

Numerical Simulation for Ship Manoeuvring and Path Following in Level Ice

by

©Quan Zhou, B.Eng

A Thesis submitted to the School of Graduate Studies
in partial fulfillment of the requirements for
the degree of Master of Engineering

Faculty of Engineering and Applied Science

Memorial University of Newfoundland

May 2014

St. John's

Newfoundland

Canada

Abstract

This thesis provides a method that combines numerical detection and semi-empirical formulas to solve the ship-level ice interaction in time domain which can be applied to studying ship manoeuvring and autopilot in level ice. Numerical implementation has been accomplished by using programming language FORTRAN90 under Linux Operation System.

The ship-ice interaction and the ice breaking process is simulated by adopting a 2-D Discrete Element Method (DEM). A new detection technique name Polygon-Point Algorithm is developed to identify the contact area. Different Pressure-Area (P-A) relation and flexural ice plate model are included and studied. Full 3DOF ice induced load is derived in this thesis. The method is validated by using the data from two model ship tests and one full scale sea trial.

A Line-of-Sight (LOS) guidance system and PID controllers for path following and velocity maintaining are also developed. Detail has been provided in solving discontinuity of commanded heading angle. The path following ability has been examined and presented.

Recommendations for future works is also provided in the thesis.

Acknowledgements

First of all, I would like to express my sincere gratitude to Dr. Heather Peng, my supervisor, for her guidance and support through my study at Memorial University of Newfoundland. Her kindly encouragement and insightful supervision have greatly facilitated the successful completion of my research.

I am sincerely thankful to Dr. Claude Daley and Dr. Wei Qiu for the expert advice and professional and valuable discussions. Special thanks to Dr. Don Spencer for providing me valuable model test data.

The financial support from NSERC CREATE Training Program for Offshore Technology Research (OTR), supports from Faculty of Engineering and Applied Science of Memorial University of Newfoundland are highly appreciated.

Lastly, and far from least, I would like to thank my parents, my sister, and Yuan Zhou, my girlfriend, for their continuous love, understanding, and support, thank all the people who provided me kindly help and support throughout my entire time at Memorial University.

Table of Contents

Abstract	ii
Acknowledgments	iii
Table of Contents	vii
List of Tables	viii
List of Figures	xi
1 Introduction	1
1.1 Background	1
1.2 Literature Review	2
1.2.1 Empirical Solutions	2
1.2.2 Numerical Solutions	8
1.3 Objectives	11
1.4 Thesis Outline	11
2 Description of the Numerical Model	13
2.1 General	13
2.2 Kinematics	14
2.2.1 Coordinate Systems	14

2.2.2	Motion Variables and Notations	16
2.2.3	Transformation Between Different Systems	17
2.2.4	Simplifying to 3DOF	18
2.3	Rigid Body Kinetics	19
2.3.1	6DOF Model	19
2.3.2	External Forces and Moments	21
2.3.3	Simplifying to 3DOF	22
2.4	Ice Induced Force	22
2.4.1	Breaking Force Component	23
2.4.1.1	Ship-Ice Contact	23
2.4.1.2	Crushing Force	24
2.4.1.3	Frictional Force	27
2.4.1.4	Breaking Force	28
2.4.1.5	Breaking by Bending	29
2.4.1.6	Ice Edge Updating	30
2.4.1.7	Effect of Ice Flexural Deflection	31
2.4.2	Clearing and Buoyancy Force Components	33
2.5	Hydrodynamic Force	35
2.6	Propeller Thrust	36
2.7	Rudder Force	37
2.8	Summary	37
3	Guidance and Control System	38
3.1	General	38
3.2	Line-of-Sight Guidance	40
3.2.1	Enclosure-based Method	40
3.2.2	Lookahead-based Method	42

3.2.3	Way-point Switching Algorithm	44
3.3	Reference Model	44
3.4	LOS Controller	45
3.5	Summary	47
4	Numerical Implementation of the Model	49
4.1	Ship-Ice Interaction	51
4.2	Contact Detecting and Ice Edge Updating	53
4.3	Mapping for LOS guidance system	54
4.4	Summary	59
5	Results, Validation, and Analysis	61
5.1	Convergence Study	62
5.2	Study of P-A relation	65
5.3	Study of the Ice Plate Deflection	66
5.4	Benchmark with Terry Fox Model Test	68
5.4.1	Descriptions	68
5.4.2	Straight Motion Test	68
5.5	Benchmark with R-Class Icebreaker Model Test	70
5.5.1	Descriptions	70
5.5.2	Pure Yaw Tests	71
5.6	Benchmark with R-Class Icebreaker Full Scale Sea Trials	72
5.6.1	Descriptions	72
5.6.2	Straight Motion	77
5.6.3	Turning a Circle	80
5.7	Study of Path-Following Ability	83
5.7.1	Analysis of a Single Convergence Action	83

5.7.2	Path-Following Performance	88
5.8	Summary	91
6	Conclusions and Recommendations	92
6.1	Conclusions	92
6.2	Recommandations	94
	Bibliography	95
	Appendices	103
A	Ship resistance estimated by Holtrop and Mennen	104
A.1	Frictional Resistance	105
A.2	Appendage Resistance	106
A.3	Wave Resistance	107
A.4	Pressure Resistance due to Bulbous Bow	108
A.5	Pressure Resistance due to Transom Immersion	109
A.6	Model-Ship Correlation Resistance	109

List of Tables

2.1	The notation of SNAME (1950) for marine vessels	16
4.1	simulation test matrix	49
5.1	Different ice model	66
5.2	Duration, mean resistance and deflection ratio of different ice model .	66
5.3	Main dimensions of the IOT Terry Fox Model Ship	68
5.4	Main dimensions of the IOT R-Class Model Ship	71
5.5	Main dimensions of the full scale CCGS R-Class icebreaker	77
5.6	Turning performance - steady speed in turn and turning diameter . .	80
5.7	Value of PID coefficients for control in water	84
5.8	Value of PID coefficients for control in ice	84
A.1	Stern Shape Factor	105
A.2	Approximate Values of Form Factor for Various Appendages	107

List of Figures

2.1	Sketch of the three coordinate systems	15
2.2	Sketch of four interaction scenarios	25
2.3	Sketch of two contact surface shapes	26
2.4	Directions of force and velocity components	28
2.5	Ice edge update in a simulated tow test of a 1:21.8 scale Terry Fox ship model	30
2.6	Flexural deflection of the ice plate	32
3.1	Line-of-Sight guidance principle	40
3.2	Diagram of the speed control feedback loop	46
3.3	Diagram of the steering control feedback loop	47
4.1	flow chart of the main routine	50
4.2	flow chart of ship-ice interaction	52
4.3	Definitions of quadrants	55
4.4	Comparison between mapped guidance and non-mapped guidance . .	56
5.1	Simulated global resistance as a function of discrete length of ice with time step of 0.01s	62
5.2	Computational time cost as a function of discrete length of ice with time step of 0.01s	63

5.3	Simulated global resistance as a function of non-dimensional time step with discrete length ratio of 0.004	63
5.4	Computational time cost as a function of non-dimensional time step with discrete length ratio of 0.004	64
5.5	Mean ice resistance at different velocity with different exponent values	65
5.6	Ice resistance with the a single interaction cycle at stem	67
5.7	IOT Terry Fox model ship water line profile	68
5.8	Time history of ice resistance when $u=0.3m/s$	69
5.9	Mean ice resistance against ship velocity in straight motion tests . . .	70
5.10	IOT R-Class model ship water line profile	70
5.11	Ice resistance during a 50-second continuous pure yaw test, $\dot{x} = 0.5m/s$	73
5.12	Ice induced sway force during a 50-second continuous pure yaw test, $\dot{x} = 0.5m/s$	73
5.13	Ice induced yaw moment during a 50-second continuous pure yaw test, $\dot{x} = 0.5m/s$	74
5.14	Linear regression model between yaw rate and yaw moment, $\dot{x} = 0.5m/s$	74
5.15	Ice resistance during a 50-second continuous pure yaw test, $\dot{x} = 0.7m/s$	75
5.16	Ice induced sway force during a 50-second continuous pure yaw test, $\dot{x} = 0.7m/s$	75
5.17	Ice induced yaw moment during a 50-second continuous pure yaw test, $\dot{x} = 0.7m/s$	76
5.18	Linear regression model between yaw rate and yaw moment, $\dot{x} = 0.7m/s$	76
5.19	Resistance of R-Class in water	78
5.20	Thrust of R-Class in water	78
5.21	Resistance of R-Class in level ice	79
5.22	Thrust of R-Class in level ice	79

5.23	Turning track and broken ice channel	81
5.24	Time history of simulated ice load and the mean value during turning	81
5.25	Time history of simulated velocities during turning	82
5.26	Simulated ship track of a specific single convergence action in water .	85
5.27	Simulated heading signals of a specific single convergence action in water	85
5.28	Simulated surge speed of a specific single convergence action in water	86
5.29	Simulated ship track of a specific single convergence action in ice . . .	86
5.30	Simulated heading signals of a specific single convergence action in ice	87
5.31	Simulated surge speed of a specific single convergence action in ice . .	87
5.32	Simulated performance of path following capability, case 1	89
5.33	Simulated performance of path following capability, case 2	90

List of Symbols

$O-NED$	Global coordinate system that is fixed on the earth surface
$\bar{x}, \bar{y}, \bar{z}$	Coordinates with respect to $O-NED$ frame
$o-xyz$	Local coordinate system that is fixed on the vessel
x, y, z	Coordinates with respect to $o-xyz$ frame
$o_i-x_iy_iz_i$	Local coordinate system that is fixed on the ice plate
ϕ, θ, ψ	Euler angles defining rotation from earth fixed coordinate system to ship fixed coordinate system
u, v, w	Linear velocity along x, y, and z directions
p, q, r	Angular velocity about x, y, and z directions
X, Y, Z	External forces acting on the vessel in x, y, and z directions
K, M, N	External moments acting on the vessel about x, y, and z directions
η	Position and orientation vector with respect to $O-NED$ frame in 3DOF and 6DOF
Θ	Euler angle vector
ν	Vector of linear and angular velocity with respect to $o-xyz$ frame in 3DOF and 6DOF
$\mathbf{J}(\Theta)$	Transformation matrix from $o-xyz$ frame to $O-NED$ frame in 6DOF

$\mathbf{R}(\psi)$	Transformation matrix from $o-xyz$ frame to $O-NED$ frame in 3DOF
\mathbf{M}	Rigid body mass/inertia matrix of the vessel
m	Mass of the vessel
$\mathbf{C}(\boldsymbol{\nu})$	Rigid body Coriolis and centripetal matrix caused by the rotation of $o-xyz$
\mathbf{F}_{TOT}	Total external force and moment vector
x_g, y_g, z_g	Coordinates of center of gravity of the vessel with respect to $o-xyz$
I_x, I_y, I_z	Moments of inertia of the vessel with respect to x, y, and z axes
I_{xy}, I_{xz}, I_{yz}	Products of inertia of the vessel
I_{yx}, I_{zx}, I_{zy}	
\mathbf{F}_H	Vector of hydrodynamic force acting on the vessel
\mathbf{F}_P	Vector of thrust generated by main propeller
\mathbf{F}_R	Vector of control force generated by rudder
\mathbf{F}_{ice}	Vector of ice induced force
X_H, Y_H, N_H	Hydrodynamic force components in 3DOF
X_P, Y_P, N_P	Propeller thrust components in 3DOF
X_R, Y_R, N_R	Rudder force components in 3DOF
$X_{ice}, Y_{ice}, N_{ice}$	Ice induced force components in 3DOF
X_{br}, Y_{br}, N_{br}	Ice breaking force components in 3DOF
X_b, Y_b, N_b	Ice buoyancy force components in 3DOF
X_{cl}, Y_{cl}, N_{cl}	Ice clearing force components in 3DOF
F_{cr}	Force caused by the vessel crushes the ice
p_{ave}, A_{cr}	Average pressure and area of the crushing surface

p_0, ex	Nominal pressure and constant exponent in pressure-area relation
h_i	Ice thickness
L_c, L_h	Maximum penetration distance and maximum width in a contact zone
α, γ, β'	Water line angle, flare angle, and normal frame angle of the vessel at place the crushing happens
f_h, f_v	Frictional forces exist in horizontal plane and normal vertical plane
v_τ, v_n	Tangential and normal components of relative velocity
C_f, C_l, C_v	Tunable parameters
l, E, σ_f	Characteristic length, Young's modulus, and flexural strength of ice
Z_{br}, P_{bear}	Vertical force component due to ice breaking and bearing capacity of the ice plate
$\delta_v, \delta_e, \delta_c$	Total vertical displacement, flexural deflection, and crushing penetration at crushing edge
$F_{cr,v}$	Vertical component of crushing force that cause vertical deflection and crushing penetration simultaneously
$Y_{i,bow}, Y_{i,mid}$	Sway force at bow and at midship
$\psi_{los}, \psi_{ref}, \psi_r(e)$	Command Line-of-Sight heading, reference heading, and track relative angle
K_{pr}, K_{dr}, K_{ir}	Proportional gain, derivative gain, and integral gain to determine track relative angle
τ_1, τ_3	Control law for dynamic task and geometrical task

K_{p1}, K_{d1}, K_{r1}	Proportional gain, derivative gain, and integral gain of the controller for propeller
K_{p3}, K_{d3}, K_{r3}	Proportional gain, derivative gain, and integral gain of the controller for rudder

Chapter 1

Introduction

1.1 Background

Estimating the performance of a ship or an offshore structure operating in ice-covered water is not new to naval architects. A number of researchers have studied this topic, and the earliest research can be traced back to Runeburg in 1888 (Jones, 2004). In recent decades, the increase of oil and gas exploration in Arctic and Sub-Arctic regions and the potential of transportation through the Northern Sea Route has resulted in a renewed interest in the ship-ice interaction and the controllability of a ice-going vessel.

The ship-ice interaction includes various aspects: the hull-ice interaction, the rudder-ice interaction, and the propeller-ice interaction. The ice resistance on the ship hull has been investigated since early 18th century (Liu, 2009). A considerable effort was put to measuring ice resistance on different ships and establishing mathematical models for predicting ice resistance.

Comparing to the relatively well investigated ice resistance, the ship manoeuvrability in ice, on the other hand, was drawn less attention in the literature. The manoeuvra-

bility is one aspect of the controllability. According to Lewis (1988), controllability is defined as “regulating a ship’s trajectory, speed, and orientation at sea as well as in restricted waters where positioning and station keeping are of particular concern”, and the manoeuvrability is the ability of the change in the direction of motion under control. The investigation of a ship’s manoeuvrability in ice is necessary because the ship will navigate in confined passageways to avoid hazards. Various methods, including full scale sea trials, model tests, and numerical simulations, are applied to study the ship manoeuvring problem.

1.2 Literature Review

Ship manoeuvring in ice fields has attracted people’s attention for many years. Recently increasing interests in oil and gas exploration in Arctic and Sub-Arctic regions and transportation through the Northern Sea Route requires a better understanding of vessel-ice interactions and vessel’s manoeuvring performance in ice. Considerable efforts have been made in this research area. The global ice loads on the hull have been studied, but most of the previous works focus on ice resistance only (Liu, 2009). Jones (1989, 2004) has reviewed the research on ship resistance in level ice from 1888 to 2004. In this chapter, the numerical models including ice resistance models and manoeuvring models since 2004. Existing models for hull-ice interaction in a continuous ice breaking process were collected and evaluated.

1.2.1 Empirical Solutions

Kashteljan et al. (1969) proposed a formula which was considered as the first analytical solution to level ice resistance by breaking it down into its components. In his model, the total resistance in ice consisted of four parts: the resistance caused by

breaking the ice plate (R_1); the resistance connected with weight (i.e. submerging and turning broken ice floes, changing position of the icebreaker, and dry friction resistance, denoted as R_2); the resistance caused by traveling through broken ice (R_3); and water viscous influence and wave-making resistance (R_4).

$$R_{TOT} = R_1 + R_2 + R_3 + R_4 \quad (1.1)$$

Lewis and Edwards (1970) modified Kashteljan's formula based on a regression analysis of available full-scale and model test data. They considered three different components: the component attributes to ice breaking and friction, the component attributes to ice buoyancy, and the component attributes to momentum exchange between the ship and broken ice. Non-dimensional coefficients were further used and good fits with full-scale and model-scale tests of Wind-class, Raritan, M-9 and M-15 were obtained

$$R_i = C_0\sigma h^2 + C_1\rho_i g B h^2 + C_2 B h v^2 \quad (1.2)$$

The first term is related to ice breaking. It can be seen that the ice flexural strength and thickness are significant in ice breaking mechanism. The second term represents the resistance that attributes to ice buoyancy. It is related to submerged ice volume and its density. The third term accounts for the influence due to momentum loss of the ship so that it is proportional to velocity square. Lewis and Edwards' method is of great value because it isolates one key factor, e.g., the ship velocity, from others. However, this method is not perfect. The buoyancy, for instance, should be related to the density difference between ice and water.

Significant contributions were made by Enkvist (1972) to the study of ship performance in level ice (Jones, 2004). Similar to Lewis and Edward's works, a three-component model was applied in Enkvist's study. Model tests of three ships, Moskva-

class, Finncarrier, and Jelppari, were carried out at creep speed to investigate the effect of ship velocity. He then conducted tests in pre-sawn ice conditions to isolate the submergence term. He was the first person to describe such test procedure in detail and able to determine the “relative importance of different terms” in his model (Jones, 2004). Enkvist suggested the following formula on ice resistance:

$$R_{TOT} = C_1 B h \sigma + C_2 B h T \rho_{\Delta} g + C_3 B h \rho_i v^2 \quad (1.3)$$

The three terms represent the resistance due to ice breaking, ice buoyancy, and momentum loss. Comparing to Eq. 1.2, we can see that Enkvist concluded the ice breaking resistance was proportional to ice thickness and ship width instead of thickness square. He also concluded the ice buoyancy resistance is related to the density difference between the ice and the water.

In his later work, Enkvist (1983) applied his technique to 16 full-scale ship tests to investigate the relation between the submersion and ice breaking components in level ice resistance. He obtained the expression of submersion term and extrapolated it to zero-speed resistance in order to achieve breaking component in full scale. He reached a conclusion that the percentage of breaking resistance in total low-velocity resistance varied between 40% and 80%, with the higher figure for the smaller ships.

Milano (1972) studied the resistance from an energy perspective for a ship moving in level ice. The total energy loss consisted of five terms: energy that made ship moving through ice-filled channel (E_1), energy that absorbed during local crushing caused by impact with cups wedge (E_2), energy that lifted the ship onto the ice (E_3), energy that caused inner fracture (E_4), and energy that made the ship moving forward, forcing the broken ice downward (E_5). The conceptual equation was given as Eq. 1.4. An explicit analytical expression was derived and good correlation was

obtained between his prediction and full-scale test data of the Mackinaw. He also proposed the speed dependence, known as “Milano hump”, and explained how it was related to the different mechanisms involved in the energy equations.

$$E_T = E_1 + E_2 + E_3 + E_4 + E_5 \quad (1.4)$$

Lindqvist (1989) proposed an analytical method to calculate ice resistance for an ice-going ship. He simplified hull form as several flat plates, identified three main components of ice resistance, and approximated their contribution with main principles of the ship and “simple but physically sound formulas”. He stated the energy of the ship will be absorbed by crushing ice at the stem (R_c), by bending the ice plate and further causing breaking (R_b), and by interacting with broken ice pieces (R_s). Each phenomenon must generate a force on the ship; therefore, three different components were achieved separately. He also considered the effect of speed by coming up with a linear relationship between ship speed and ice resistance. Finally, he verified his formulas with three different ships (JELPPARI, OTSO KONTIO, and VLADIVOSTOK) in Baltic conditions. This method balances the submersion component and breaking component and is easy to carry out since only main principles of the ship are required.

$$R_{ice} = (R_c + R_b) \times g_1(v) + R_s \times g_2(v) \quad (1.5)$$

Colbourne (1989) presented a detailed review of the work done previous in his PhD dissertation. He came up with a method to analyse the icebreaking model test and further applied the conclusion to full scale ships. The method broke the total ice resistance down into breaking resistance, clearing resistance, and viscous drag (skin friction). It is a combination of the model test and the analytical solution. The basic steps in the method were presented in his dissertation. The ship would be towed

through intact level ice, as well as pre-sawn ice, and resistance will be measured. Viscous drag was achieved by using ITTC method and further subtracted from pre-sawn resistance to yield the ice clearing term. Breaking term can be obtained by subtracting pre-sawn resistance from level ice resistance. Non-dimensional numbers are used to apply model test conclusions to full scale ships. In his dissertation, Colbourne applies the method to four different ships.

Spencer (1992) used a similar regression model and the experiment procedure to Colbourne's. He split the total resistance into ice breaking, clearing, buoyancy, and open water resistance. Standard test procedure and Standard analysis procedure were introduced in his paper. Further, this method was applied to predicting ice resistance of Canadian Coast Guard "R-Class" icebreakers in (Spencer and Jones, 2001). The regression formula of ice resistance is achieved from model tests. Good agreement between calculated total resistance and measured resistance can be observed in their work.

$$R_{tot} = R_w + C_{br}\rho_i B h_i v^2 + C_{cl}\rho_i B h_i v^2 + C_b \Delta \rho g h_i B T \quad (1.6)$$

where R_w stands for open water resistance, C_{br} , C_{cl} , and C_b are empirical coefficients for ice breaking resistance, ice clearing resistance, and ice buoyancy resistance. C_b is constant, while the other two are determined by

$$C_{br} = f_1(F_h) \quad (1.7)$$

$$C_{cl} = f_2(S_N) \quad (1.8)$$

where

$$F_h = \frac{v}{\sqrt{g h_i}} \quad (1.9)$$

is the ice Froude number, and

$$S_N = \frac{v}{\sqrt{\frac{\sigma_f h_i}{\rho_i B}}} \quad (1.10)$$

is the ice strength number.

Keinonen (1996) suggested a formula for the total resistance of an icebreaker in level ice on the basis of a large database of sea trials of 16 CCGS R-Class icebreakers (Keinonen, 1996; Keinonen et al., 1989, 1991). The total resistance at speed v ($R(v)_t$) was expressed in terms of three components: open water resistance at speed v m/s ($R(v)_{ow}$); ice breaking resistance at 1 m/s ($R(1m/s)_{ice}$) that included the major ice breaking component plus ice submergence and clearing components that was done by Keinonen et al. (1991); the increase in icegoing resistance above that at 1m/s ($R(> 1m/s)_{ice}$). Two practical formulas were achieved in their work to calculate the third component ($R(> 1m/s)_{ice}$) of either round hull form icebreaker or chinned hull form icebreaker.

$$R(v)_t = R(v)_{ow} + R(1m/s)_{ice} + R(> 1m/s)_{ice} \quad (1.11)$$

Although those reviewed methods vary from one to another, the researchers share some common knowledge, which is to separate the total resistance into different components according to one specific interaction event, in addressing ice resistance. The real ship-ice interaction is complicated and not fully understood. The physical process involves solid-solid interaction, solid-fluid interaction and a series of events that are joint together. It is crucial to simplify the real physical process by determining the major factors, isolating each of them and finding its contribution to the total resistance. This core idea is also accepted by the numerical approaches.

1.2.2 Numerical Solutions

In the recent decades, efforts have been put onto development of numerical methods based on the empirical formulas. They can be used to simulate continuous structure-ice interaction process, i.e., Daley’s conceptual model of ice failure as “a nested hierarchy of discrete failure events” (Daley et al., 1998). In particular, one numerical approach, named Discrete Element Method (DEM), which discretize continuous ice material and the structure into many small elements, is widely applied in solving structure-ice interaction (Lau et al., 2004; Liu, 2009; Nguyen, 2011; Nguyen et al., 2009; Sawamura et al., 2009a,b; Su et al., 2010; Tan et al., 2013; Wang, 2001).

Daley et al. (1998) proposed a conceptual model which described ice failure as “a nested hierarchy of discrete failure events” which was based on observation and was a continuation of his previous work (Daley, 1991, 1992). In the model, each discrete process was happening with another discrete process and comprised of a continuous process and a series of limit events. Due to the iterative nature and hierarchy of different limit mechanisms, this concept is more general and further applied to numerically simulate structure-ice interaction by many researchers.

Wang (2001) adopted Daley’s conceptual framework and simplified it as a continuum process of crushing, bending, and rubble formation in her study of conical structure breaking level ice. She proposed a geometric grid method to simulate continuous contact between the structure and level ice. Analytical formulas are applied to achieve crushing force and bearing capability, while geometric grid method is used to numerically detect ice-structure contact and update ice profile after bending failure. She also assumed the broken ice floes have circular shape and their size is related to ship speed, V , and ice characteristic length, l . She gave the Eq. 1.12 to calculate ice floe size without reference without detailed interpretation. This strategy to simulate ice-fixed structure interaction is widely extended to solving the interaction between

ice and moving structures.

$$R = C_l l (1 + C_v V) \quad (1.12)$$

Lau et al. (2004) proposed a model that decomposes the total yaw moment into its components which is analogous to the formation of ice resistance in (Spencer, 1992). He divided total moment into hydrodynamic, breaking, submergence, and ice clearing, components and further derived the formulas for breaking and submergence terms. In his method, ice-induced force was considered as three concentrated loads among which two were acting at the bow and the other was on the parallel midship body. Yaw moment can be easily obtained by multiplying those loads to the corresponding rotate arms. This strategy is simplified but still valuable. Because ship motion is able to be involved.

Martio (2007) develops software to numerically simulate the vessel's manoeuvring performance in uniform level ice. His work is on the basis of Lindqvist's ice resistance model (Lindqvist, 1989). The major contribution of his work is to consider the effect of bending and submergence terms on sway and yaw motions. In his work, Lindqvist's formulas are modified and relationships between resistance and transverse force, as well as yaw moment, are proposed.

Sawamura et al. (2009a) developed a numerical method, which shared the same strategy with Wang's work, to calculate the repetitive ice breaking pattern and load with a circle contact algorithm. In the method, he used small circles, instead of grid in Wang's work, to represent discrete ship waterline and the entire ice plate. Contact will be detected if the distance between the center of hull circle and ice circle is less than the sum of the radius of the circles. Similar to the geometric grid method in Wang's work, the circle contact algorithm still requires discretizing the entire ice plate that results in inefficient calculation since most circles are not involved in the interaction.

Nguyen et al. (2009) applied the same strategy but came up with a different DEM method to simulate vessel-ice interaction. In their work, only the ice edge and ship waterline profile were discretized into points. Contact or not was determined by checking the distance between two arbitrary points that one was on ice edge and the other was on ship waterline. He also assumed the crushing force increases linearly from zero to the maximum value that led to ice breaking by bending. Therefore, ice-induced force on the ship can be achieved by time past since initial contact instant and the bearing capability of the ice plate. They numerically calculated the force due to crushing at the stem and applied Lindqvist's formula (Lindqvist, 1989) to obtain bending and submergence force. The discretization strategy is more time efficient because it avoids discretizing the internal part of ice plate that is not involved in ship-ice interaction.

Su et al. (2010) followed Nguyen's DEM strategy that only discretizing the ice edge and ship waterline. However, the assumption that crushing force increases linearly was abandoned, and a new contact detecting algorithm was proposed without detail. He simply assumed ice crushing force is proportional to contact area which will be determined numerically at each time instant. He also added frictional force into his model by considering it consists of two parts and each part is proportional to the corresponding relative velocity component.

Zhou and Peng (2013a) continued the DEM strategy and proposed a different contact detecting method that categorized ship-ice interaction into four scenarios. They identified the contact via investigating the relationship between nodes, which represented ice edge, and the polygon, which represented the ship water line, and applied interpolation method to improve calculation accuracy. The 1:21.8 scale Terry Fox model ship was used to validate the method. In their further study, Zhou and Peng (2013b) conducted another case study with the 1:20 scale R-Class icebreaker model.

1.3 Objectives

The major work of this study is to develop a numerical simulator that can be used to investigate the manoeuvrability and the controllability of a vessel in level ice. The main objectives include:

- To develop a numerical hull-ice interaction model that is able to predict ice load in 3 Degrees of Freedom in time domain. The model is also able to carry out prescribed manoeuvres of a ship.
- To develop a guidance and controller system for a ship's path following in ice.
- To verify the hull-ice interaction model by comparing to full scale sea trials and ship model tests.
- To investigate a ship's manoeuvrability in ice.
- To provide proposals for further work.

1.4 Thesis Outline

This thesis presents a simulation in time domain of ship manoeuvring in level ice.

- Chapter 1 provides the introduction to the entire thesis, reviews previous works on mathematical modeling and numerical modeling of ship resistance and manoeuvring in level ice, and introduces the objectives and the outline of this thesis.
- Chapter 2 introduces the theoretical derivation of the numerical model in detail. The chapter includes a 2-dimensional hull-ice interaction mechanics as well as the mathematical models of the hull, the propeller, the rudder and their interactions.

- Chapter 3 applies Line-of-Sight method to develop the guidance and control system. The system is used to accomplish path-following simulations.
- Chapter 4 describes the numerical implementation of the simulation model based on chapter 2 and 3. In particular, the hull-ice interaction and the Line-of-Sight guidance system are thoroughly interpreted.
- Chapter 5 provides the the verification of the numerical model. The studies of the convergence ability and the effects of P-A relationship and flexural ice model are carried out. Simulation and comparison are conducted with two IOT model ships and a full-scale CCGS R-Class icebreaker.
- Chapter 6 concludes the current work and provides recommendation for future research.

Chapter 2

Description of the Numerical Model

2.1 General

Ship manoeuvring in ice is a complex process that involves solid-solid and solid-fluid interactions. As proposed by previous researchers, a repeatable and simplified procedure is applied to simulate the real physical process of the interaction between the ship and a small ice piece. From the macro perspective, the ice breaking process occurs equally on both sides of the ship when it transits forward. An approximately equal amount of ice floes pass along both sides of the ship hull. These ensure the assumption of symmetrical ice load on the hull in early research. However, the symmetry of the ice load is no longer valid when the ship turns in ice. Different amount of ice floes passing along both sides results in lateral clearing and buoyancy forces. Furthermore, one side of the hull may contact more intact ice cover so that icebreaking happens more on this side than on the other one. This also leads to an asymmetrical breaking force. The ice breaking pattern during the ship-ice interaction is complex

and stochastic. Most previous works adopt cusp breaking patterns and elastic plate theories. Various ice failure modes exist due to the stochastic nature of ice plate and the varying flare angle of the hull.

This chapter derives the mathematical model of ship manoeuvring in ice based on previous works (Lau et al., 2004; Liu, 2009; Nguyen et al., 2009; Sawamura et al., 2009a; Su et al., 2010; Wang, 2001). It considers the distributed breaking force, buoyancy force, and clearing force, separately. Two failure modes, crushing and bending, are involved. Ice floe hydrodynamics is included in clearing force. The hull-ice contact is numerically detected at each time step. The ice channel is tracked and exported to files when breaking happens. The ship dynamics, the models of propeller and rudder are also included in this chapter. The integral numerical model is time efficient and has the capability of carrying out various tests.

2.2 Kinematics

The developed numerical model only considers the motions of the ship and the ice plate in the horizontal plane with three degrees of freedom (3DOF). However, for completeness and further extension, we introduce coordinate systems and transformation in 6DOF. The transformation is then simplified to 3DOF for further application.

2.2.1 Coordinate Systems

To describe the interaction between the ship and the ice plate, three coordinate systems, i.e., a global coordinate system and two moving local coordinate systems, are introduced; one local coordinate system is attached on the ship and the other is attached on the ice plate. Figure 2.1 depicts these coordinate systems in 3-dimension. These systems use the standard right-hand rule convention.

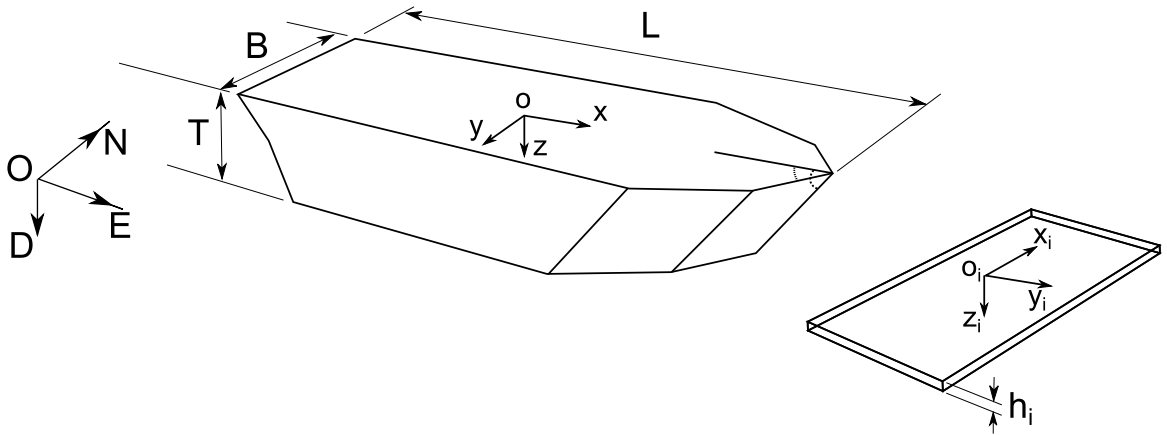


Figure 2.1: Sketch of the three coordinate systems

The global coordinate system, named North-East-Down system (denoted as $O-NED$), is defined as the tangent plane on the surface of the Earth. This system is used for Earth navigation of a marine craft. $O-NED$ is assumed inertial such that Newton's laws still apply. The N -axis points towards true North, the E -axis points towards East, while the D -axis points downwards normal to the Earth's surface (Fossen, 2011). The positions and orientation of the vessel and the ice are described relative to $O-NED$. The coordinates respect to $O-NED$ frame are expressed as $[\bar{x}, \bar{y}, \bar{z}]^T$.

The ship-fixed coordinate system (denoted as $o-xyz$) is the moving local system that is attached on the ship. The origin o is chosen to coincide with the geometry center of the water plane. For a vessel, the axes x , y , and z are chosen to coincide with the principal axes of inertia, and they are usually defined as:

- x - longitudinal axis (directed from aft to fore)
- y - transversal axis (directed to starboard)
- z - vertical axis (directed from top to bottom)

The linear and angular velocities of the vessel should be expressed in this coordinate system.

The ice-fixed coordinate system, denoted as $o_i-x_iy_iz_i$, is the moving local system that is attached on the ice plate. For convenience, the origin is chosen to coincide with an arbitrary point on the edge of the ice plate, and the axes x_i , y_i , and z_i are initially chosen to parallel to the corresponding axes of $O-NED$, respectively. The linear and angular velocities of the ice plate, as well as the coordinates of the discretized points, are expressed relative to this system.

2.2.2 Motion Variables and Notations

Six dependent coordinates are required to determine the position and orientation for a vessel in 6DOF. The first three coordinates, with their time derivatives, correspond to the position and translational motions along the x , y , and z axis, while the last three coordinates and their time derivatives describe the orientation and rotational motions of the vessel. Generally, the six motion components are defined as surge, sway, heave, roll, pitch, and yaw. The notation of SNAME (1950) for marine vessels, as listed in 2.1, is used.

Table 2.1: The notation of SNAME (1950) for marine vessels

DOF		Forces and moments	Linear and velocities	Position and Euler angles
1	motion in the x direction (surge)	X	u	x
2	motion in the y direction (sway)	Y	v	y
3	motion in the z direction (heave)	Z	w	z
4	rotation about the x direction (roll)	K	p	ϕ
5	rotation about the y direction (pitch)	M	q	θ
6	rotation about the z direction (yaw)	N	r	ψ

2.2.3 Transformation Between Different Systems

During the numerical integration scheme, once the translational and rotational velocities are obtained in ship-fixed coordinate system, they should be transformed into the global coordinate system to achieve the changing rate of the coordinates of the origin of the ship-fixed reference frame. The transformation law is given by:

$$\begin{pmatrix} \dot{\bar{x}} \\ \dot{\bar{y}} \\ \dot{\bar{z}} \\ \dot{\phi} \\ \dot{\theta} \\ \dot{\psi} \end{pmatrix} = \begin{bmatrix} c\psi c\theta & -s\psi c\theta + c\psi s\theta s\phi & s\psi s\theta + c\psi c\phi s\theta & 0 & 0 & 0 \\ s\psi c\theta & c\psi c\phi + s\psi s\theta s\phi & -c\psi s\theta + s\psi s\phi c\theta & 0 & 0 & 0 \\ -s\theta & c\theta s\phi & c\theta c\phi & 0 & 0 & 0 \\ 0 & 0 & 0 & 1 & s\phi t\theta & c\phi t\theta \\ 0 & 0 & 0 & 0 & c\phi & -s\phi \\ 0 & 0 & 0 & 0 & s\phi c\theta & c\phi c\theta \end{bmatrix} \begin{pmatrix} u \\ v \\ w \\ p \\ q \\ r \end{pmatrix} \quad (2.1)$$

where $s \cdot = \sin(\cdot)$, $c \cdot = \cos(\cdot)$, $t \cdot = \tan(\cdot)$.

Rewrite 2.1 in vectorial form :

$$\dot{\boldsymbol{\eta}} = \mathbf{J}(\boldsymbol{\Theta}) \cdot \boldsymbol{\nu} \quad (2.2)$$

where $\boldsymbol{\eta} = [\bar{x}, \bar{y}, \bar{z}, \phi, \theta, \psi]^T$ denotes the positions and orientation vector, $\boldsymbol{\Theta} = [\phi, \theta, \psi]^T$ is a vector of Euler angles,

$$\mathbf{J}(\boldsymbol{\Theta}) = \begin{bmatrix} c\psi c\theta & -s\psi c\theta + c\psi s\theta s\phi & s\psi s\theta + c\psi c\phi s\theta & 0 & 0 & 0 \\ s\psi c\theta & c\psi c\phi + s\psi s\theta s\phi & -c\psi s\theta + s\psi s\phi c\theta & 0 & 0 & 0 \\ -s\theta & c\theta s\phi & c\theta c\phi & 0 & 0 & 0 \\ 0 & 0 & 0 & 1 & s\phi t\theta & c\phi t\theta \\ 0 & 0 & 0 & 0 & c\phi & -s\phi \\ 0 & 0 & 0 & 0 & s\phi c\theta & c\phi c\theta \end{bmatrix}$$

is the transformation matrix, and $\boldsymbol{\nu} = [u, v, w, p, q, r]^T$ denotes the linear and angular velocity vector that decomposed in the ship-fixed coordinate system.

Eq. 2.2 presents the transformation between $o-xyz$ frame and $O-NED$ frame. A similar transformation between $o_i-x_iy_iz_i$ frame and $O-NED$ frame can be obtained by replacing Euler angle and velocity vector of the ship to those of the ice plate in Eq. 2.2.

2.2.4 Simplifying to 3DOF

As mentioned, 3DOF is sufficient for this numerical model of ship manoeuvring in horizontal plane so that we can skip roll, pitch, and yaw motions, i.e., consider the corresponding Euler angle and velocity components as zero in Eq. 2.1:

$$\begin{Bmatrix} \dot{\bar{x}} \\ \dot{\bar{y}} \\ \dot{\psi} \end{Bmatrix} = \begin{bmatrix} \cos(\psi) & -\sin(\psi) & 0 \\ \sin(\psi) & \cos(\psi) & 0 \\ 0 & 0 & 1 \end{bmatrix} \begin{Bmatrix} u \\ v \\ r \end{Bmatrix} \quad (2.3)$$

2.3 can be written in vectorial form:

$$\dot{\boldsymbol{\eta}} = \mathbf{R}(\psi) \cdot \boldsymbol{\nu} \quad (2.4)$$

where $\boldsymbol{\eta} = [\bar{x}, \bar{y}, \psi]^T$ is the vector of positions and heading of the ship, $\mathbf{R}(\psi)$ is the transform matrix in 3DOF, and $\boldsymbol{\nu} = [u, v, r]^T$ is vector of velocities. Eq. 2.4 is used to achieve positions and heading changing rate.

2.3 Rigid Body Kinetics

2.3.1 6DOF Model

According to Fossen (1994, 2011), the 6DOF rigid body kinetics in ship-fixed coordinate system can be expressed in a vectorial form:

$$\mathbf{M}\dot{\boldsymbol{\nu}} + \mathbf{C}(\boldsymbol{\nu})\boldsymbol{\nu} = \mathbf{F}_{TOT} \quad (2.5)$$

where \mathbf{M} is the rigid body mass matrix that is given by Eq. 2.6; $\mathbf{C}(\boldsymbol{\nu})$, given by Eq. 2.7, is the rigid body Coriolis and centripetal matrix caused by the rotation of $o\text{-}xyz$; $\mathbf{F}_{TOT} = [X, Y, Z, K, M, N]^T$ is the generalized vector of external forces and moments respect to ship-fixed frame.

$$\mathbf{M} = \begin{bmatrix} m & 0 & 0 & 0 & mz_g & -my_g \\ 0 & m & 0 & -mz_g & 0 & mx_g \\ 0 & 0 & m & my_g & -mx_g & 0 \\ 0 & -mz_g & my_g & I_x & -I_{xy} & -I_{xz} \\ mz_g & 0 & -mx_g & -I_{yx} & I_y & -I_{yz} \\ -my_g & mx_g & 0 & -I_{zx} & -I_{zy} & I_z \end{bmatrix} \quad (2.6)$$

$$\mathbf{C}(\boldsymbol{\nu}) = \begin{bmatrix}
0 & 0 & 0 \\
0 & 0 & 0 \\
0 & 0 & 0 \\
-m(y_g q + z_g r) & m(y_g p + w) & m(z_g p - v) \\
m(x_g q - w) & -m(z_g r + x_g p) & m(z_g q + u) \\
m(x_g r + v) & m(y_g r - u) & -m(x_g p + y_g q) \\
m(y_g q + z_g r) & -m(x_g q - w) & -m(x_g r + v) \\
-m(y_g p + w) & m(z_g r + x_g p) & -m(y_g r - u) \\
-m(z_g p - v) & -m(z_g q + u) & m(x_g p + y_g q) \\
0 & -I_{yz}q - I_{xz}p + I_z r & I_{yz}r + I_{xy}p - I_y q \\
I_{yz}q + I_{xz}p - I_z r & 0 & -I_{xz}r - I_{xy}q + I_x p \\
-I_{yz}r - I_{xy}p + I_y q & I_{xz}r + I_{xy}q - I_x p & 0
\end{bmatrix} \quad (2.7)$$

where x_g , y_g , and z_g denotes the coordinates of the center of gravity of the ship in $oxyz$, I_x , I_y , I_z denote the moment of inertia about the x , y , and z axes, and $I_{xy} = I_{yx}$, $I_{xz} = I_{zx}$, and $I_{yz} = I_{zy}$ are the products of inertia. They are valid when the ship is port-starboard symmetrical and fore-aft symmetrical.

$$I_x = \int_m (y^2 + z^2) dm \quad (2.8)$$

$$I_y = \int_m (x^2 + z^2) dm \quad (2.9)$$

$$I_z = \int_m (x^2 + y^2) dm \quad (2.10)$$

$$I_{xy} = \int_m xy dm \quad (2.11)$$

$$I_{xz} = \int_m xz dm \quad (2.12)$$

$$I_{yz} = \int_m yz dm \quad (2.13)$$

Merging Eqs. 2.6 and 2.7 into Eq. 2.5, we can achieve the expanded equations of motion of a ship:

$$\begin{aligned}
m[\dot{u} - vr + wq - x_g(q^2 + r^2) + y_g(pq - \dot{r}) + z_g(pr + \dot{q})] &= X \\
m[\dot{v} - wp + ur - y_g(r^2 + p^2) + z_g(qr - \dot{p}) + x_g(qp + \dot{r})] &= Y \\
m[\dot{w} - uq + vp - z_g(p^2 + q^2) + x_g(rp - \dot{q}) + y_g(rq + \dot{p})] &= Z \\
I_x \dot{p} + (I_z - I_y)qr - (\dot{r} + pq)I_{xz} + (r^2 - q^2)I_{yz} + (pr - \dot{q})I_{xy} \\
&\quad + m[y_g(\dot{w} - uq + vp) - z_g(\dot{v} - wp + ur)] &= K \quad (2.14) \\
I_y \dot{q} + (I_x - I_z)rp - (\dot{p} + qr)I_{xy} + (p^2 - r^2)I_{zx} + (qp - \dot{r})I_{yz} \\
&\quad + m[z_g(\dot{u} - vr + wq) - x_g(\dot{w} - uq + vp)] &= M \\
I_z \dot{r} + (I_y - I_x)pq - (\dot{q} + rp)I_{yz} + (q^2 - p^2)I_{xy} + (rq - \dot{p})I_{zx} \\
&\quad + m[x_g(\dot{v} - wp + ur) - y_g(\dot{u} - vr + wq)] &= N
\end{aligned}$$

2.3.2 External Forces and Moments

In order to solve Eq. 2.5, the generalized external forces and moments must be described in proper mathematical forms. The modular modelling approach and the principle of superposition are applied. The total forces and moments are given by:

$$\mathbf{F}_{TOT} = \mathbf{F}_H + \mathbf{F}_P + \mathbf{F}_R + \mathbf{F}_E \quad (2.15)$$

Each term consists of six elements that correspond to the six-motion components. The terms with subscript ‘‘H’’, ‘‘P’’, and ‘‘R’’ represent the hydrodynamic forces on the bare hull, the propeller, and the rudder, respectively. The interactions among them are included in each term. The term with subscript ‘‘E’’ represents the environmental force, such as the forces due to wind, wave, current, and ice. The present work assumes ice load is dominant in ice covered sea so that other environmental forces can

be neglected. Hence:

$$\mathbf{F}_{TOT} = \mathbf{F}_{ice} + \mathbf{F}_H + \mathbf{F}_P + \mathbf{F}_R \quad (2.16)$$

2.3.3 Simplifying to 3DOF

To achieve the kinetic equations for a rigid body moving in horizontal plane, we simply skip the acceleration and velocity that are associated with roll, pitch, and heave. It is also common to assume the vessel is port-starboard symmetrical so that the center of gravity lies in the longitudinal center plane of the vessel, i.e., $y_g = 0$. The equations of motions can be given by:

$$\begin{aligned} m\dot{u} - mvr - mx_g r^2 &= X_{ice} + X_H + X_P + X_R \\ m\dot{v} + mx_g \dot{r} + mur &= Y_{ice} + Y_H + Y_P + Y_R \\ I_z \dot{r} + mx_g \dot{v} + mx_g ur &= N_{ice} + N_H + N_P + N_R \end{aligned} \quad (2.17)$$

2.4 Ice Induced Force

The real mechanism of the ship-level ice interaction (icebreaking process) is complicated and remains unclear. However, many researchers have provided simplified processes to describe it (Colbourne, 1989; Enkvist et al., 1979; Keinonen, 1996; Lindqvist, 1989; Spencer, 1992). Based on those descriptions, the interaction during the ship continuously advancing into the ice plate involves three phases.

Initially, the vessel contacts with the ice plate and generates a force on the plate. The interaction force is perpendicular to the contact surface and causes ice crushing as well as vertical deflection. The force keeps increasing as the ship is moving forward until ice is broken by bending and then a cusp forms. In the case of thick ice or a vessel with a large flare angle, only crushing failure might occur, i.e., the flexural capacity of the ice plate would not be reached. When an ice floe is broken off the plate, it

continues moving downward. The floe is also rotated and accelerated simultaneously until it is parallel to the wet surface of the hull. Finally, ice pieces slide along the hull until they leave it.

Though it is questionable (Enkvist et al., 1979), the methodology in which the total ice load is divided into its components that represent the corresponding physical processes has been widely used. Considering the fore-mentioned processes, the total ice induced force is divided into three independent components, i.e., breaking, buoyancy, and clearing force components (Colbourne, 1989; Spencer, 1992; Spencer and Jones, 2001):

$$\mathbf{F}_{ice} = \mathbf{F}_{br} + \mathbf{F}_b + \mathbf{F}_{cl} \quad (2.18)$$

where each term denotes a force vector that consists of three elements: surge force, sway force, and yaw moment. The subscript “ice”, “br”, “b”, and “cl” refer to the total ice force, the breaking force component, the buoyancy force component, and the ice clearing force component, respectively. Eq. 2.18 can be expanded as:

$$\begin{aligned} X_{ice} &= X_{br} + X_b + X_{cl} \\ Y_{ice} &= Y_{br} + Y_b + Y_{cl} \\ N_{ice} &= N_{br} + N_b + N_{cl} \end{aligned} \quad (2.19)$$

The following sections 2.4.1 and 2.4.2 derive each term in Eq. 2.19 respectively.

2.4.1 Breaking Force Component

2.4.1.1 Ship-Ice Contact

Wang (2001) proposed a geometric Grid Method to detect the contact between the ship and the ice; Sawamura et al. (2009a) proposed a circle contact algorithm which is similar to the geometric Grid Method. These methods require discretizing the entire

domain into elements. Lau et al. (2004) came up with a DEM to deal with this issue; this method is also applied by Nguyen et al. (2009) and Su et al. (2010). The DEM only requires discretizing the ship water line and a certain segment of the ice edge. A new detecting strategy, named Polygon-Point Algorithm, is proposed in this study. It is a modification of the DEM proposed by Su et al. (2010).

The algorithm is on the basis of Ray casting method, which is a simple way of finding whether a point is inside or outside a simple polygon. Ray casting algorithm is based on a simple observation that if a point moves along a ray from the probe point to infinity and if it crosses the boundary of the polygon an odd number times, the probe point is inside the polygon. During the process of contact detecting, the ship water line is first considered as a simple polygon while the discrete ice edge is considered as scattered probe points. Every point is investigated to see if it is inside the polygon or not. After that, the ice plate will be treated as a polygon and each point on the ship water line will be investigated. Based on the detecting result, the ship-ice contact is identified as four alternative scenarios (illustrated in Figure 2.2):

- no points are involved
- contact involves points both on the ship water line and the ice edge
- contact involves points only on the ice edge
- contact involves points only on the ship water line

The first scenario means the ship does not contact with the ice while the rest scenarios denote they contact with each other.

2.4.1.2 Crushing Force

As long as the hull contacts with the ice edge, ice crushing starts at the contact point. It continues until the ice plate is broken by bending. More than one contact zone

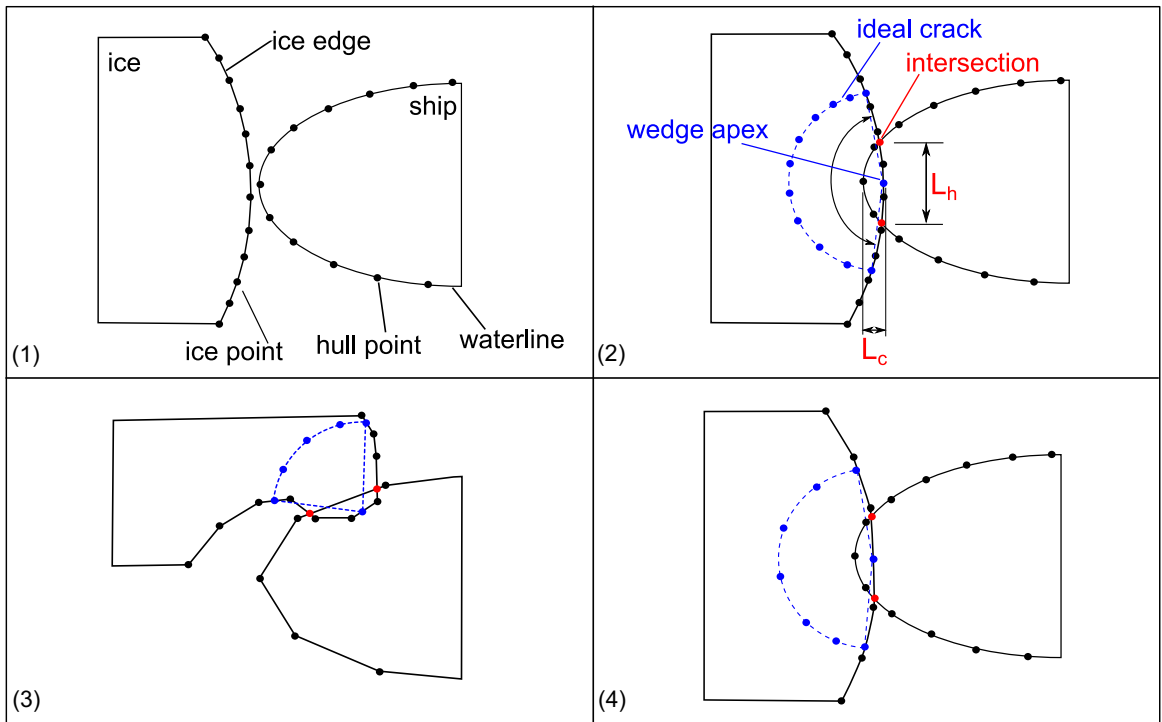


Figure 2.2: Sketch of four interaction scenarios

could exist at the same instant time. In each contact zone there is a crushing force on the hull. The value of the crushing force within one contact zone is given by:

$$F_{cr} = p_{ave} \cdot A_{cr} \quad (2.20)$$

where F_{cr} is the value of crushing force, and which is perpendicular to the contact surface and pointing inward to the ship; p_{ave} is the average pressure on the contact surface, and it is achieved by process pressure-area relationship; A_{cr} is the area of the contact surface which is numerically achieved.

(1) average pressure

Previous numerical models implement constant contact pressure (crushing strength, σ_{cr}) when calculating the crushing force (Lau et al., 2004; Liu, 2009; Martio, 2007; Nguyen et al., 2009; Sawamura et al., 2009a; Su et al., 2010; Wang, 2001). However,

analysis on Full-scale data shows that contact pressure is varying as the surface area changes. A form of power relation between average pressure and area (P-A curve or P-A relation) is widely accepted:

$$p_{ave} = p_0 \cdot A_{cr}^{ex} \quad (2.21)$$

where p_0 is the constant nominal pressure; ex is the constant exponent.

Daley (2004) stated that there are two different pressure distribution models to derive a P-A relation: spatial pressure distribution which describes the variation of pressure within the contact at one point in time; process pressure distribution which describes the pressure-area relation at different time steps. He also mentioned that a decrease trend of pressure when area increases can be observed in spatial pressure distribution, i.e., ex has a negative value; however, this trend is not necessary to process pressure distribution.

(2) contact surface area

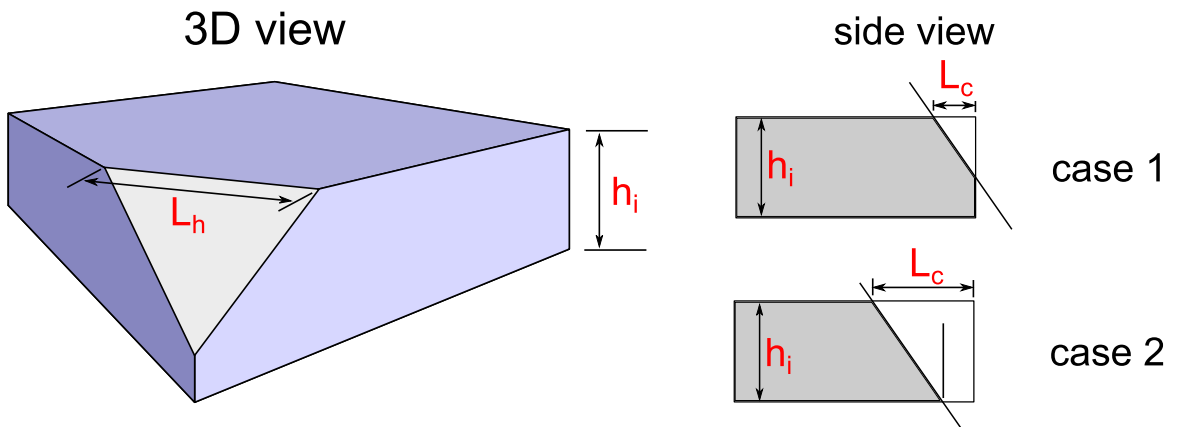


Figure 2.3: Sketch of two contact surface shapes

As illustrated in Figure 2.3, the contact surface has two shapes: triangular and trape-

zoidal. The area is given by:

$$A_{cr} = \begin{cases} \frac{1}{2} L_h \frac{L_c}{\sin(\beta')} & \text{if } L_c \leq h_i \cdot \tan(\beta') \\ \frac{1}{2} \left[L_h + L_h \frac{L_c - h_i / \tan(\beta')}{L_c} \right] \frac{h_i}{\cos(\beta')} & \text{if } L_c \geq h_i \cdot \tan(\beta') \end{cases} \quad (2.22)$$

where L_h is the maximum width of the contact surface; L_c is the maximum penetration; h_i is ice thickness; β' is normal frame angle of the hull. L_h and L_c are determined from Polygon-Point Algorithm.

2.4.1.3 Frictional Force

Besides the crushing force, the friction, which is related to relative velocity between the ship and the ice as the ice slides along the hull, should also be considered. Both the crushing force and the friction should be decomposed into three components that coincide with the three axes of the ship-fixed frame. The method proposed in Su et al. (2010) is applied to calculate the friction. It is assumed that the friction, which is proportional to crushing force, consists of two parts (shown in Figure 2.4): one is in horizontal plane, and the other is in vertical plane. The value of each component was related to the corresponding relative velocity:

$$f_h = \mu F_{cr} \frac{v_\tau}{\sqrt{v_\tau^2 + v_{n,1}^2}} \quad (2.23)$$

$$f_v = \mu F_{cr} \frac{v_{n,1}}{\sqrt{v_\tau^2 + v_{n,1}^2}} \quad (2.24)$$

where μ is the frictional coefficient; v_τ is the tangential relative velocity in horizontal plane; $v_{n,1}$ is the relative velocity along the hull in normal section; f_h and f_v are the horizontal and vertical frictional forces, respectively, and their directions are illustrated in Figure 2.4.

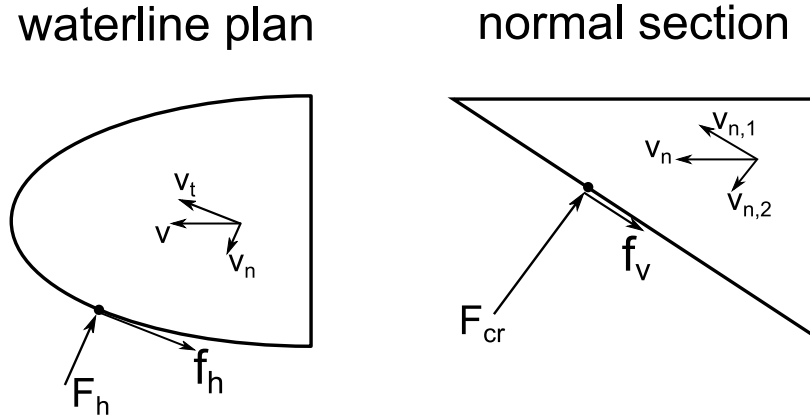


Figure 2.4: Directions of force and velocity components

2.4.1.4 Breaking Force

Sections 2.4.1.1 to 2.4.1.3 provide the method to achieve the ice force (crushing force and frictional force) within one contact zone. To obtain the total ice force, i.e., the breaking force, the crushing force and frictional force have to be projected onto ship-fixed coordinate system. Based on previous analysis, the projected components are given by:

$$X_{br} = \left[\sin(\beta') \tan(\alpha) + \mu \sqrt{1 + \tan^2(\alpha) \cos^2(\beta')} \right] \cdot F_{cr} \quad (2.25)$$

$$Y_{br} = \left[\sin(\beta') - \mu \tan(\alpha) \frac{\cos(\alpha) - \cos^2(\beta')}{\sqrt{\cos^2(\alpha) + \sin^2(\alpha) \cos^2(\beta')}} \right] \cdot F_{cr} \quad (2.26)$$

$$Z_{br} = \left[\cos(\beta') - \mu \frac{\sin(\alpha) \sin(\beta') \cos(\beta')}{\sqrt{\cos^2(\alpha) + \sin^2(\alpha) \cos^2(\beta')}} \right] \cdot F_{cr} \quad (2.27)$$

where α is the water line angle at contact location; X_{br} and Y_{br} are breaking force components that are in the horizontal plane; Z_{br} is the vertical breaking force component that is perpendicular to the horizontal plane. Z_{br} is further compared to bearing capability of the ice plate to investigate whether bending failure will happen or not.

The breaking yaw moment is given by:

$$N_{br} = -X_{br} \cdot y + Y_{br} \cdot x \quad (2.28)$$

where x and y are coordinates of the contact point that refer to $o-xyz$ frame.

The total ice breaking force is achieved by integrating all the crushing and frictional forces along the hull.

2.4.1.5 Breaking by Bending

The vertical force component increased as the ship is penetrating into the ice plate. As long as it exceeds the bearing capability of the ice sheet, bending failure would happen and a circular ice floe would be broken off the plate. The bearing capability is calculated by Kashtelyan (Kerr, 1976):

$$P_{bear} = C_f \left(\frac{\theta}{\pi} \right)^2 \sigma_f h_i^2 \quad (2.29)$$

where θ is the open angle of the ideal ice wedge as illustrated in Figure 2.2; σ_f is the flexural strength of the ice; C_f is an empirical coefficient. The above formula expresses the bearing capacity in quasi-static condition that is fail to consider the effect of ship velocity. It is only suitable for low velocity cases. However, the ice plate dynamics is beyond the scope of the current study; therefore, we assume the above formula fits all velocity range.

Kashtelyan (Kerr, 1976) suggested a small value (around 1.0) for the constant parameter, C_f , while Nguyen et al. (2009) used a value of 4.5 with no explanation. In Su et al. (2010), a study of determining C_f was carried out and a value of 3.1 was finally adopted. The coefficient is considered tunable in this study.

2.4.1.6 Ice Edge Updating

As long as both vertical breaking force, Z_{br} , and the bearing capability of the ice, P_{bear} , are obtained, flexural failure can be investigated. If $Z_{br} \leq P_{bear}$, the ice edge will only be crushed; otherwise, flexural failure will happen. A circular shaped ice piece will be broken off the plate. Figure 2.5 shows the ice plate breaks and updates pattern of a 1:21.8 scale Terry Fox ship model in a simulated towed straight motion test. The red points and segments represent the new generated ice edge, while the blue points and segments are current ice edge. It can be seen that three updating zones exist at the same time: one is at the stem, and the other two are at shoulder region. It is also clear to see that the updating zones at shoulder region do not involve discrete points on the ship waterline.

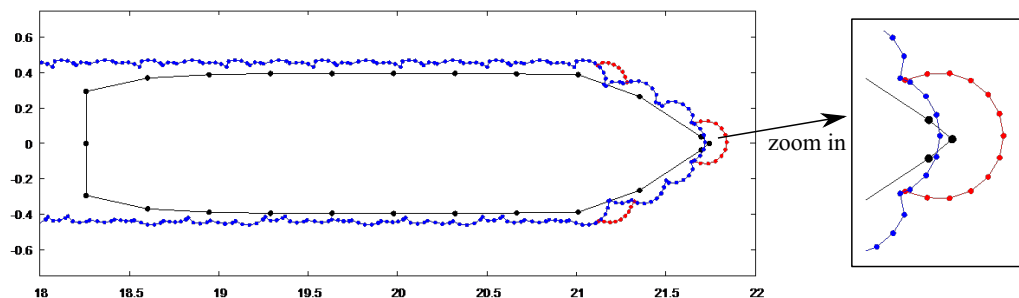


Figure 2.5: Ice edge update in a simulated tow test of a 1:21.8 scale Terry Fox ship model

The size of the ice floe mainly depends on the characteristic length of the ice and the relative velocity component that is perpendicular to the contact surface. It is determined by Wang (2001) formula:

$$R = C_l \cdot l(1 + C_v \cdot v_{n,2}) \quad (2.30)$$

where $v_{n,2}$ is the relative velocity component that is normal to the contact surface; C_l

and C_v are tunable coefficients. C_l has a positive value, and C_v has a negative value. l is the characteristic length of the ice that is given by:

$$l = \left[\frac{Eh_i^3}{12(1 - \nu^2)\rho_w g} \right]^{1/4} \quad (2.31)$$

where E is Young's modulus of the ice; ν is Poisson's ratio; ρ_w is sea water density; g is gravitational acceleration.

2.4.1.7 Effect of Ice Flexural Deflection

Valanto (1989) reported a rapid flexural failure was observed in the experiment when flexural strength ratio had a large value ($E/\sigma_f = 6400$), while in low ratio case ($E/\sigma_f = 1400$), considerably more time was required. Valanto also pointed out that the difference was important since it would significantly affect the average ice resistance. However, in previous works (Nguyen et al., 2009; Su et al., 2010; Wang, 2001), a rigid ice plate model was assumed so that vertical deflection by bending was not considered. This model was unable to simulate what was observed in Valanto's experiment.

The real ice dynamics during the interaction is quite complex. According to Daley (2010) and Enkvist et al. (1979), a high pressure zone forms under the bottom of the ice sheet and provides additional support against the ice deflection. The high pressure zone depends on the velocity of the downward deflected ice sheet and the acceleration force of the ice mass and the entrained mass of water (Enkvist et al., 1979). In addition, during the interaction both the vessel and the ice have vertical movement which results in the 3DOF model insufficient.

However, we can avoid the dynamic pressure and the vertical movement of the vessel and develop a relatively simplified model to study the effect of ice deflection on the

interaction.

Water under the ice sheet is considered as an elastic foundation. As the ship is moving forward, the ice plate will be bent. Since ice deflection is small comparing to ice characteristic length, we further assume a parallel downward movement of ice plate instead of bending. The contact force, F_{cr} , leads to ice crushing and flexural deflection simultaneously.

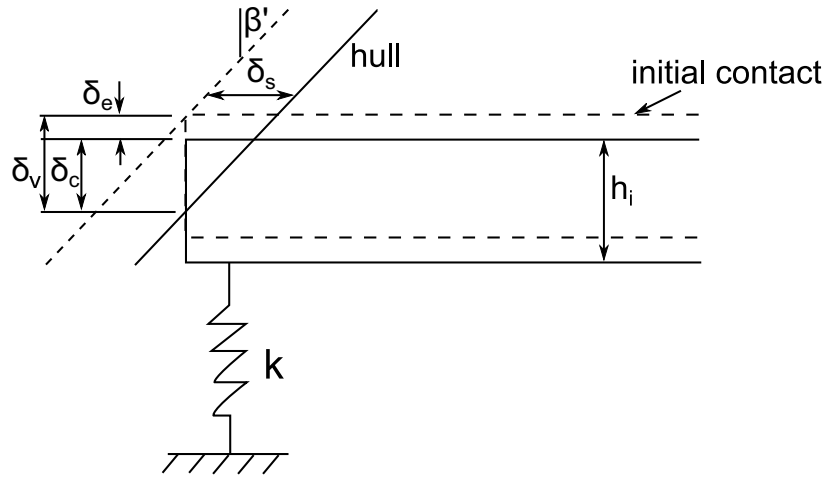


Figure 2.6: Flexural deflection of the ice plate

As illustrated in Figure 2.6, the ship penetrates into the ice by δ_s from the initial contact time instant to the calculating time instant, resulting in a vertical elastic deflection, δ_e , and a vertical crushing height, δ_c . They satisfy the following equation:

$$\delta_e + \delta_c = \delta_s \cdot \tan(\beta') \quad (2.32)$$

δ_e and δ_c are caused by the same force, the vertical component of F_{cr} . Therefore, they must satisfy:

$$F_{cr,v} = f_1(\delta_c) = f_2(\delta_e) \quad (2.33)$$

where $f_1(\cdot)$ is given by Eqs. 2.20, 2.21, 2.22, and 2.27; $f_2(\cdot)$ is obtained by considering the dynamics of an infinite ice plate to a concentrated load. The dynamic equation

is given by:

$$\frac{d^4w}{dx^4} + 2\frac{d^4w}{dx^2dy^2} + \frac{d^4w}{dy^4} = \frac{P - \rho_w g w}{D} \quad (2.34)$$

where w is the deflection of the ice plate; P is the concentrated load; D is the flexural rigidity of the ice plate that is given by

$$D = \frac{Eh_i^3}{12(1 - \nu^2)} \quad (2.35)$$

The maximum deflection, w_{max} , exists where the concentrated load is placed and is given by

$$w_{max} = \frac{P}{8\sqrt{\rho_w g D}} \quad (2.36)$$

Consider that the crushing force is placed at the apex of an ice wedge with the open angle of θ , $f_2(\cdot)$ is given by

$$F_{cr,n} = \frac{2\pi}{\theta} \cdot 8\sqrt{\rho_w g D} \cdot \delta_e \quad (2.37)$$

As long as $f_1(\cdot)$ and $f_2(\cdot)$ are obtained, Eqs. 2.32 and 2.33 can be combined to solve δ_c and δ_s . According to triangular similarity, the contact surface area is modified by multiplying $(\delta_c/\delta_v)^2$, i.e., the effect of ice flexural deflection diminishes the contact area.

2.4.2 Clearing and Buoyancy Force Components

The ice resistance (x-component) due to buoyancy and clearing is calculated by Spencer and Jones (2001):

$$X_{cl} = C_{cl} F_h^{EX_{cl}} \rho_i B h_i u^2 \quad (2.38)$$

$$X_b = C_b \rho_{\Delta} g h_i B T \quad (2.39)$$

where $F_h = u/\sqrt{gh_i}$ is the ice Froude number; B is the ship beam; T is the ship draft; ρ_i is the ice density; ρ_Δ is the density difference between ice and sea water; C_{cl} , C_b , and EX_{cl} are empirical coefficients from model tests.

To derive the model of y-component of buoyancy and clearing forces, we assume the effect of buoyancy and clearing forces on sway direction are equivalent to three concentrated loads: one is acting somewhere on the parallel midship body, denoted with the subscript of "mid", and the other two are on each side of bow, denoted with the subscript of "bow". Under the assumption of port-starboard symmetry in ship geometry, each bow force is given by:

$$Y_{i,bow} = \frac{Y_{br}}{X_{br}} \cdot \frac{X_i}{2} \quad (2.40)$$

where subscript "i" is either "cl" or "b", representing either clearing force component or buoyancy force component; X_{br} and Y_{br} are x-component and y-component due to ice breaking given by Eqs. 2.25 and 2.26, respectively. Therefore,

$$Y_{i,bow} = \frac{X_i}{2} \cdot \frac{\sin(\beta') - \mu \tan(\alpha) \frac{\cos(\alpha) - \cos^2(\beta')}{\sqrt{\cos^2(\alpha) + \sin^2(\alpha) \cos^2(\beta')}}}{\sin(\beta') \tan(\alpha) + \mu \sqrt{1 + \tan^2(\alpha) \cos^2(\beta')}} \quad (2.41)$$

The net sway force at bow would be:

$$\Delta Y_{i,bow} = Y_{i,bow,port} + Y_{i,bow,starboard} \quad (2.42)$$

If the ship is moving straight forward, due to the symmetrical geometry and movement, the ice load should also be symmetrical, i.e., the net sway force at bow should be zero. However, when the ship starts to turn, the load on each sides will no longer be the same.

We can also achieve the concentrated load on the midship by assuming the load is

proportional to its corresponding motion velocity:

$$Y_{i,mid} = C_{mid} \cdot X_i \cdot \frac{v}{u} \quad (2.43)$$

where C_{mid} is an empirical coefficient.

To summarise, the sway force due to either clearing or buoyancy can be achieved by:

$$Y_i = \Delta Y_{i,bow} + Y_{i,mid} \quad (2.44)$$

where $\Delta Y_{i,bow}$ is given by Eq. 2.42, and $Y_{i,mid}$ is given by Eq. 2.43

2.5 Hydrodynamic Force

The hydrodynamic force is assumed to just depend on velocity and acceleration components that is well known as “quasi-steady approach”. The part that is associated with acceleration is named added mass, and the part that is associated with velocity is known as damping. According to Fossen (2011), Perez and Blanke (2002) and Gong (1993), the hydrodynamic forces and moment are given by:

$$X_H = -X_{\dot{u}}\dot{u} + X(u) + (Y_{\dot{v}} + X_{vr})vr \quad (2.45)$$

$$Y_H = -X_{\dot{u}}ur - Y_{\dot{v}}\dot{v} - Y_{\dot{r}}\dot{r} + Y_vv + Y_r r + Y_{v|v}|v| + Y_{r|r}|r| + Y_{vr}vr \quad (2.46)$$

$$\begin{aligned} N_H = & -N_{\dot{r}}\dot{r} - N_{\dot{v}}\dot{v} + N_vv + N_r r + N_{vr}vr + N_{v|v}|v| + N_{vvr}vvr + N_{vrr}vrr \\ & + N_{r|r}|r| + x_G(Y_vv + Y_r r + Y_{vr}vr + Y_{v|v}|v| + Y_{r|r}|r|) \end{aligned} \quad (2.47)$$

The coefficients are known as hydrodynamic coefficients. They are formulated as partial derivatives of the force under consideration with respect to the multiplicand motion variables. They can be determined by model test, CFD method, or analytical

formulas (Gong, 1993). $X(u)$ represents water resistance and is calculated by Holtrop and Mennen's initial design prediction method (Holtrop and Mennen, 1982) which can be seen in Appendix A.

2.6 Propeller Thrust

We consider the propeller is operating in the first quadrant, i.e., both the ship speed and the shaft revolution correspond to ahead progress. By avoiding the propeller rotating in oblique flow or asymmetrical wake, the effect on sway force and yaw moment can be neglected. Hence:

$$Y_P = N_P = 0 \quad (2.48)$$

According to ITTC (2002), the mathematical model for propeller thrust is given by:

$$X_P = (1 - t)\rho_w n^2 D_P^4 K_T(J_P) \quad (2.49)$$

where t is the thrust deduction that accounts for the interaction between the hull and the propeller; n is shaft speed in unit of revolution per second (rps); D_P is the propeller diameter; J_P is advance coefficient given by Eq. 2.50; K_T is the thrust coefficient of the propeller given by Eq. 2.51.

$$J_P = \frac{u(1 - w_P)}{nD_P} \quad (2.50)$$

where w_P is the wake fraction coefficient.

$$K_T = a_0 + a_1 \cdot J_P + a_2 \cdot J_P^2 \quad (2.51)$$

where a_0 , a_1 , and a_2 are coefficients.

2.7 Rudder Force

The mathematical model of the rudder force can be seen in (Bhawsinka, 2011; Gong, 1993; Hirano, 1981; Toxopeus, 2011). The derivative of the model is out of the scope of the present thesis. The rudder force is given by:

$$X_R = -(1 - t_R)F_N \sin(\delta) \quad (2.52)$$

$$Y_R = -(1 + \alpha_H)F_N \cos(\delta) \quad (2.53)$$

$$N_R = -(x_R + \alpha_H x_H)F_N \cos(\delta) \quad (2.54)$$

where δ is the rudder deflection; t_R is the rudder drag correction factor; x_R is the x-coordinate of the rudder with respect to $o - xyz$; α_H and x_H are coefficients that account on hull-rudder interaction; F_N is the rudder normal force given by:

$$F_N = \frac{1}{2} \rho \frac{6.13\Lambda}{\Lambda + 2.25} A_R U_R^2 \sin(\alpha_R) \quad (2.55)$$

where Λ is the rudder aspect ratio; A_R is the projected rudder area; U_R is the effective rudder inflow; α_R is the effective rudder inflow angle.

2.8 Summary

This chapter derives a 2D ship-ice interaction model. The model directly simulates the physical ice-hull interaction process in time-domain by empirical approach with numerical implementation. This model is capable of simulating various tests.

Chapter 3

Guidance and Control System

3.1 General

One important manoeuvring problem in many offshore applications is to steer a vessel, a submersible or a rig along a desired route with a prescribed speed (Fossen et al., 2003). This is further specified as two tasks: the Geometric Task, which is to converge to and follow a desired route or path (usually defined parametrized or in terms of way-points); and the Dynamic Task, which is to satisfy a speed assignment (defined in terms of a prescribed speed) along the path (Skjetne et al., 2011). The motion control system that is assigned to implement the pre-mentioned tasks is known as Autopilot or Auto-steering gear.

When designing a control system for a vessel, it is important to distinguish between fully actuated vessel and underactuated vessel. According to Fossen (2011), a fully actuated vessel has equal or more independent control inputs than the number of DOF of the vessel, while an underactuated vessel has less independent control inputs than the number of DOF.

For slow speed control of floating rigs and supply vessels, fully actuated is commonly

referred to as dynamic positioning (DP) where control forces and moments are available in all 3DOFs (surge, sway, and yaw). However, conventional ships are usually equipped with main propellers for forward speed control and rudders for turning control. This means only two independent control inputs are available so that it is specified as an underactuated situation.

One solution to a conventional and underactuated vessel is to reduce the output space from 3DOF to 2DOF, and leave the other uncontrolled. A autopilot system is involved to generate the commanded heading such that the cross-track error can be minimized. This can be done by including an additional cross-track error control loop or by adopting multivariable controller (Fossen et al., 2003).

The Line-of-Sight (LOS) method controller is widely used for a path-following of an underactuated vessel (Breivik, 2003; Fossen et al., 2003; Moreira et al., 2007; Skjetne et al., 2011). It generates a commanded heading signal and gradually guides a vessel to turn to the desired heading angle. The convergence to the desired heading also leads to the convergence to the desired position simultaneously. This requires only one control input and leaves the other to dynamically maintain the forward speed.

In this chapter, the guidance system and controller based on LOS method will be introduced. The output includes the commanded heading angle and surge speed. The Geometric Task is achieved by the rudder, while the Dynamic Task is performed by the main propeller. Section 3.2 derives the LOS guidance system. This includes a desired heading algorithm and a way-point switching algorithm. A reference model is also introduced in section 3.3 in order to avoid rapid change in the heading signal. The control law, which is based on the guidance system and the reference model, is provided in section 3.4.

3.2 Line-of-Sight Guidance

According to Breivik (2003, 2010) and Fossen (2011), two different methods can be applied to achieve the desired heading angle: the enclosure-based method and the lookahead-based method. This section present both methods. The lookahead-based method is further implemented due to its lower complexity in calculation.

3.2.1 Enclosure-based Method

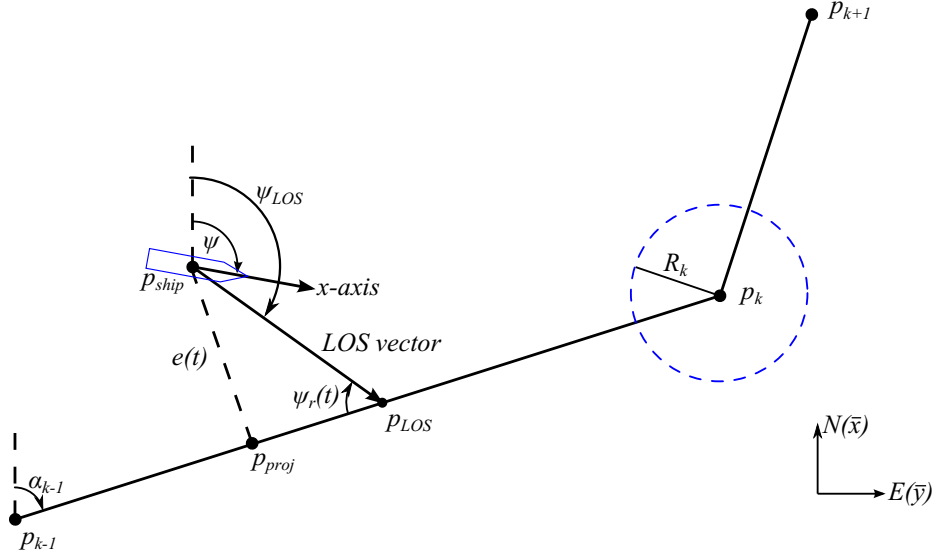


Figure 3.1: Line-of-Sight guidance principle

Figure 3.1 illustrates the principle of LOS guidance method. Assuming at a time instant t , the ship is located at $\mathbf{p}_{ship} = [\bar{x}_0, \bar{y}_0]^T$ and has a heading angle of ψ in O-NED. \mathbf{p}_{k-1} denotes the previous way-point and \mathbf{p}_k denotes the current way-point, and both are from the way-point table provided by the operator. The desired path is defined as the straight line segment between \mathbf{p}_{k-1} and \mathbf{p}_k . $\mathbf{p}_{los} = [\bar{x}_{los}, \bar{y}_{los}]^T$ is called the LOS position that is located somewhere on the path and moving towards \mathbf{p}_k . $e(t)$ is called the cross-track error. We force the ship pointing towards the LOS position all the time such that the ship location will converge to the desired path (Breivik, 2003).

The LOS angle is the heading when the ship is pointing towards the LOS position, and it is given by:

$$\psi_{los} = \text{atan2}(\bar{y}_{los} - \bar{y}, \bar{x}_{los} - \bar{x}) \quad (3.1)$$

where atan2 is the quadrant function:

$$\text{atan2}(y, x) = \begin{cases} \arctan\left(\frac{y}{x}\right) & x > 0 \\ \arctan\left(\frac{y}{x}\right) + \pi & y \geq 0, x < 0 \\ \arctan\left(\frac{y}{x}\right) - \pi & y < 0, x < 0 \\ +\frac{\pi}{2} & y > 0, x = 0 \\ -\frac{\pi}{2} & y < 0, x = 0 \\ \text{undefined} & y = 0, x = 0 \end{cases} \quad (3.2)$$

The definition of the quadrant function ensures

$$\psi_{los} \in [-\pi, \pi] \quad (3.3)$$

According to the above interpretation, the Geometric Task can be expressed as:

$$\lim_{t \rightarrow \infty} (\psi - \psi_{los}) = 0 \quad (3.4)$$

To achieve the coordinates of the LOS position, the enclosure-based method introduces a sufficient large circle enclosing the ship's current location \mathbf{p}_{ship} . The circle will intersect the desired path at two points. One of them is chosen to be the LOS points according to the direction of travel. Therefore, the following equations must be solved

online:

$$\frac{\bar{y}_{los} - \bar{y}_{k-1}}{\bar{x}_{los} - \bar{x}_{k-1}} = \frac{\bar{y}_k - \bar{y}_{k-1}}{\bar{x}_k - \bar{x}_{k-1}} = \tan(\alpha_{k-1}) \quad (3.5)$$

$$(\bar{x}_{los} - \bar{x})^2 + (\bar{y}_{los} - \bar{y})^2 = R_{los}^2 \quad (3.6)$$

\mathbf{p}_{los} is obtained by solving Eqs. 3.5 and 3.6. After that, Eq. 3.1 is used to achieve the LOS angle ψ_{los} . A controller for steering is finally applied to accomplish the Geometric Task.

3.2.2 Lookahead-based Method

To avoid solving Eqs. 3.5 and 3.6, the lookahead-based method is introduced. As illustrated in Figure 3.1, the ship location has a projection on the path, denoted as \mathbf{p}_{proj} . According to the travel direction, find the LOS position on the path which is Δ ahead the projection point. The LOS angle can be calculated in another way:

$$\psi_{los} = \psi_r(e) + \alpha_{k-1} \quad (3.7)$$

where

$$\psi_r(e) = \arctan\left(\frac{-e}{\Delta}\right) \quad (3.8)$$

where e is the cross-track error.

We assume the linear desired path has a direction from \mathbf{p}_{k-1} to \mathbf{p}_k in Figure 3.1, and it can be expressed in mathematical form as:

$$ax + by + c = 0 \quad (3.9)$$

where a , b , and c are coefficients that can be determined by the coordinates of \mathbf{p}_{k-1}

and \mathbf{p}_k . Hence, the cross-track error can be achieved by:

$$e(t) = \frac{a\bar{x}_0 + b\bar{y}_0 + c}{\sqrt{a^2 + b^2}} \quad (3.10)$$

where \bar{x}_0 and \bar{y}_0 are the coordinates of \mathbf{p}_{ship} . It is easy to notice that if the ship location is on the left side of the path, $e(t) < 0$; if it is on the right side, $e(t) > 0$; if it is right on the path, $e(t) = 0$.

The lookahead-based method and the enclosure-based method could be identical if we apply a time variant $\Delta(t)$ that satisfies:

$$e(t)^2 + \Delta(t)^2 = R_{los}^2 \quad (3.11)$$

Hence, $\Delta(t)$ is determined by:

$$\Delta(t) = \sqrt{R_{los}^2 - e(t)^2} \quad (3.12)$$

According to Fossen (2011), Eq. 3.8 can be expressed as a proportional control law:

$$\psi_r(e) = \arctan(-K_{pr}e) \quad (3.13)$$

where $K_{pr} = 1/\Delta > 0$.

A integral term and a differential term can be added so that ψ_r will be calculated by a PID controller which is able to increase the response and minimize the steady error:

$$\psi_r(e) = \arctan\left(-K_{pr}e - K_{dr}\dot{e} - K_{ir}\int_0^t e(\tau)d\tau\right) \quad (3.14)$$

where $K_{dr} > 0$ is the differential gain, and $K_{ir} > 0$ is the integral gain.

As long as ψ_r is determined, Eq. 3.7 is used to calculate the LOS angle. α_{k-1} is the

heading angle of the path that is given by:

$$\tan(\alpha_{k-1}) = \frac{\bar{y}_k - \bar{y}_{k-1}}{\bar{x}_k - \bar{x}_{k-1}} \quad (3.15)$$

3.2.3 Way-point Switching Algorithm

A criteria for updating desired path from $\mathbf{p}_{k-1}\mathbf{p}_k$ to $\mathbf{p}_k\mathbf{p}_{k+1}$ is implemented by introducing a circle of acceptance located at the current way-point \mathbf{p}_k . The circle is illustrated in Figure 3.1. If the ship's location \mathbf{p}_{ship} at some instant satisfies:

$$(\bar{x}_k - \bar{x})^2 + (\bar{y}_k - \bar{y})^2 \leq R_k^2 \quad (3.16)$$

the current way-point will be updated to the next way-point in the way-point table. R_k denotes the radius of the circle of acceptance at current way-point. They could be assigned an arbitrary value and stored together with the coordinates of the way-points. For simplicity, the radii are assumed constant in this study.

3.3 Reference Model

A reference model is usually required to avoid sending rapid changing signals to a controller. For the path-following purpose, the reference model is also able to filter out high frequency motions. A 2nd order reference model is applied in this study since both the desired heading angle and its time derivative are need. The 2nd order reference model is given by:

$$\frac{x_d(s)}{x_r(s)} = \frac{\omega_n^2}{s^2 + 2\xi\omega_n s + \omega_n^2} \quad (3.17)$$

where ξ is the relative damping ratio, and ω_n is the natural frequency. Eq. 3.17 is equivalent to a second order ordinary derivative equation:

$$\ddot{x}_d + 2\xi\omega_n\dot{x}_d + \omega_n^2x_d = \omega_n^2x_r \quad (3.18)$$

The 4th-order Runge-Kutta method is used to solve the ordinary derivative equation. x_d and its first order time derivative, \dot{x}_d , can be obtained from Eq. 3.18 by specifying ξ , ω_n , and the input signal x_r . After that, they will be exported to the controller.

3.4 LOS Controller

Various techniques are available for controller design in modern control theories such as PID control, linear quadratic optimal control, and backstepping control. Among all of them, the PID control is the simplest but practical one so that it is widely used in industrial systems. Due to the decoupling of surge motion from sway and yaw motions, i.e., the speed control is separated from steering control, separated Single-Input-Single-Output (SISO) PID controllers will be designed to accomplish the Geometric Task and the Dynamic Task in this section. The strategy of feedback is applied in the design.

As mentioned, the Geometric Task can be expressed as:

$$\lim_{t \rightarrow \infty} (\psi - \psi_{los}) = 0 \quad (3.19)$$

Similarly, the Dynamic Task can be expressed as:

$$\lim_{t \rightarrow \infty} (u - u_{sp}) = 0 \quad (3.20)$$

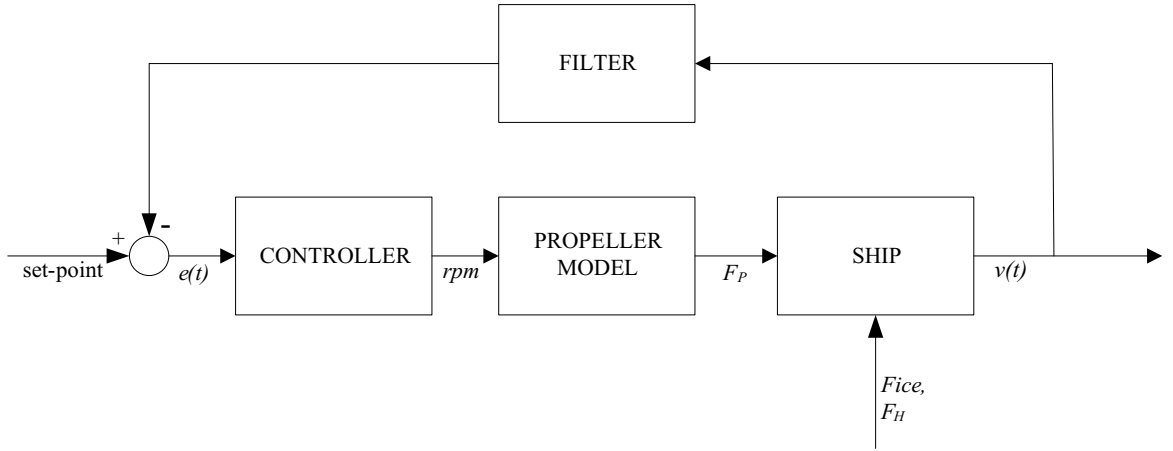


Figure 3.2: Diagram of the speed control feedback loop

Figure 3.2 illustrates the diagram of speed control system. The speed set-point is assumed constant and provided by the operator. The feedback speed signal must go through a filter to filter out high frequency component. The speed difference between the filtered speed and the set-point will be imported into the controller to generate the commanded shaft resolution. After that, Eq. 2.49 is applied to obtain the propeller thrust. Finally, the equations of the ship motions are solved to achieve a new speed. We define the filtered speed is denoted as \hat{u} , the speed difference is denoted as $\tilde{u} = u_{sp} - \hat{u}$. Hence, the PID control law for speed is given by:

$$\tau_1 = K_{p1} \cdot \tilde{u} + K_{d1} \cdot \dot{\tilde{u}} + K_{i1} \int \tilde{u} dt \quad (3.21)$$

where τ represents the output command signal, K_p , K_d , and K_i are the proportional gain, the derivative gain, and the integral gain, respectively, and the subscript “1” represents the surge speed control. Since the speed set-point is constant, it is easy to find that

$$\dot{\tilde{u}} = -\dot{u} \quad (3.22)$$

Similarly, the PID control law for steering is given by:

$$\tau_3 = K_{p3} \cdot \tilde{\psi} + K_{d3} \cdot \dot{\tilde{\psi}} + K_{i3} \int \tilde{\psi} dt \quad (3.23)$$

where $\tilde{\psi} = \psi_{ref} - \psi$ is the heading difference.

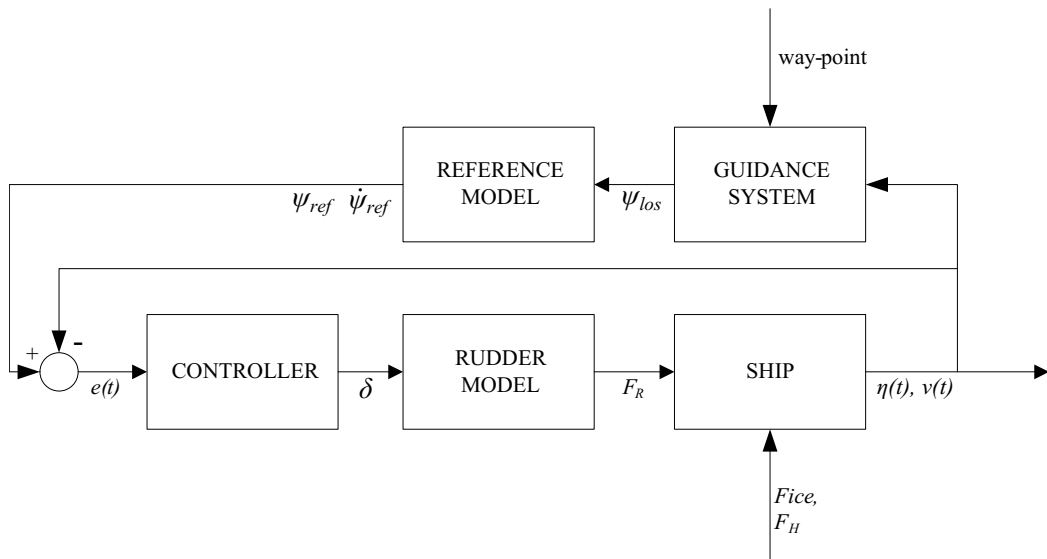


Figure 3.3: Diagram of the steering control feedback loop

The ψ_{ref} is the reference heading which is generated by the guidance system based on the input way-point table. Due to the existence of the reference model illustrated in Figure 3.3, the time derivative of the reference heading is available; hence, the time derivative of heading difference is given by:

$$\dot{\tilde{\psi}} = \dot{\psi}_{ref} - \dot{\psi} \quad (3.24)$$

3.5 Summary

This chapter introduces the LOS guidance system and two SISO PID controllers for a ship to converge to the desired path as well as maintaining the required speed. The

path is generated by the guidance system based on the operator-defined way-point table. Low pass filters and the reference model are applied prior to the controllers to filter out high frequent components of the signals and to avoid rapid change in signals.

Chapter 4

Numerical Implementation of the Model

This chapter presents the numerical simulation program developed as part of the research. The program is implemented with programming language FORTRAN 90, under Linux operating system.

Various tests can be simulated by using this program. They can be categorized as Planar Motion Mechanism (PMM) tests, manoeuvring tests, and control-involved tests. The ship can be simulated either in open water or in level ice. Table 4.1 lists all the applicable tests.

Table 4.1: simulation test matrix

	item	numbering	in water	in ice
PMM tests	straight	1		×
	pure sway	2		×
	pure yaw	3		×
Manoeuvring tests	straight	4	×	×
	turning circle	5	×	×
Control involved test	path-following	7	×	×

The program is developed as modules, i.e., each particular function is enveloped

in a module so that it is easy to use or be replaced. The major modules include: “lib_level_ice.mod” which is to simulate the hull-ice interaction, “line_of_sight.mod” which is to apply LOS guidance method, “controller.mod” which is to achieve required shaft resolution and rudder deflection angle, “hydrodynamics.mod” which is to calculate hydrodynamic force, “control_force.mod” which is to calculate propeller thrust and rudder force, “statederive.mod” which is to solve 3DOF equations of the ship motions, and “selection.mod” which is to select a prescribed test to simulate.

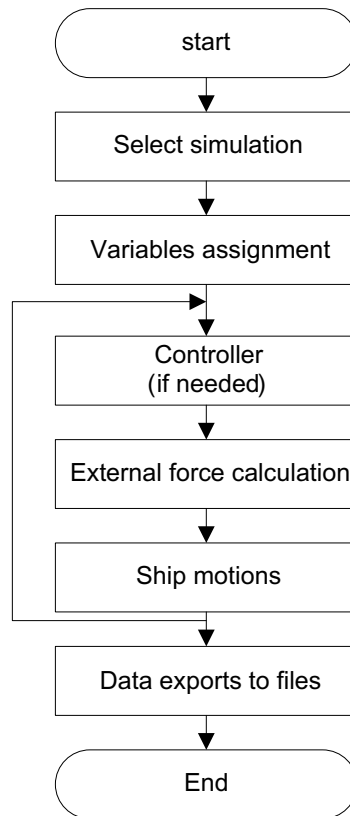


Figure 4.1: flow chart of the main routine

A main routine is also developed, and those pre-mentioned modules are used in this routine. Figure 4.1 illustrates the flow chart of the main routine. Each block in the chart will call one or more subroutines to accomplish a certain task. For instance, the block, “external force calculation”, is to achieve the total force acting on the

ship. It calls three modules at each point in time: “lib_level_ice.mod” for ice load, “hydrodynamics.mod” for hydrodynamic force, and “control_force.mod” for propeller thrust and rudder force.

The main contributions of the study are to develop a numerical method of hull-ice interaction and a guidance and controller system for automatical operation. Section 4.1 and 4.3 will introduce the numerical implementation of these two parts. Others, such as ship motions, hydrodynamics, and propeller and rudder, will not be included in this chapter.

4.1 Ship-Ice Interaction

As discussed in section 2.4, ice load is decomposed into three components: breaking term, buoyancy term, and clearing term. The first term is determined numerically, while the latter two are achieved by empirical formulas. Hence, two separate subroutines are developed.

Figure 4.2 shows the flow chart of the subroutine that is to obtain breaking force. First, it reads kinematic and geometric data such as position, velocities, and the coordinates of the discretized points on the ice edge and the ship water line. All the data is then transformed from either $O-NED$ frame or $o_i-x_iy_iz_i$ frame to $o-xyz$ frame. After that, contact scenarios is detected. If the ship does not contact with the ice plate, the ice load is assigned as zero. However, if the ship contacts with the ice plate, the first contact zone will be identified, and the ice load, as well as ice bending capability, will be calculated. The bending capability is then compared to the vertical force component to determine if breaking happens. If the bending capability is exceeded by the vertical force, this contact zone will be stored for updating, and the investigation will be moved to the next contact zone until the last one is investigated.

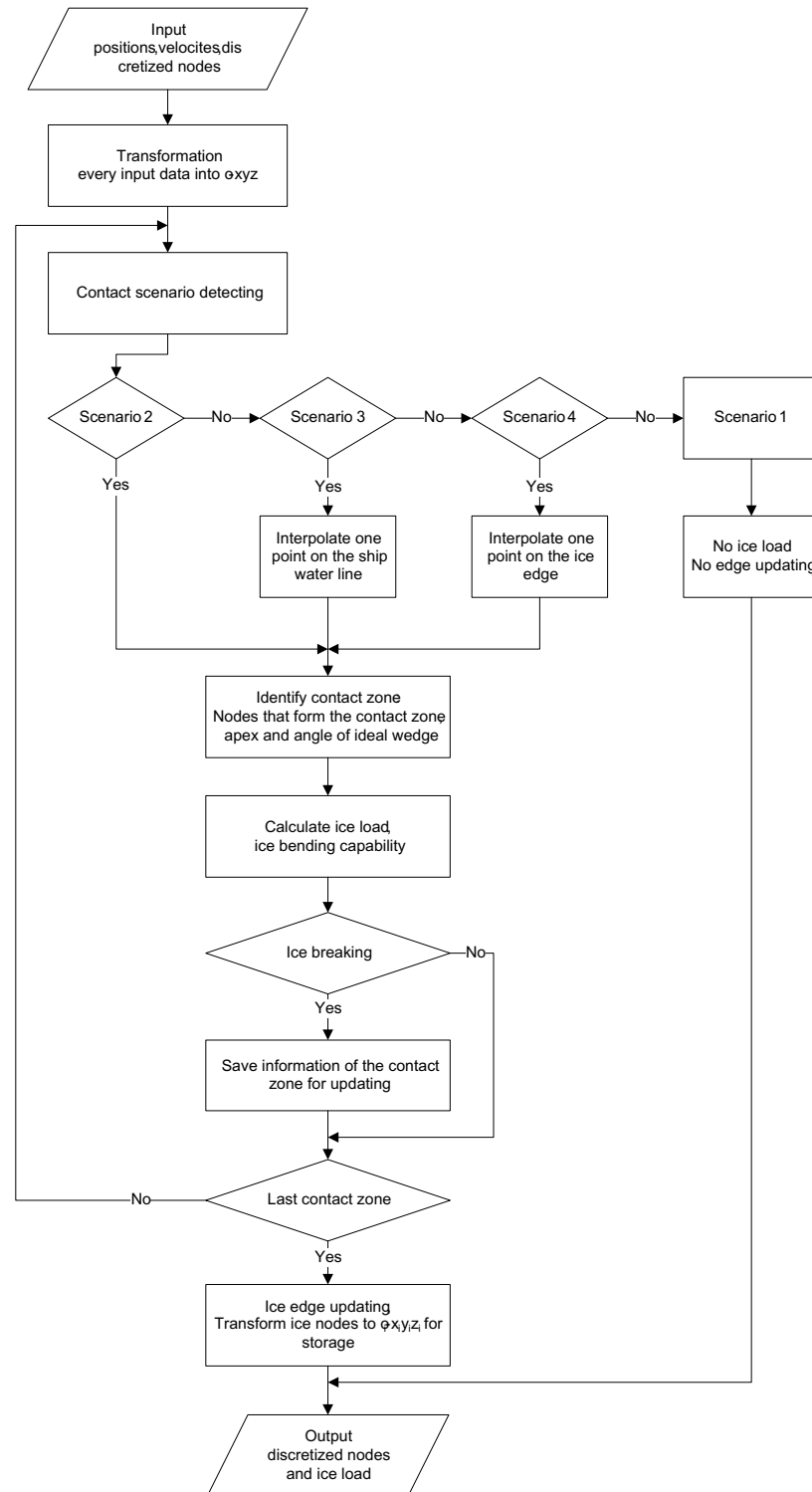


Figure 4.2: flow chart of ship-ice interaction

The ice edge will be updated when all the contact zones are finished, and the new coordinates are transformed back to $o_i-x_iy_iz_i$ frame. Finally, the 3DOF ice load and the new ice edge will be exported.

The other subroutine which is to obtain buoyancy term and clearing term is much easier than the previous one. It reads ship velocities as input and implements Eq. 2.38 to 2.44. It outputs buoyancy force and clearing force in 3DOF.

4.2 Contact Detecting and Ice Edge Updating

To numerical implement the Point-in-Polygon algorithm to detect the interaction area is the core issue to this simulation. In order to conduct the simulation effectively, a certain segment ice edge is stored (three times of the ship waterline length) and discretized into a constant number of points, which is dependent on total segment length and the discrete length. The ship waterline is also discretized into a constant number of points which is simply dependent on the offset table. A flag variable is assigned to each point to represent if it is involved in the interaction. For example, if the flag variable has a value of +1, it is involved in the interaction; but if the variable is -1, the point is not involved.

At the beginning of each computational step, all the flag variables will be assigned +1 or -1. Different contact zones and their included points can be easily identified by check the value of the corresponding flag variables. After that, analysis of interaction force is conducted within one contact zone followed by another. If within one contact zone, the vertical force exceeds the ice plate bearing capacity, the involved ice discrete points will be temporally stored. They will be used for ice edge updating after every contact zone has been analysed.

Ice edge update starts when the analysis of the interaction has been completed as

illustrated in Figure 2.5. The open angle of the ideal wedge will be achieved based on those saved discrete points, Eq. 1.12 will be used to obtain the new circumferential crack, and the crack will be discretized into points. In order to maintain the number of the total ice discrete points, the number of new generated points will be compared to the number of the involved points. If more points should be generated, some points behind the ship, which will not be involved in the interaction, will be exported to file and deleted. There will be a shift among the points in order to insert the new points in the right place. However, if less points will be generated, the discrete length will be modified to ensure the number of new points is the same as the number of involved points. If this is the case, new points will replace the old ones so that there is no points shift nor points export. When update has been completed, simulation time will increase by one time step and the same procedure will be repeated.

4.3 Mapping for LOS guidance system

This section is mainly based on Breivik (2003). The lookahead-based method is applied in the program since it is less complex in calculation. Hence, Eqs. 3.7, 3.10, and 3.14 are implemented.

The atan2-function is used in Eq. 3.14 which results in discontinuity of $\psi_r(e)$ at the $-\pi/\pi$ -junction (i.e., the LOS angle, ψ_{los} , is discontinuous at $(-\pi + \alpha_{k-1})/(\pi + \alpha_{k-1})$ -junction). If the path is predefined such that the $\psi_r(e)$ must cross the $-\pi/\pi$ -junction at some instant, inappropriate performance will be observed.

For convenience, we consider a case that $\alpha_{k-1} = 0$; hence, the LOS angle is also discontinuous at $-\pi/\pi$ -junction. At the current instant, the LOS angle is given as ψ_1 in the third quadrant in Figure 4.3. At the next instant, the angle is given as ψ_2 in the fourth quadrant. practically, the ship should turn counter-clockwise and go across

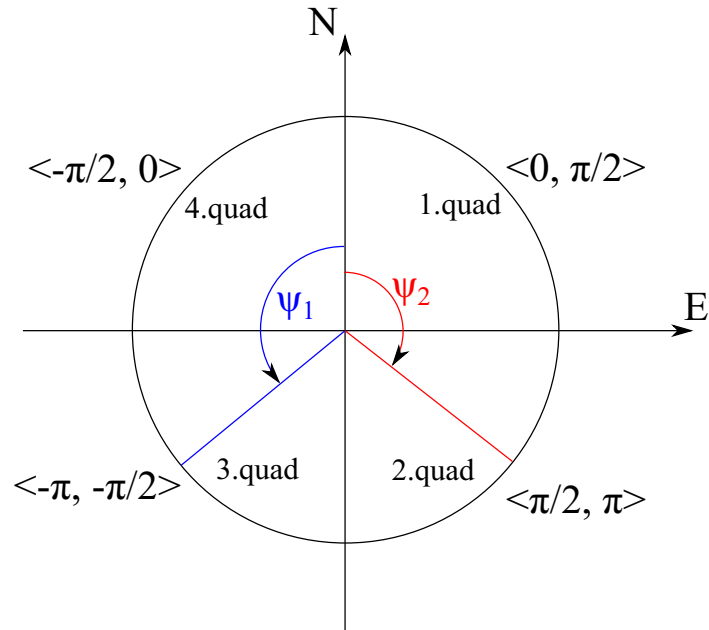


Figure 4.3: Definitions of quadrants

the negative N -axis to ψ_2 ; however, due to the discontinuity at the junction, the ship will turn clockwise towards ψ_2 . Figure 4.4 illustrate this phenomenon. The blue line represents the desired path, and it is set keeping changing across the $-\pi/\pi$ -junction. The red line and the orange line represent the ship actual tracks that one is with the mapped LOS guidance and the other is with the non-mapped LOS guidance. It is obvious that without a mapping function, the ship is unable to turn across the junction.

The discontinuity problem can be solved by adopting a mapping for the LOS angle from $[-\pi, \pi]$ to $[-\infty, \infty]$. The continuous angle is further used for control purpose. As mentioned by Breivik (2003), “memory variables” are required when mapping a narrower region, such as $[-\pi, \pi]$ to a wider region, such as $[-\infty, \infty]$. Consider a unity circle as shown in Figure 4.3. It is evenly divided into four quadrant, and they are consecutively numbered clockwise as in the figure. Consider two LOS angles: one, denoted as ψ_{last} , is for the previous instant, and the other, denoted as ψ_{now} , is for

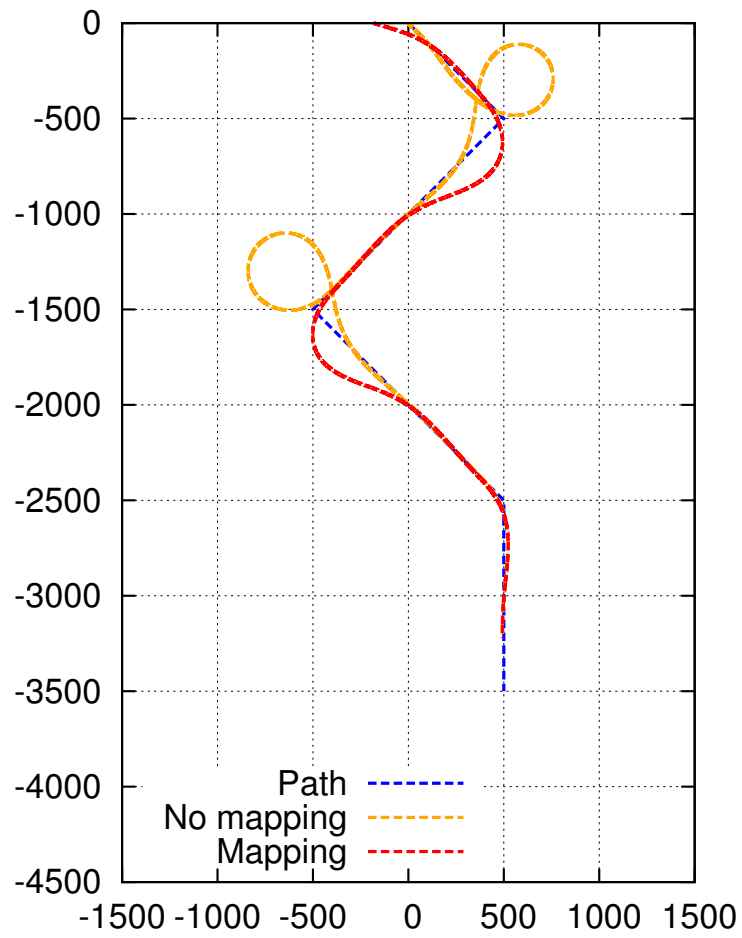


Figure 4.4: Comparison between mapped guidance and non-mapped guidance

the current instant. The variable that is to store LOS angle change is denoted as $\Delta\psi$. Another variable, denoted as $\psi_\Sigma \in [-\infty, \infty]$, is to store the accumulative and continuous LOS angle. It must be pointed out that

$$\Delta\psi \neq \psi_{now} - \psi_{last} \quad (4.1)$$

in general due to $-\pi/\pi$ discontinuity. 16 different cases are specified to achieve $\Delta\psi$ based on the relationship between ψ_{now} and ψ_{last} .

- case 1 to case 4: if ψ_{last} is in the first quadrant
 - ψ_{now} is in the first quadrant, $\Delta\psi = \psi_{now} - \psi_{last}$, i.e., the angle either increases or decreases without crossing the junction;
 - ψ_{now} is in the second quadrant, $\Delta\psi = \psi_{now} - \psi_{last}$, i.e., the angle increases without crossing the junction;
 - ψ_{now} is in the third quadrant, if ψ_{now} satisfies

$$|\psi_{now}| + \psi_{last} \leq \pi \quad (4.2)$$

$\Delta\psi = \psi_{now} - \psi_{last}$, which indicates the angle decreases without crossing the junction; otherwise, $\Delta\psi = \psi_{now} - \psi_{last} + 2\pi$, which indicates the angle increases, rotates clockwise, and crosses the $-\pi/\pi$ -junction;

- ψ_{now} is in the fourth quadrant, $\Delta\psi = \psi_{now} - \psi_{last}$, i.e., the angle increases without crossing the junction.

- case 5 to case 8: if ψ_{last} is in the second quadrant
 - ψ_{now} is in the first quadrant, $\Delta\psi = \psi_{now} - \psi_{last}$, i.e., the angle either increases or decreases without crossing the junction;

- ψ_{now} is in the second quadrant, $\Delta\psi = \psi_{now} - \psi_{last}$, i.e., the angle increases without crossing the junction;
- ψ_{now} is in the third quadrant, $\Delta\psi = \psi_{now} - \psi_{last}$, i.e., the angle increases without crossing the junction.
- ψ_{now} is in the fourth quadrant, if ψ_{now} satisfies

$$|\psi_{now}| + \psi_{last} \leq \pi \quad (4.3)$$

$\Delta\psi = \psi_{now} - \psi_{last}$, which indicates the angle decreases without crossing the junction; otherwise, $\Delta\psi = \psi_{now} - \psi_{last} + 2\pi$, which indicates the angle increases, rotates clockwise, and crosses the $-\pi/\pi$ -junction;

- case 9 to case 12: if ψ_{last} is in the third quadrant

- ψ_{now} is in the first quadrant, if ψ_{now} satisfies

$$\psi_{now} + |\psi_{last}| \leq \pi \quad (4.4)$$

$\Delta\psi = \psi_{now} - \psi_{last}$, which indicates the angle decreases without crossing the junction; otherwise, $\Delta\psi = \psi_{last} - \psi_{now} + 2\pi$, which indicates the angle increases, rotates counter-clockwise, and crosses the $-\pi/\pi$ -junction;

- ψ_{now} is in the second quadrant, $\Delta\psi = \psi_{now} - \psi_{last}$, i.e., the angle either increases or decreases without crossing the junction;
- ψ_{now} is in the third quadrant, $\Delta\psi = \psi_{now} - \psi_{last}$, i.e., the angle increases without crossing the junction;
- ψ_{now} is in the fourth quadrant, $\Delta\psi = \psi_{now} - \psi_{last}$, i.e., the angle increases without crossing the junction.

- case 13 to case 16: if ψ_{last} is in the fourth quadrant
 - ψ_{now} is in the first quadrant, $\Delta\psi = \psi_{now} - \psi_{last}$, i.e., the angle either increases or decreases without crossing the junction;
 - ψ_{now} is in the second quadrant, if ψ_{now} satisfies

$$\psi_{now} + |\psi_{last}| \leq \pi \quad (4.5)$$

$\Delta\psi = \psi_{now} - \psi_{last}$, which indicates the angle decreases without crossing the junction; otherwise, $\Delta\psi = \psi_{last} - \psi_{now} + 2\pi$, which indicates the angle increases, rotates clockwise, and crosses the $-\pi/\pi$ -junction;

- ψ_{now} is in the third quadrant, $\Delta\psi = \psi_{now} - \psi_{last}$, i.e., the angle increases without crossing the junction;
- ψ_{now} is in the fourth quadrant, $\Delta\psi = \psi_{now} - \psi_{last}$, i.e., the angle increases without crossing the junction.

When the angle change, $\Delta\psi$, is obtained, the accumulative LOS angle, ψ_{Σ} and the previous LOS angle, ψ_{last} , will be updated by:

$$\psi_{\Sigma} = \psi_{\Sigma} + \Delta\psi \quad (4.6)$$

$$\psi_{last} = \psi_{now} \quad (4.7)$$

The accumulative LOS angle will be used for control purpose.

4.4 Summary

This chapter introduces the computer program that is to simulate ship-ice interaction, ship manoeuvring, and ship autopilot. Particularly, the numerical implementation of

the ship-ice interaction and the mapping method to continue LOS angle are interpreted with detail. The program is capable of conducting prescribed PMM tests, ship manoeuvring tests, and path-following tests. It is developed based on the model described in chapter 2 and chapter 3. The performance of this program will be presented in the next chapter.

Chapter 5

Results, Validation, and Analysis

The numerical simulation method need to be validated prior to applying to any practical use. The validation process or the benchmark process is accomplished by comparing the simulation results to model tests results or full scale sea trials data. Two ships, one is a Canadian Coast Guard icebreaker, CCGS Terry Fox, and the other is a R-Class icebreaker, Sir John Franklin, are selected for validation in this chapter. The benchmark data includes: the model-scale straight progress tests of CCGS Terry Fox (Derradji-Aouat, 2002; Lau, 2006), the model-scale PMM tests of the R-Class icebreaker Sir John Franklin (Newbury, 1992; Shi, 2002), and the full-scale sea trials of the R-Class icebreaker Sir John Franklin (Keinonen, 1996; Keinonen et al., 1991). Prior to the validation, studies on convergence of the program, the effect of different P-A relations, and the effect of flexural ice plate model are conducted. At last, the performance of the guidance and controller is investigated and presented in section 5.7.

5.1 Convergence Study

The time step and the discrete length, which is defined as the distance between two adjacent nodes on the ice edge, are two key factors that will affect the accuracy of the numerical method. The effects are studied in this section. The length ratio of discrete length to ship width, denoted as

$$ratio = l_{DL}/B \quad (5.1)$$

is used to study the effect of discrete length.

This study is accomplished with a 1:21.8 scale Terry Fox model ship at the speed of 0.3m/s and 0.6m/s, and a 300-second period is simulated. The ratio's range is set from 0.001 to 0.1, and the time step has a range from 0.05 to 0.0005. The mean global ice resistance and the computational time cost are selected as the criteria.

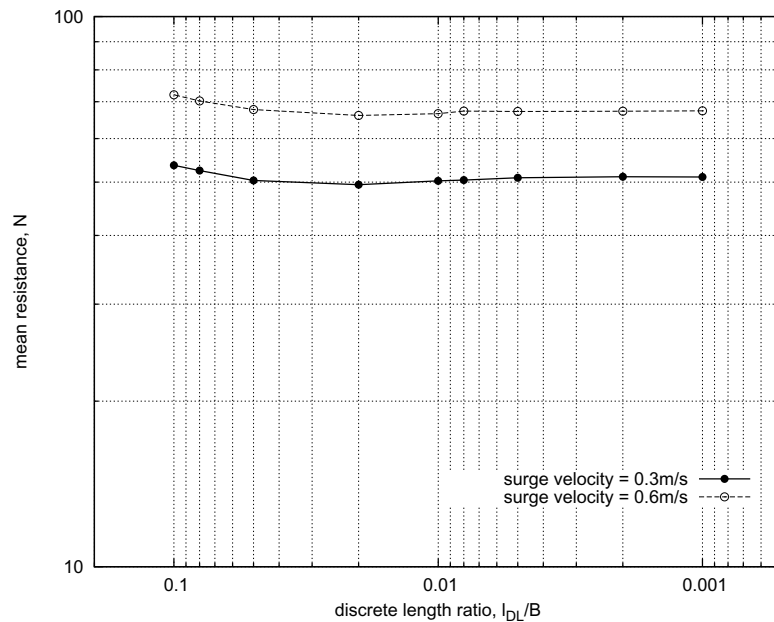


Figure 5.1: Simulated global resistance as a function of discrete length of ice with time step of 0.01s

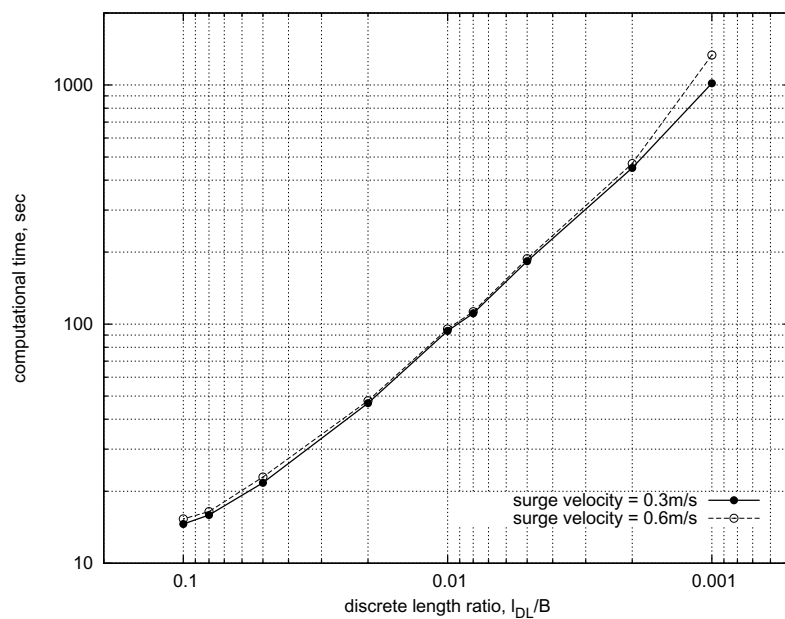


Figure 5.2: Computational time cost as a function of discrete length of ice with time step of 0.01s

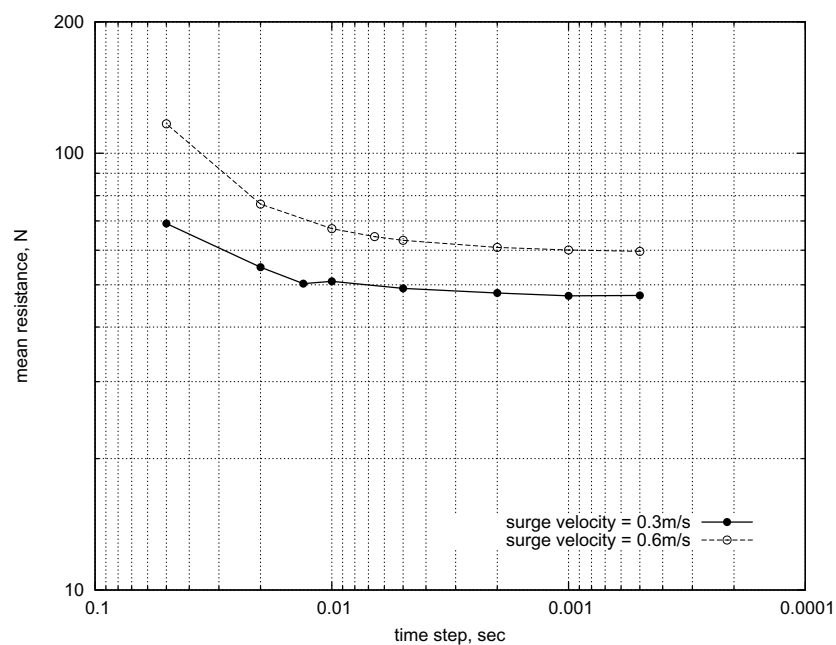


Figure 5.3: Simulated global resistance as a function of non-dimensional time step with discrete length ratio of 0.004

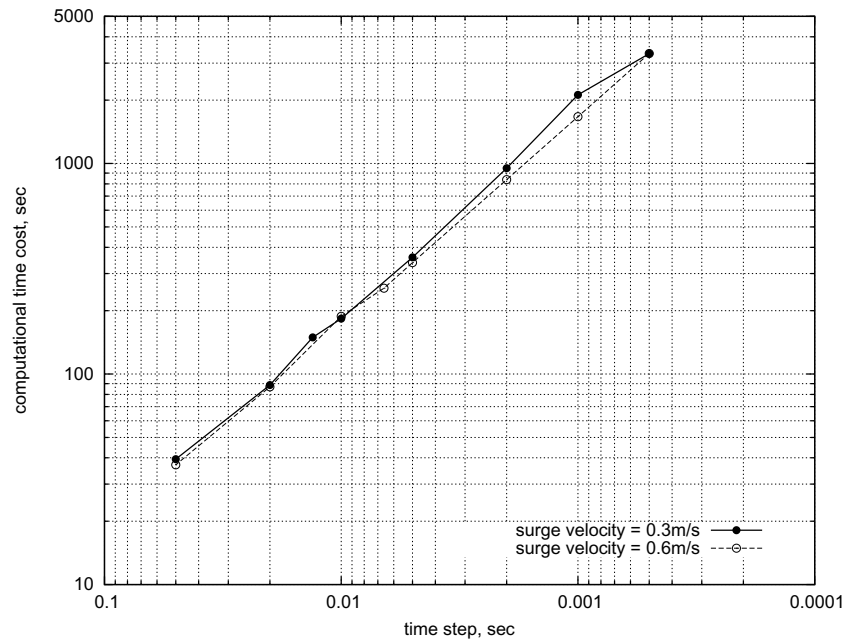


Figure 5.4: Computational time cost as a function of non-dimensional time step with discrete length ratio of 0.004

Figure 5.1 presents the effect of discrete length of the ice edge on the simulated global resistance, Figure 5.2 illustrate the effect of discrete length of the ice edge on the computational time cost. It is easy to observe that the simulated ice resistance is not greatly affect by the length ratio, especially when $ratio \leq 0.01$. This conclusion is valid for the velocities of 0.3m/s and 0.6m/s. However, the computational time cost and the number of the nodes significantly increase as the discrete length decreases. Approximately exponential relationship between time consumption and time step can be observed in Figure 5.2.

Figure 5.3 and Figure 5.4 illustrate the effect of time step on mean ice resistance and real time consumption for simulation. Comparing to Figure 5.1 and Figure 5.2, we conclude that the time step has more significant influence on computational accuracy and time consumption than discrete length does. To balance the computational time cost and the convergence, the length ratio is chosen as 0.004, and the time step is

chosen as 0.002s. The simulated result is then filtered at 5Hz to match the sampling frequency in model tests.

5.2 Study of P-A relation

The P-A relation is expressed by Eq. 2.21. We assume the nominal crushing pressure is constant ($p_0 = \sigma_c = 130KPa$), and the exponent is varying (-0.4, -0.2, -0.1, 0.0, 0.1, 0.2, 0.4). Figure 5.5 sketches the mean ice resistance against velocity with different values of the exponent. The results from Lau (2006) and Derradji-Aouat and Thiel (2004) are also plotted. We can observe that the lines in the figure are approximately parallel which indicate that different exponents will lead to different mean resistance but will not change the relationship between the velocity and the mean resistance. It also can be seen that most tests points fall around line that $ex = 0$. Therefore, the exponent value is chosen as 0.0 in the following study.

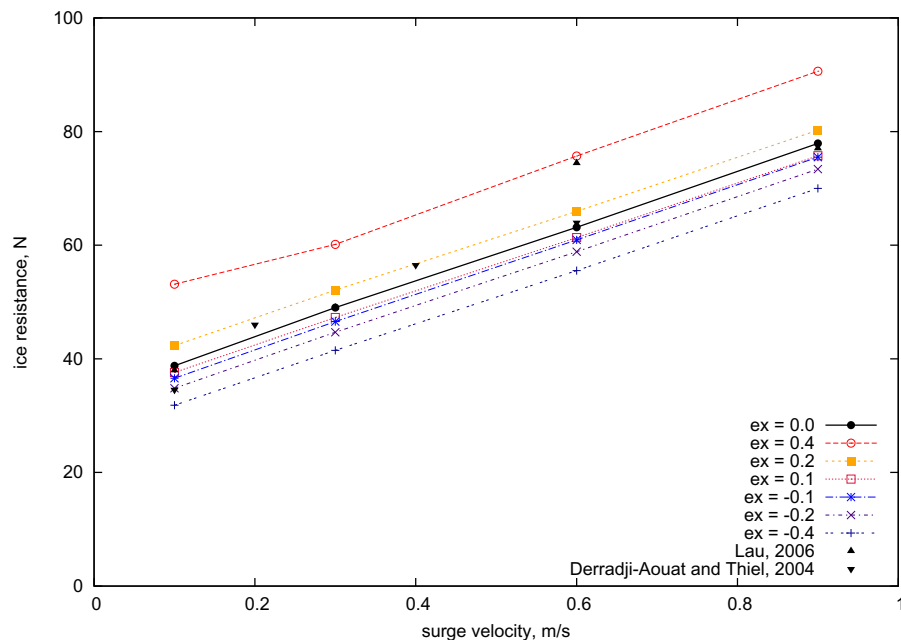


Figure 5.5: Mean ice resistance at different velocity with different exponent values

5.3 Study of the Ice Plate Deflection

According to section 2.4.1.7, the flexural deflection of the ice plate is considered in the research. This section will conduct a study that investigates a single crushing-bending-breaking cycle at stem to determine the effect of the ice flexibility and how significant it is. Valanto (1989) observed rapid flexural failure when the flexural strength ratio E/σ_f was 6400 and longer interaction duration when the ratio was 1400. Similarly to Valanto (1989), we assume the high ratio is 7000 and the low ratio is 2000. The ice models are listed in Table 5.1. The investigation is completed with full scale R-Class icebreaker and four different ice models. The interaction duration and the deflection ratio δ_e/δ_v (see Figure 2.6) are of the interest.

Table 5.1: Different ice model

name	ice model	E/σ_f
rigid 7000	rigid ice plate	7000
rigid 2000	rigid ice plate	2000
flexural 7000	flexural ice plate	7000
flexural 2000	flexural ice plate	2000

Table 5.2: Duration, mean resistance and deflection ratio of different ice model

item	duration, s		mean resistance, MN		deflection ratio
	rigid	flexural	rigid	flexural	δ_e/δ_v
$E/\sigma_f = 2000$	0.125	0.167	-0.460	-0.501	0.25
$E/\sigma_f = 7000$	0.125	0.154	-0.404	-0.428	0.19

Figure 5.6 illustrates the time history of resistance during a single interaction cycle at stem. It can be observed that ice resistance starts to increase when the ship is contacting with the ice. It keeps increasing until vertical component reaches the bearing capability of the ice plate. When breaking happens, the ice load falls. It also can be seen that the lines of “rigid 7000” and “rigid 2000” coincide with each other which means flexural strength ratio does not affect the interaction process when the

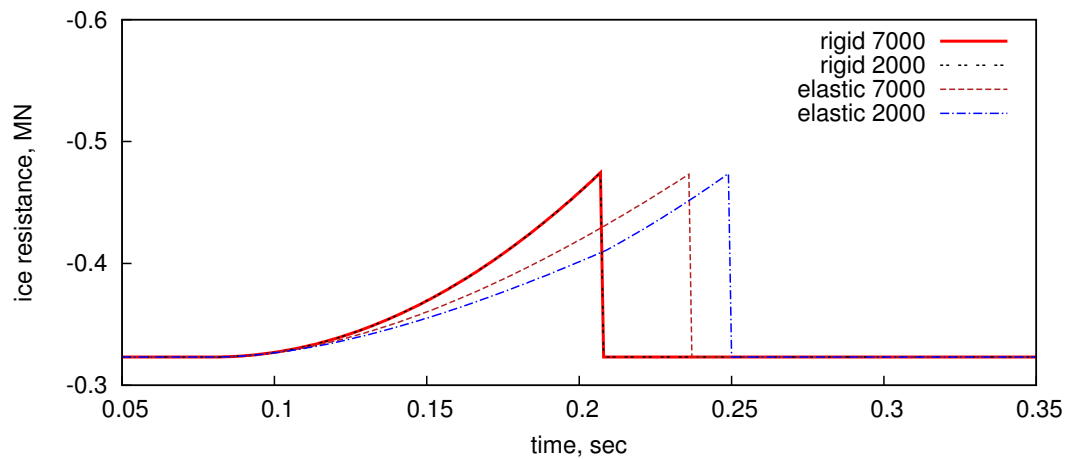


Figure 5.6: Ice resistance with the a single interaction cycle at stem

ice plate is rigid. However, when it is flexural and can be bent downward, the ice load increases slower and the interaction lasts longer. The ice plate with low ratio has longer loading duration than that with high ratio. When the ice load increases slower and lasts longer during a single interaction process, higher mean value can be achieved. Therefore, the ship interacts with flexural ice plate has higher mean ice resistance than that with rigid ice plate. The data is listed in Table 5.2.

Another issue that interests the author is how much the ice plate will be bent if the flexural ice plate model is applied. The deflection starts to occur since the ship contacts with ice plate and keeps increasing until breaking by bending happens. The ratio of maximum elastic deflection to total vertical deflection is listed in Table 5.2. The ratio is 0.25 for low flexural strength ratio ice model and 0.19 for high ratio model. It can be seen that flexure of ice plate is significant to the interaction and the ice resistance. Softer (lower flexural strength ratio) the ice plate is, more significant the effect will be.

5.4 Benchmark with Terry Fox Model Test

5.4.1 Descriptions

According to Derradji-Aouat (2004), Derradji-Aouat and Thiel (2004), Lau (2006), and Liu (2009), the IOT Terry Fox model ship is a 1:21.8 scale model of the Canadian icebreaker, M.V. Terry Fox. The water line profile is illustrated in Figure 5.7, and the main dimensions are listed in Table 5.3.

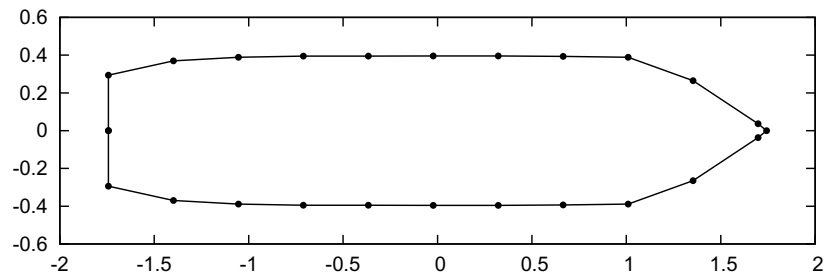


Figure 5.7: IOT Terry Fox model ship water line profile

Table 5.3: Main dimensions of the IOT Terry Fox Model Ship

parameter	notation	unit	value
Length water line	L_{WL}	m	3.74
Draft	T	m	0.368
Beam	B	m	0.0.789
Mass	M	kg	625.8
Block coefficient	C_B	m	0.577
Wet Surface	A_{wet}	m^2	3.984

5.4.2 Straight Motion Test

Resistance tests results of IOT Terry Fox model ship can be seen in Derradji-Aouat and Thiel (2004) and Lau (2006). The ice had flexural strength of 35KPa and thickness of 0.4m. The simulation is conducted with the same ice condition. A 300-second duration is simulated and mean ice resistance is calculated and compared to the

test data and the results from the empirical method proposed by Spencer and Jones (2001). Figure 5.8 presents a sample of time history of ice resistance when the ship is travelling at 0.3m/s. The red line in the figure indicates the mean value. Figure 5.9 illustrates the mean resistance at different velocities.

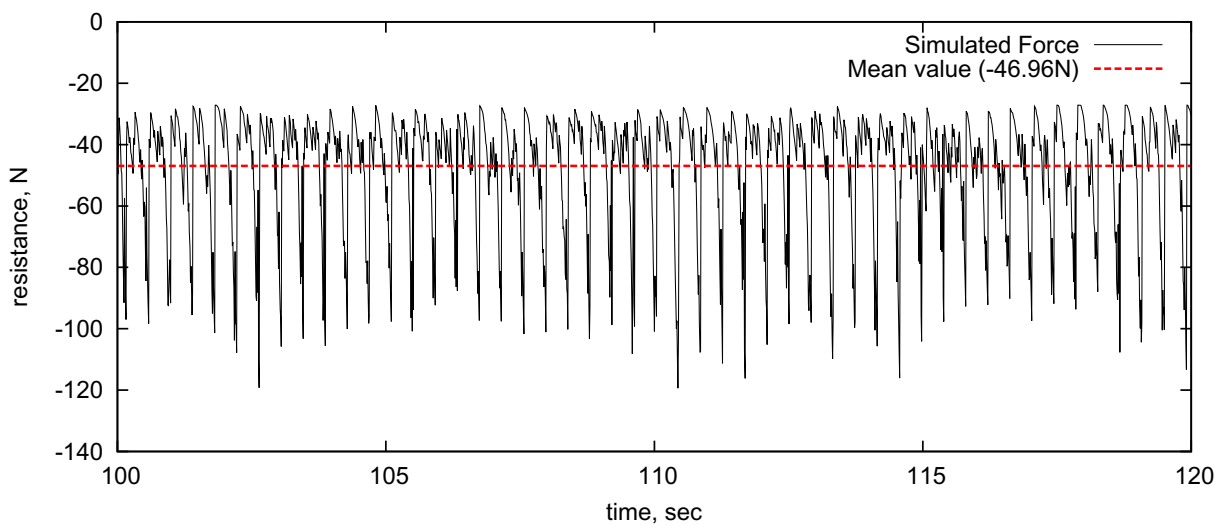


Figure 5.8: Time history of ice resistance when $u=0.3\text{m/s}$

We can see, from Figure 5.8, that ice resistance is fluctuating. The peak value is high which is mainly due to ice breaking, but the mean value is relatively low. It is valid because the the ice breaking force only exists in a very short time. The simulated mean resistance is approximately consistent with the model test results and the empirical calculations as shown in Figure 5.9. A nonlinear relationship between mean resistance and velocity was seen in model tests; however, a linear relationship can be observed in simulation.

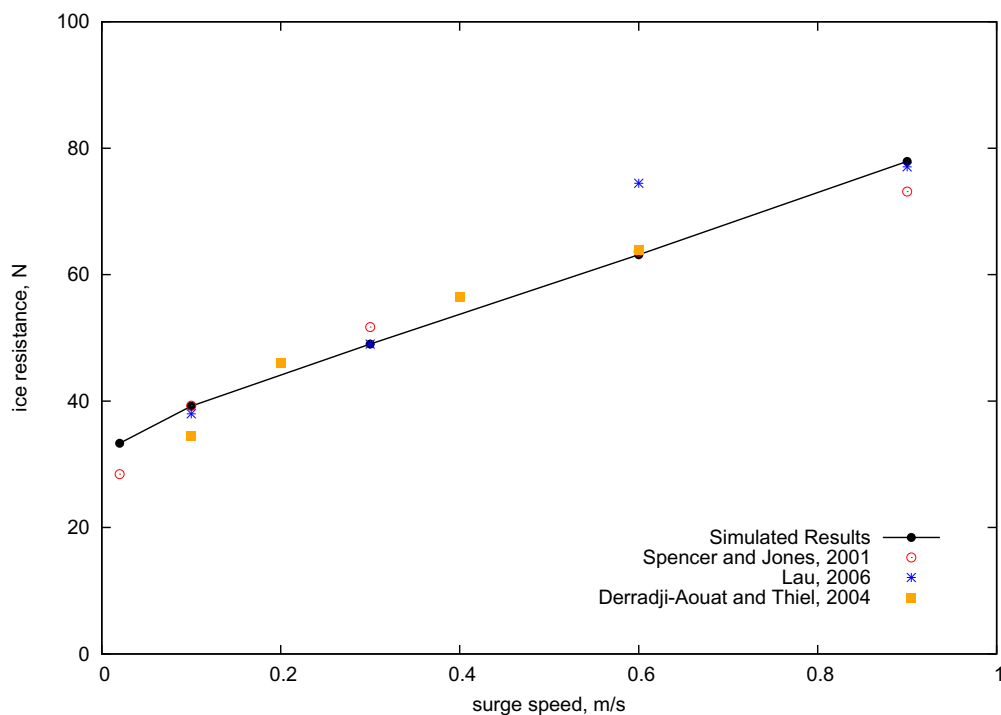


Figure 5.9: Mean ice resistance against ship velocity in straight motion tests

5.5 Benchmark with R-Class Icebreaker Model Test

5.5.1 Descriptions

According to Liu (2009), Newbury (1992), and Shi (2002), the IOT R-Class model ship is a 1:20 scale model of the CCG Sir John Franklin. The water line profile is illustrated in Figure 5.10, and the main dimensions are listed in Table 5.4.

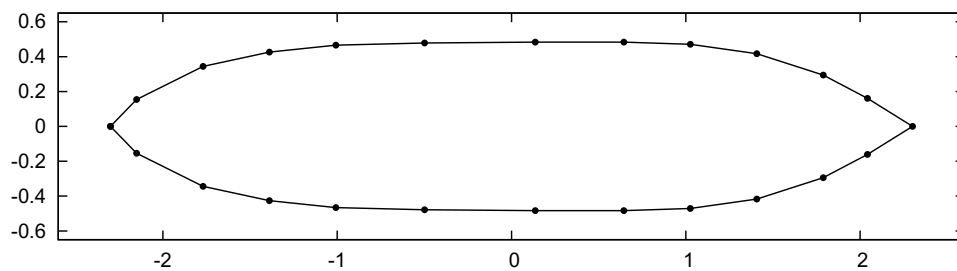


Figure 5.10: IOT R-Class model ship water line profile

Table 5.4: Main dimensions of the IOT R-Class Model Ship

parameter	notation	unit	value
Length water line	L_{WL}	m	4.65
Draft	T	m	0.35
Beam	B	m	0.96
Mass	M	kg	965.00
Block coefficient	C_B	m	0.624
Wet Surface	A_{wet}	m^2	4.627

5.5.2 Pure Yaw Tests

In the pure yaw tests, the ship model is forced to move along a predefined path such that the centreline is always tangent to the path. The predefined path is given by:

$$\bar{x} = \bar{x}_0 \cdot t \quad (5.2)$$

$$\bar{y} = \bar{y}_0 \cdot \sin(\omega \cdot t) \quad (5.3)$$

$$\psi = \psi_0 \cdot \cos(\omega \cdot t) \quad (5.4)$$

where x_0 , y_0 , and ψ_0 are user-defined parameters, and ω is the frequency. The parameters should be chosen to satisfy:

$$v = \cos(\psi) \cdot \dot{\bar{x}} + \sin(\psi) \cdot \dot{\bar{y}} = 0 \quad (5.5)$$

In 1996, Spencer conducted the pure yaw tests with the 1:20 scale R-Class model. During the tests, \bar{x}_0 is set as 0.5 and 0.7, \bar{y}_0 is set as 2.5, ψ_0 is set as 0.436, and ω is set as 0.1257. The tests were conducted continuous and divided into several segments. In each segment, mean value of the measured variables, including surge velocity, yaw rate, resistance, sway force, and yaw moment, are recorded as one test point. In order to compare to the test data, similar data processing method is applied. We simulate a full cycle (50s) and calculate a mean value every 2s. The following pictures compare

the time history of resistance, sway force, and yaw moment between the simulations and the model tests. The linear relationship between yaw rate and yaw moment is also compared.

Figure 5.11 to Figure 5.14 illustrate the comparisons when $\bar{x}_0 = 0.5$, and Figure 5.15 to Figure 5.18 illustrate the comparisons when $\bar{x}_0 = 0.7$. Comparing the time history of the simulated resistance and the measured resistance, we can conclude that the mean values are consistent with each other as shown in Figures 5.11 and 5.15. Good agreement can also be observed in time history of yaw moment in Figures 5.13 and 5.17. However, the simulated result has smaller maximum value of yaw moment than the model test does.

The simulated sway force is not consistent with that in model test especially in Figure 5.16. The reason for the phenomenon is unclear and should be studied in the future. In Figures 5.14 and 5.18, the yaw moment is plotted against the yaw rate. Linear relationship is assumed and the fitting line is also presented. The simulated yaw moment is smaller than the measured yaw moment which is also observed in yaw moment time history. under the assumption of the hull geometrical symmetry, the yaw moment should be zero when yaw rate is zero. This can be found in simulated results. However, a non-zero offset value is observed in the model test.

5.6 Benchmark with R-Class Icebreaker Full Scale Sea Trials

5.6.1 Descriptions

Sea trials data of Canadian Coast Guard (CCGS) R-Class icebreaker is available in many papers (Browne et al., 1989; Keinonen, 1996; Keinonen et al., 1991; Williams

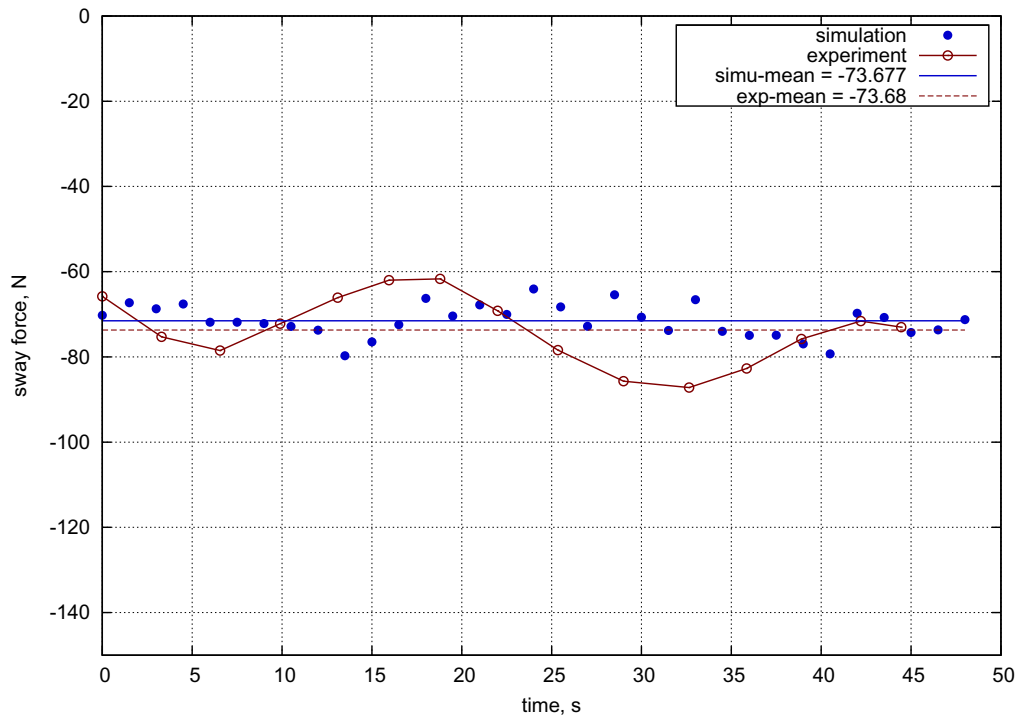


Figure 5.11: Ice resistance during a 50-second continuous pure yaw test, $\dot{x} = 0.5m/s$

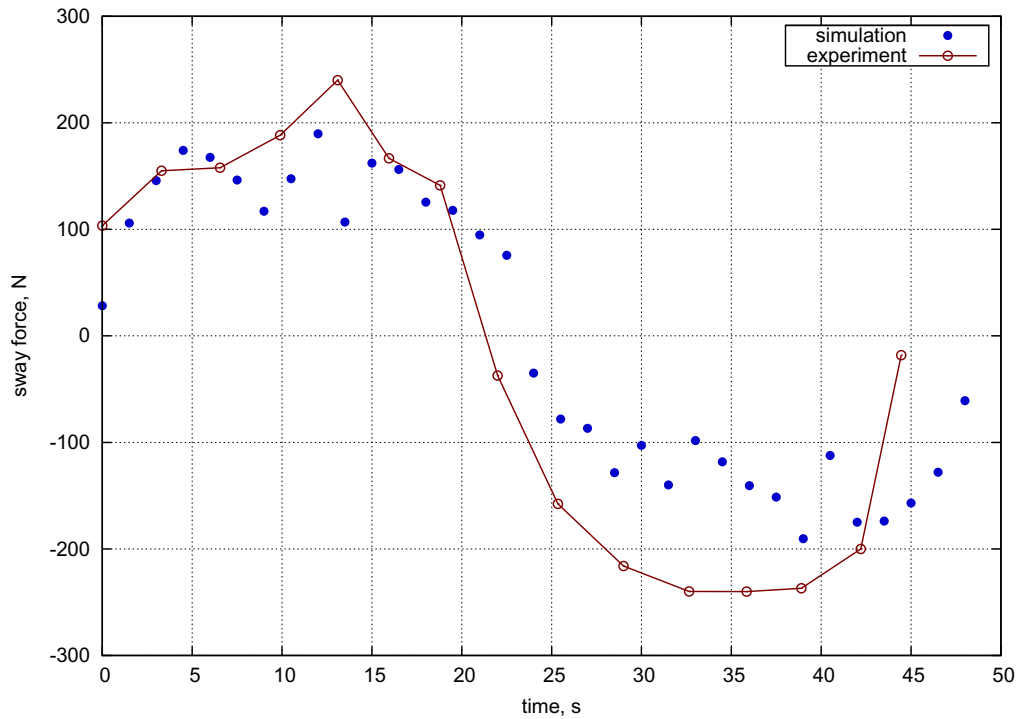


Figure 5.12: Ice induced sway force during a 50-second continuous pure yaw test, $\dot{x} = 0.5m/s$

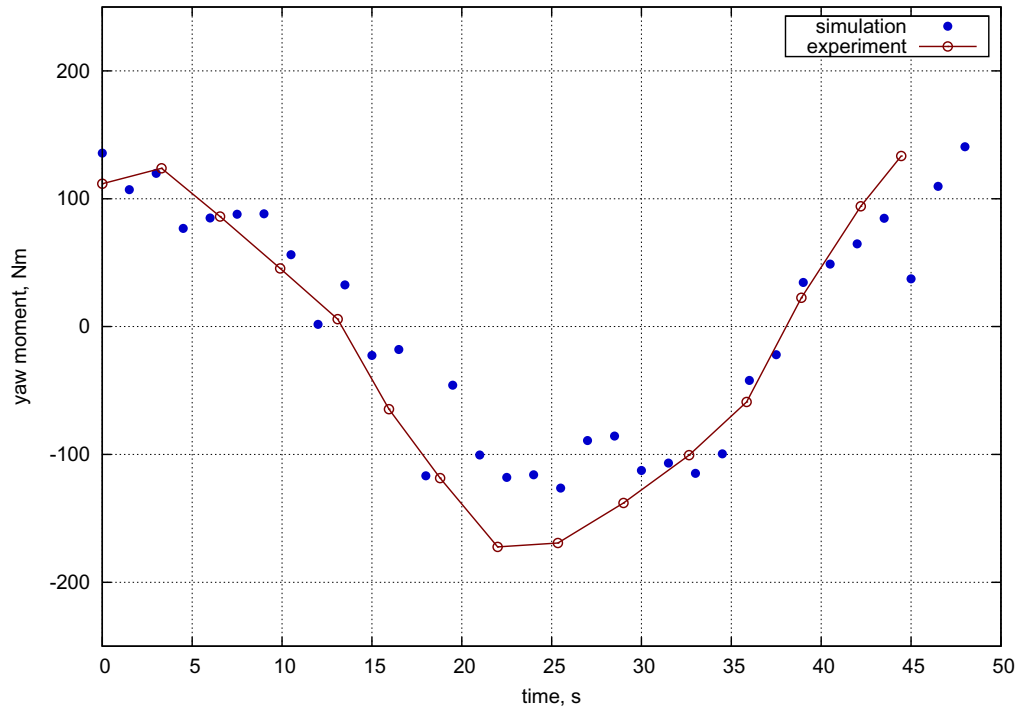


Figure 5.13: Ice induced yaw moment during a 50-second continuous pure yaw test, $\dot{x} = 0.5m/s$

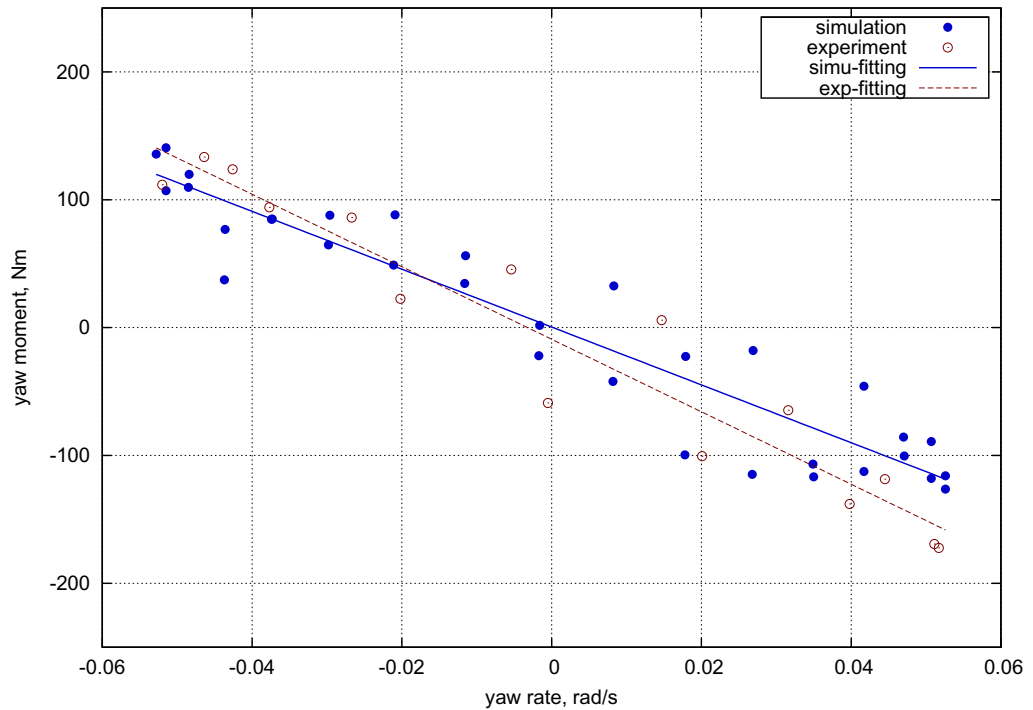


Figure 5.14: Linear regression model between yaw rate and yaw moment, $\dot{x} = 0.5m/s$

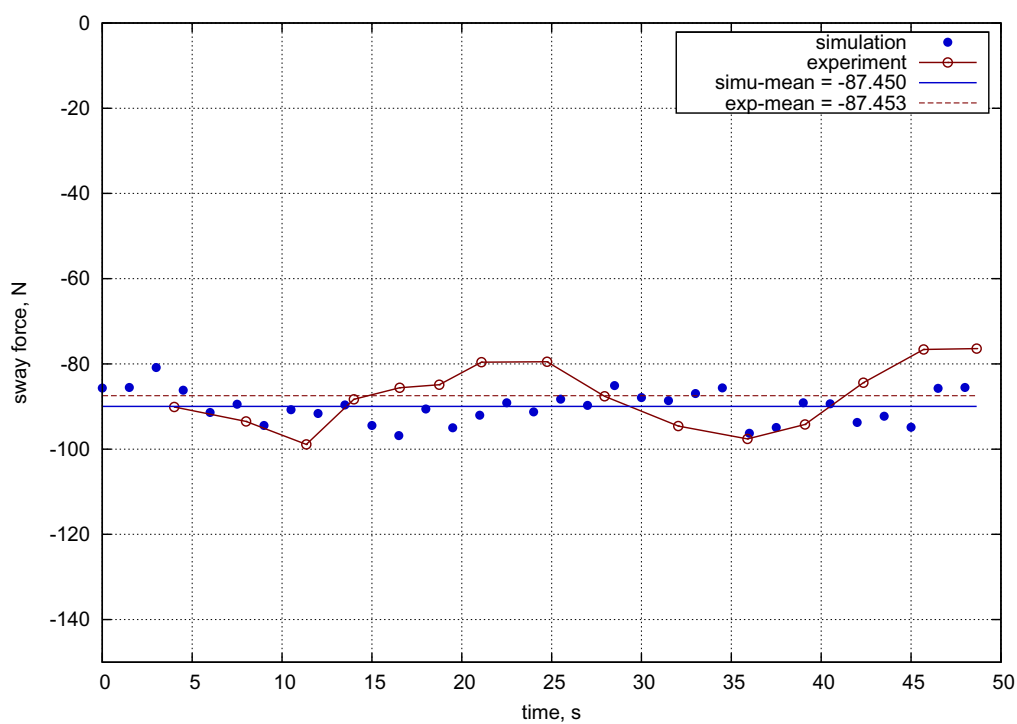


Figure 5.15: Ice resistance during a 50-second continuous pure yaw test, $\dot{x} = 0.7m/s$

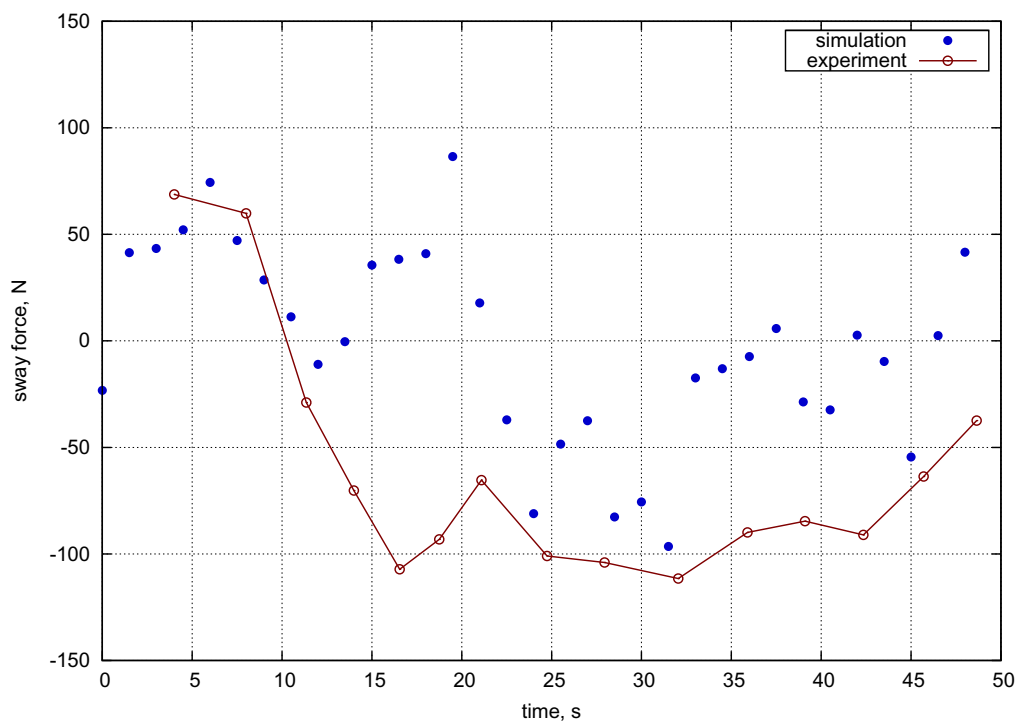


Figure 5.16: Ice induced sway force during a 50-second continuous pure yaw test, $\dot{x} = 0.7m/s$

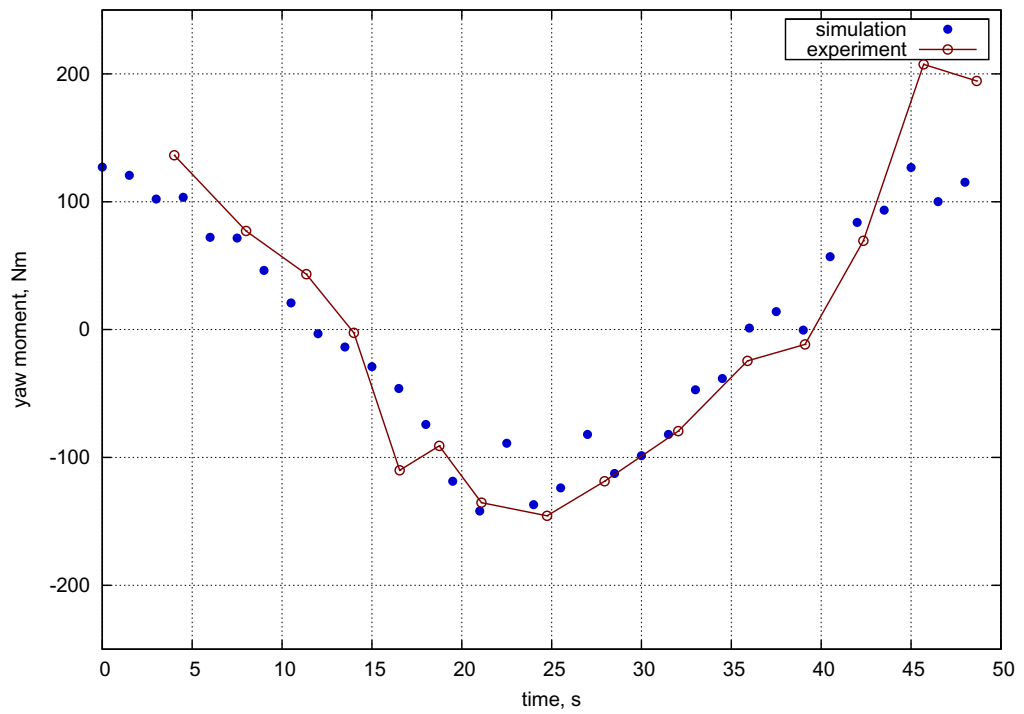


Figure 5.17: Ice induced yaw moment during a 50-second continuous pure yaw test, $\dot{x} = 0.7m/s$

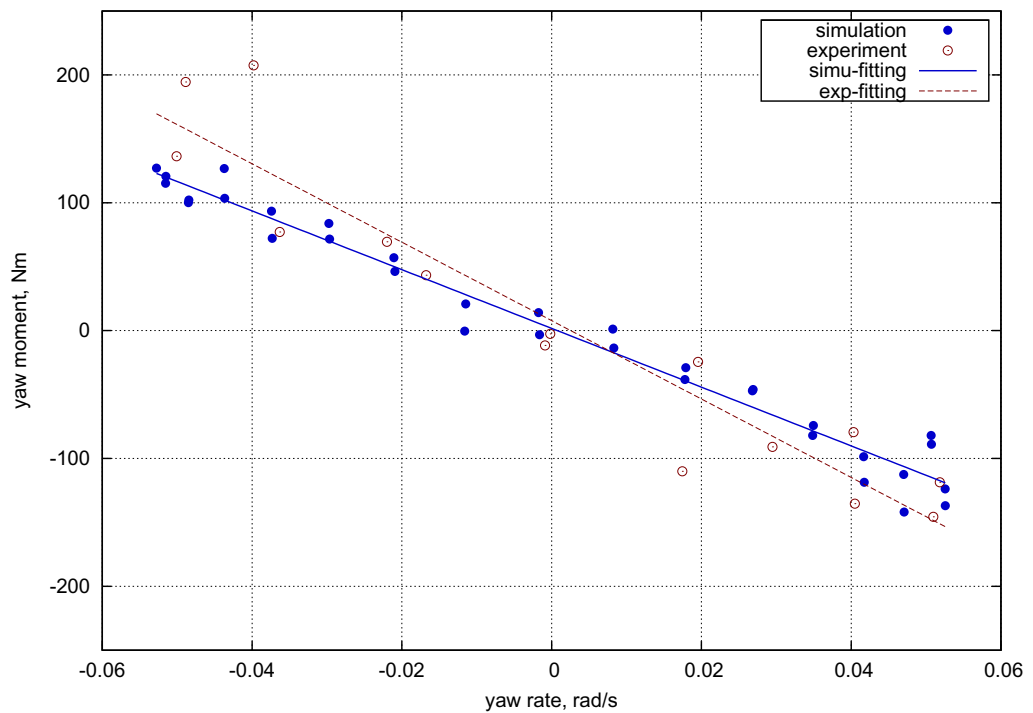


Figure 5.18: Linear regression model between yaw rate and yaw moment, $\dot{x} = 0.7m/s$

et al., 1992). This section presents the comparison between the simulated results and the sea trials data of a full scale CCGS R-Class icebreaker, CCGS Sir John Franklin. Two manoeuvres are included: straight motion and turning a circle. The profile of the water line is similar to what is illustrated in Figure 5.10. The main dimensions are listed in Table 5.5.

Table 5.5: Main dimensions of the full scale CCGS R-Class icebreaker

parameter	notation	unit	value
Length water line	LWL	m	93
Length between perpendiculars	LPP	m	87.96
Draft	T	m	6.94
Beam	B	m	19.37
Block coefficient	CB	m	0.611
Number of propellers	Np	–	2
Propeller diameter	Dp	m	4.12
Pitch/diameter ratio	P/Dp	–	0.775

5.6.2 Straight Motion

This test is to validate the total resistance and propulsive performance of the ship. Full scale free running tests are conducted both in open water and virgin level ice. Simulated propeller thrust and total resistance are compared to sea trial data (Keinonen, 1996). The speed range of the test in open water is from 6.34 m/s to 8.35 m/s, and that of the test in level ice is from 2.3 m/s to 6.3 m/s. Ice thickness varies from 0.489 m to 0.592 m. Simulation is conducted by restricting sway and yaw motion of the ship. Comparison is conducted among simulation, empirical calculation and sea trial data.

Figure 5.19 and Figure 5.20 present the resistance and propeller thrust against ship speed in open water. It can be observed that the simulated water resistance and thrust follow the same trend of sea trial results but are slightly smaller.

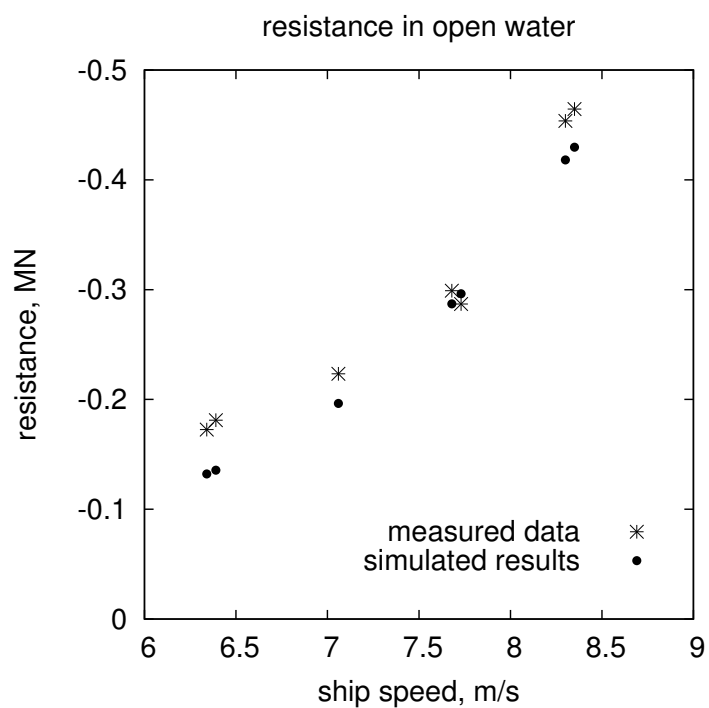


Figure 5.19: Resistance of R-Class in water

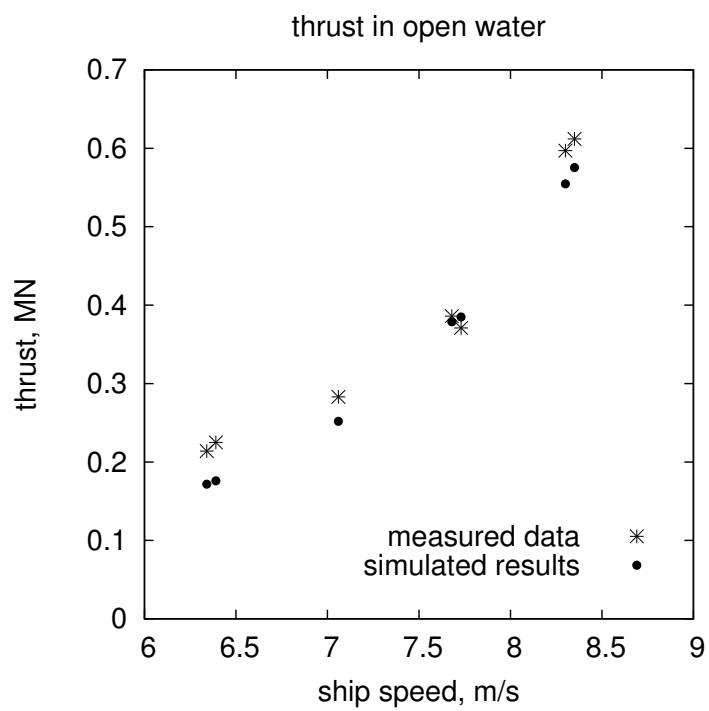


Figure 5.20: Thrust of R-Class in water

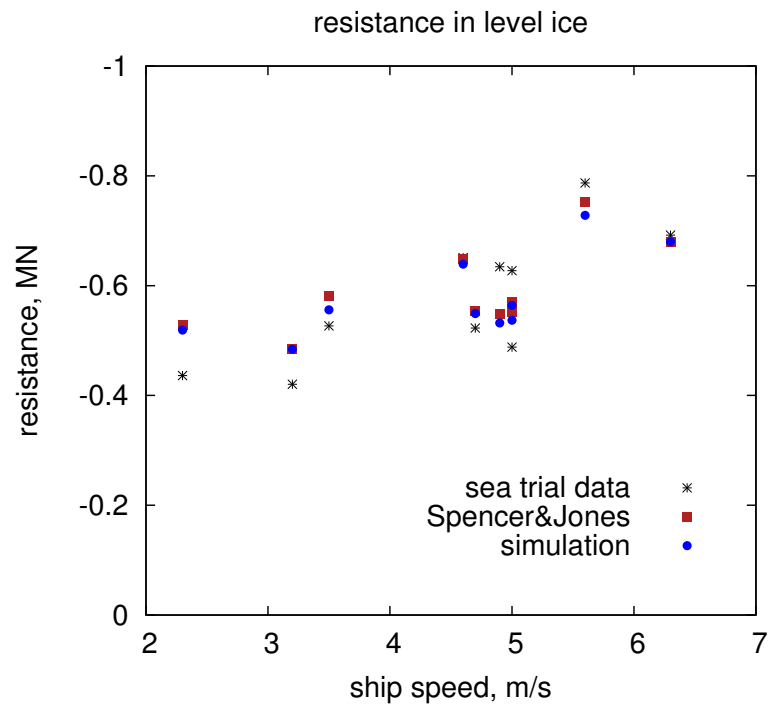


Figure 5.21: Resistance of R-Class in level ice

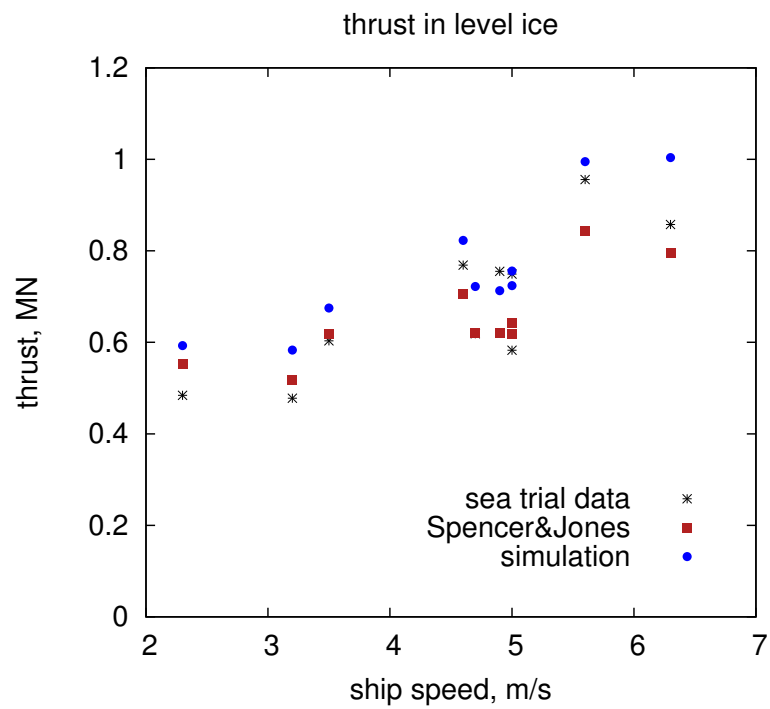


Figure 5.22: Thrust of R-Class in level ice

The total resistance and thrust in ice are presented in Figure 5.21 and Figure 5.22. Comparisons are conducted among three sources: sea trial data, empirical calculation given by Spencer and Jones (2001), and numerical method proposed in this paper. Simulated resistance shows consistence with empirical calculation. However, propeller thrust between simulation and empirical calculation are not consistent with each other. From energy perspective, the phenomenon may result from the impulsive characteristics of ice load that requires more energy. In empirical method ice load is calculated as a constant value; however, in this numerical method, ice load is determined by detecting the contact between ice and ship so that it has a nature of randomization and variation. This may cause more energy loss. Therefore, to maintain the speed, more energy is required which means higher propeller thrust is needed. Good agreement can be observed between sea trials and the other two methods.

5.6.3 Turning a Circle

Turning performance was also investigated during sea trials both in open water and in level ice (Keinonen, 1996). All trials were conducted with starboard rudder. Comparison of steady speed in turn and turning diameter between sea trials and simulations are listed in Table 5.6. Turning circles and ice breaking channel are presented in Figure 5.23. Sample time history of ship velocity and ice load in surge, sway, and yaw directions in ice field are presented in Figure 5.25 and Figure 5.24.

Table 5.6: Turning performance - steady speed in turn and turning diameter

Condition	Shaft Speed RPM	Speed, m/s		Diameter, D/D_{WL}	
		Sea Trial	SIMU	Sea Trial	SIMU
Level Ice	170	5.3	5.14	13.12	12.80
Open Water	120	3.8	3.9	4.21	4.1

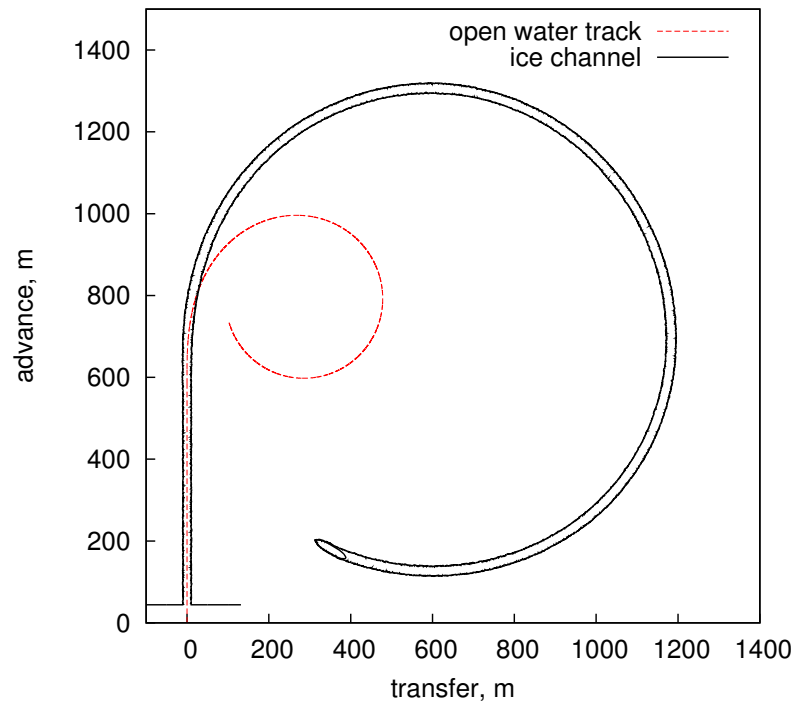


Figure 5.23: Turning track and broken ice channel

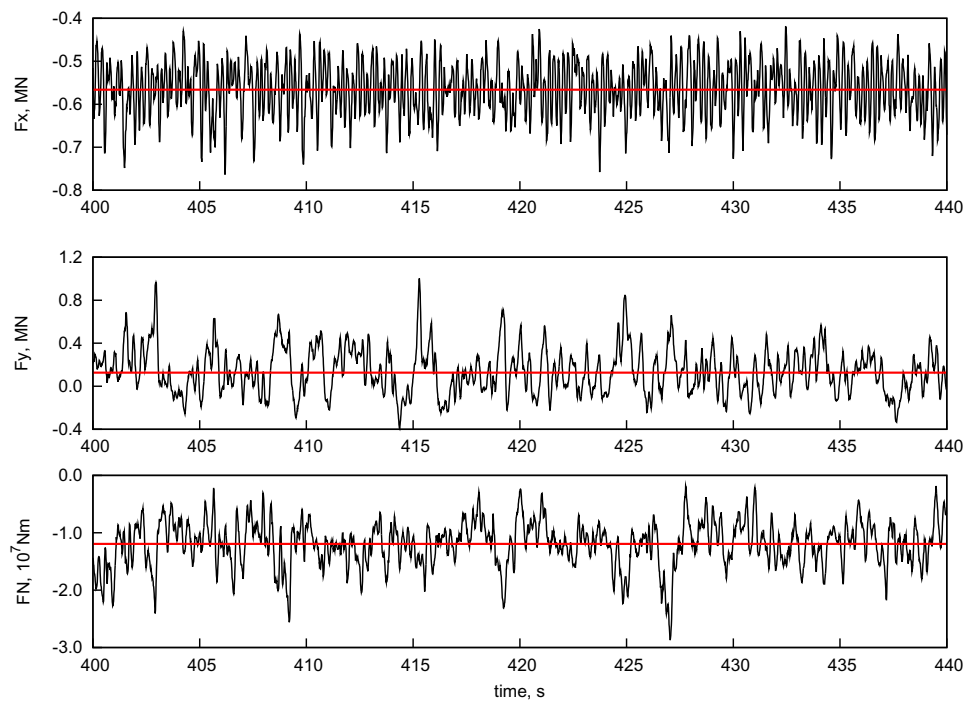


Figure 5.24: Time history of simulated ice load and the mean value during turning

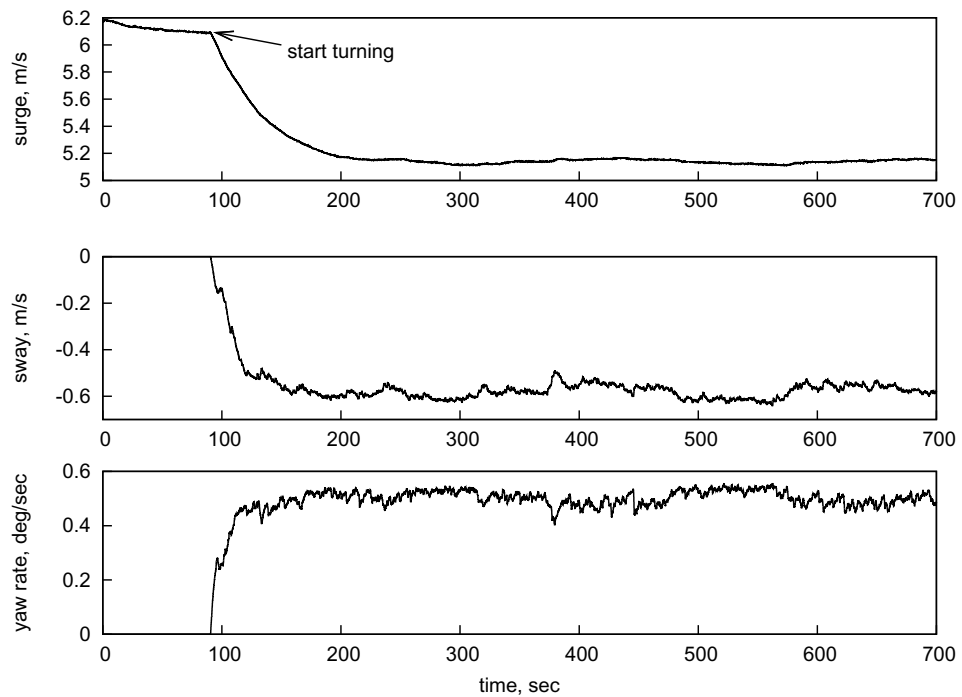


Figure 5.25: Time history of simulated velocities during turning

In the simulation, the ship was kept straight for 600m then turned to full rudder angle (35°). The initial speed is 6.17 m/s (12.0 knots). The shaft speeds are 170 rpm in ice and 120 rpm in water. The steady speeds and turning circle diameters are listed in Table 5. Good agreement between sea trials and simulation ensures that this numerical method is able to reproduce the turning performance of the ship. The turning circles are shown in Figure 5.23 in which the dashed line represents the track of geometric center of the ship in open water and the black line represents the breaking ice channel.

Figure 5.25 presents 3DOF ship speed during full simulation time (700s) and Figure 5.24 presents 3DOF ice load in a time span of 40s during turning in level ice. The ship starts turning at 90.48s and achieves a stable speed (5.14 m/s) at 200s. The steady sway speed is 0.58 m/s to port side and the yaw rate is 0.5 deg/s clockwise.

The mean resistance during steady turning is 0.566 MN which is consistent with the parameter tuning result shown in Figure 11. The mean value of yaw moment is 11.93 MNm. The speed and ice load in sway and yaw direction have non-zero value due to turning. They are oscillating around the mean value due to ice breaking process.

Another character of the turning path attracts the author's interest is the advance that is defined as the longitudinal distance from the point where the ship starts to turn to the point where the x -axis of the ship has turned 90 degrees. The advance is highly related to the path following capability because it is the minimum value when the ship is required to change heading by 90 degrees. In this simulation, the ship starts to turn at (600, 0), the advance is 375m and 700m for turning in water and in ice, respectively.

5.7 Study of Path-Following Ability

Previous sections mainly investigate the manoeuvrability of a ship in ice. In this section, the controllability is examined with the full scale R-Class icebreaker CCGS Sir John Franklin. The ship is simulated under the command of the LOS guidance and control system both in water and in ice. The performances of the ship are provided during a single convergence action and different path-following cases. The control signals are also provided and analyzed in the single convergence action.

5.7.1 Analysis of a Single Convergence Action

Before investigating the performance in a fully path-following process, a single convergence action is analyzed. It is sketch in Figure 3.1, i.e., we assume the ship's current position, as well the reference and target points, and let the ship automatically operate until it converges to the desired path. The goal of conducting such analysis is to

tune the PID controller to avoid steady error and inappropriate overshoot in heading and position. It is also considered as a preliminary examination of the path-following ability.

When the ship is in open and calm water, the current position is assumed as $(0, 0)$; the reference and the target points are located at $(400, 0)$ and $(1000, 1200)$, respectively; and the speed setpoint is 6.17m/s (12.0knots). The PID coefficients are listed in Table 5.7. Figure 5.26 illustrates the simulation result in water, and Figure 5.27 shows the heading signals and the rudder angle in the single convergence action. Figure 5.28 illustrate the surge speed control and the shaft resolution.

Table 5.7: Value of PID coefficients for control in water

Control Object	K_p	K_d	K_i
shaft resolution	0.1	3.0	0.001
rudder angle	2.8	70.0	0
LOS guidance system	0.003	0.55	0

From Figure 5.26, it can be observed that the ship eventually converges to the path and heads towards the target point. Under the command of the LOS guidance and control system, the underactuated ship is able to accomplish the Geometric Task in 3DOF. We observe that the rapid change in heading signal is avoided by introducing a reference model in Figure 5.27. However, a phase lag is generated due to applying a low-pass filter as the reference model. Actual heading increases from initial value and finally converges to the target value. Good performance of surge speed control can also be seen in Figure 5.28.

Table 5.8: Value of PID coefficients for control in ice

Control Object	K_p	K_d	K_i
shaft resolution	0.1	3.0	0.001
rudder angle	2.8	70.0	0
LOS guidance system	0.003	0.55	0

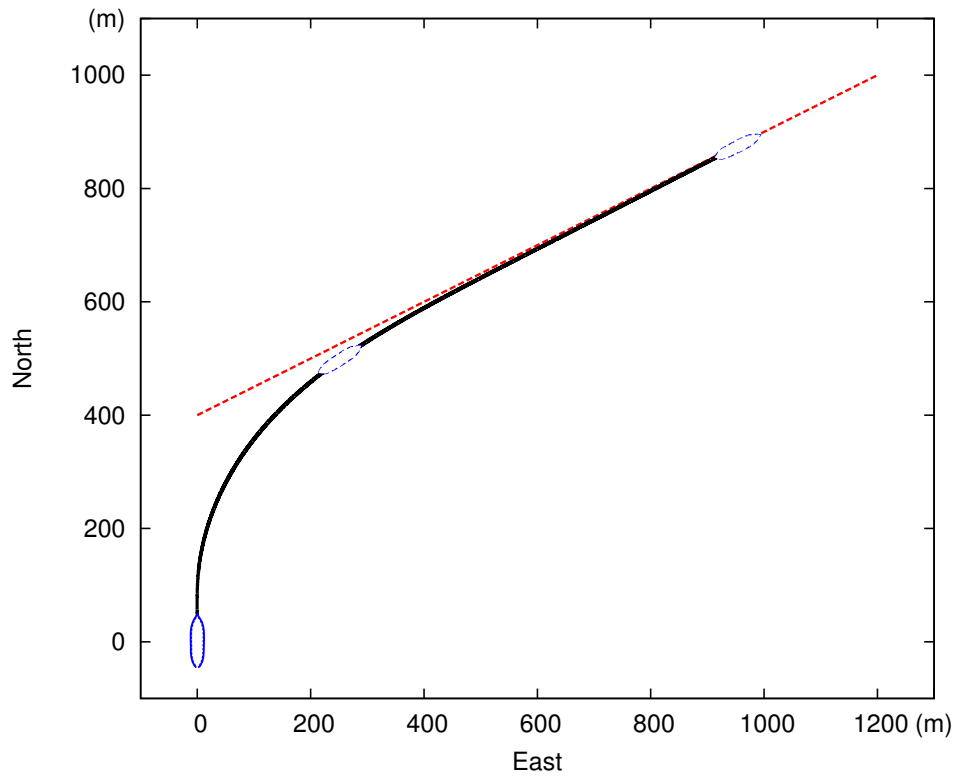


Figure 5.26: Simulated ship track of a specific single convergence action in water

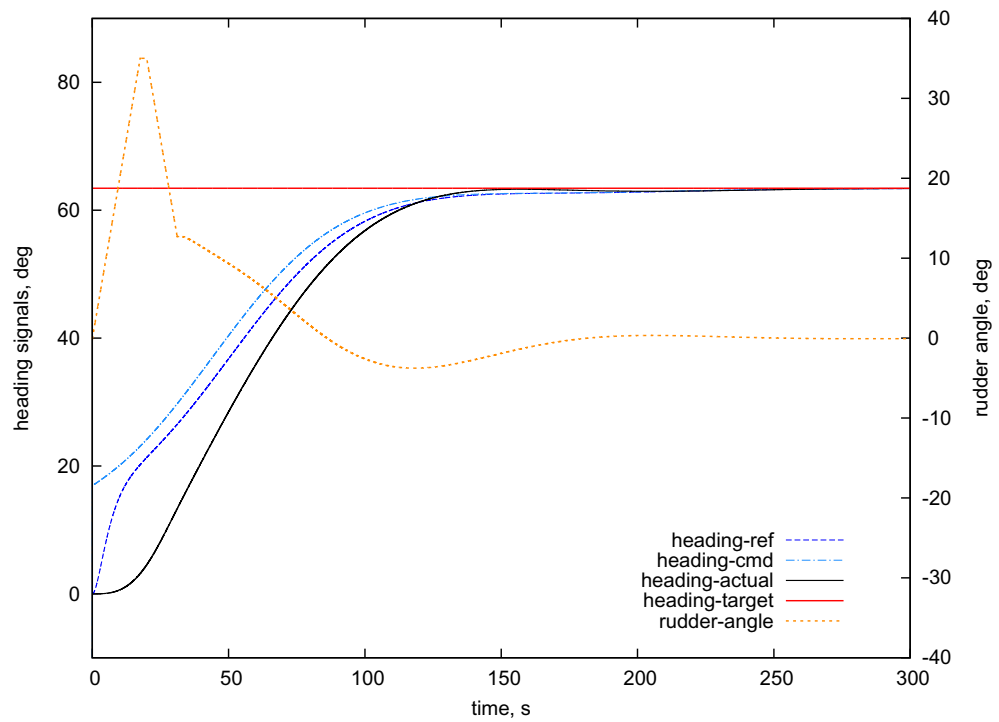


Figure 5.27: Simulated heading signals of a specific single convergence action in water

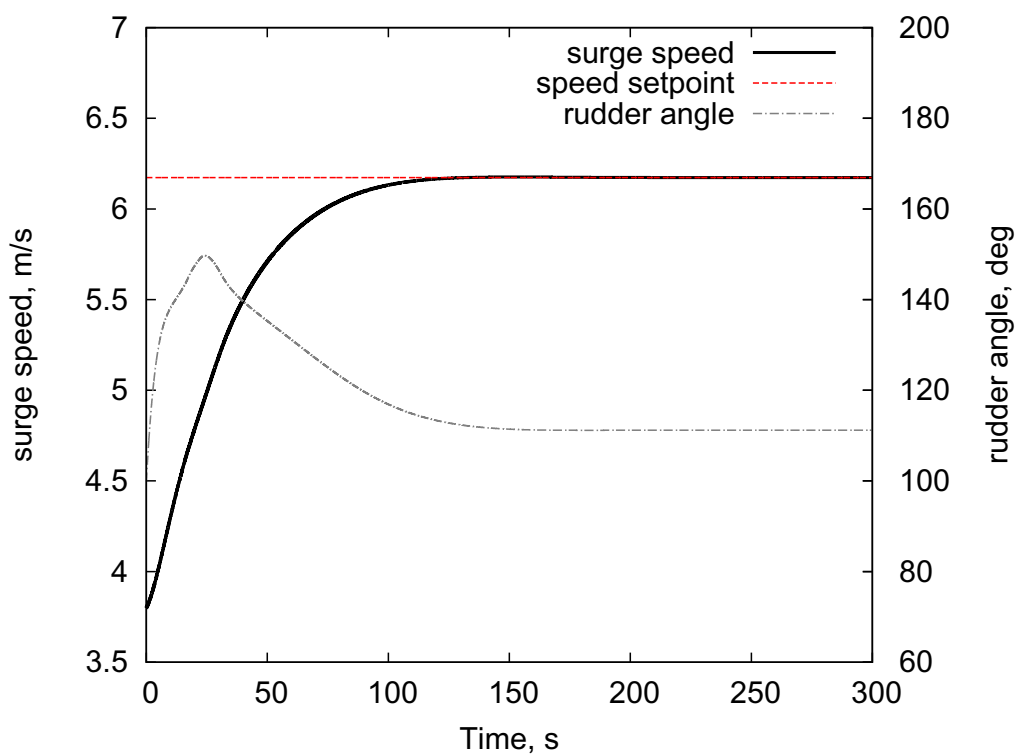


Figure 5.28: Simulated surge speed of a specific single convergence action in water

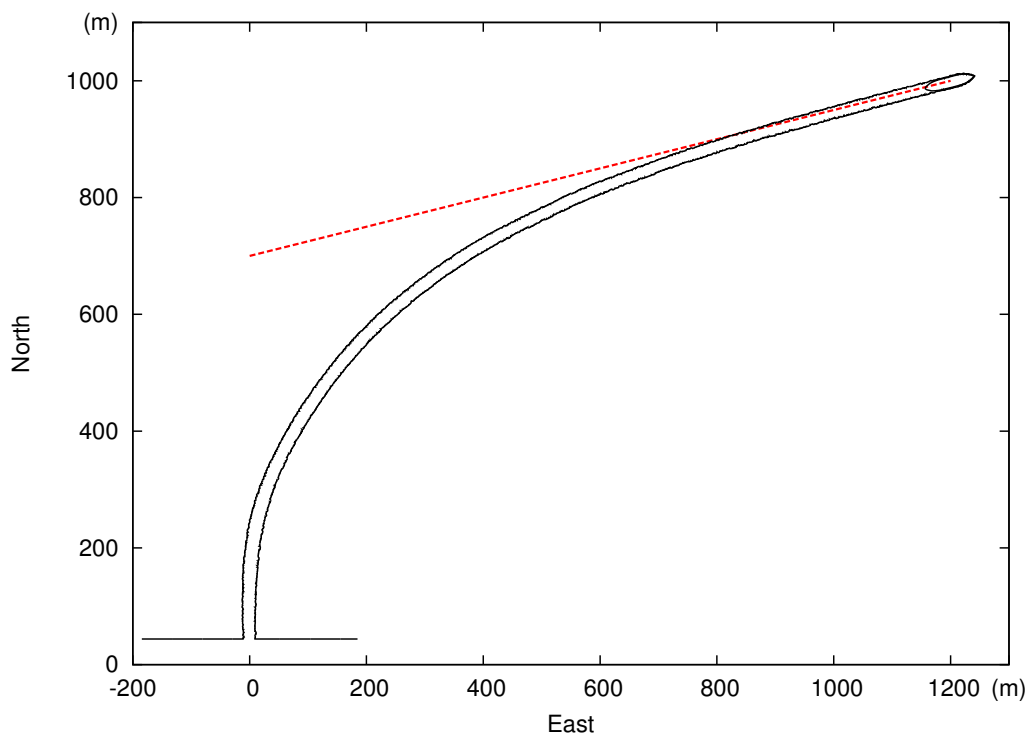


Figure 5.29: Simulated ship track of a specific single convergence action in ice

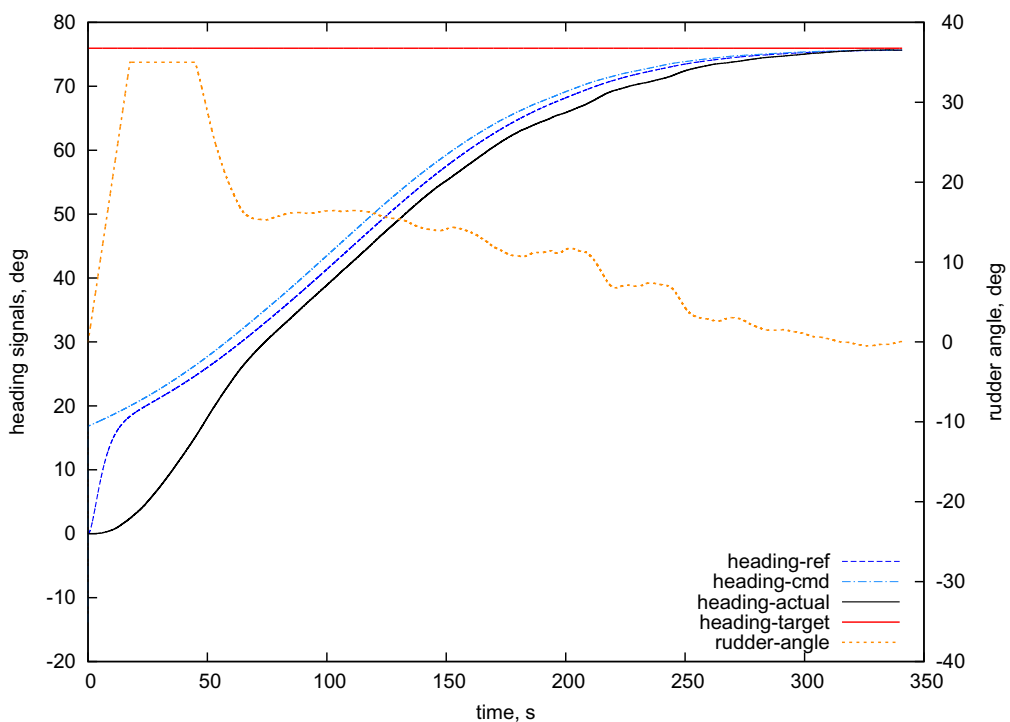


Figure 5.30: Simulated heading signals of a specific single convergence action in ice

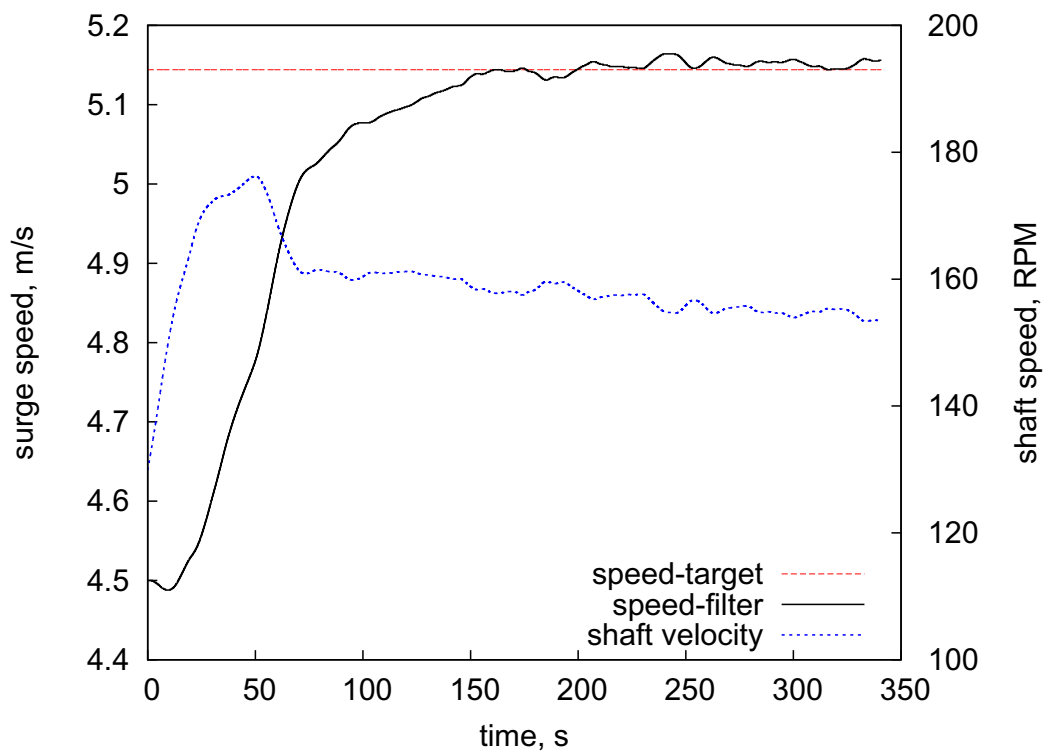


Figure 5.31: Simulated surge speed of a specific single convergence action in ice

Due to operating in open and calm water, the ship lacks oscillating disturbance, such as waves or ice load, so that the control signals are smooth. However, it is no longer true when the ice load is introduced. We assume the ship's current location is at $(0, 0)$, that the reference point is at $(750, 0)$, and that the target point is at $(1000, 1200)$. Different reference points are used in simulations in water and in ice. This is due to different turning abilities of the ship. As mentioned in section 5.6.3, the advance is 375m and 700m for turning in water and in ice. The distance between the reference points and the initial locations are selected slightly larger than the advance. Because if it is selected too small, the controller will never be tuned so that the ship can converge to the path without crossing it. The ship speed is 5.14m/s (10.0knots). Different PID gains are listed in Table 5.8 for control in level ice condition. Figure 5.29 to Figure 5.31 illustrates the simulations in ice.

Similar results can be observed comparing the simulation in water to that in ice. The most significant difference between them is that the commands of the rudder (Figure 5.30) and the propeller (Figure 5.31) in ice are not as smooth as that in water. This phenomenon is due to the ice breaking force which is noisy and randomized.

5.7.2 Path-Following Performance

In the previous section, the single convergence action has been investigated, and the controller has been tuned. The performance in full path-following is then simulated by adopting the PID coefficients provided in the previous. Two desired paths are provided to examine the controllability of the ship both in ice and in water. The paths are given as way-point tables which can be found in Table and Table. The initial position of the ship is $(0, 0)$, and the heading angle is 0 which means the ship is towards north. The target velocity is 6.17m/s (12.0knots) in water and 5.14m/s (10.0knots) in ice. The radius of the circle of acceptance is set as 370m. The simulated tracks of the

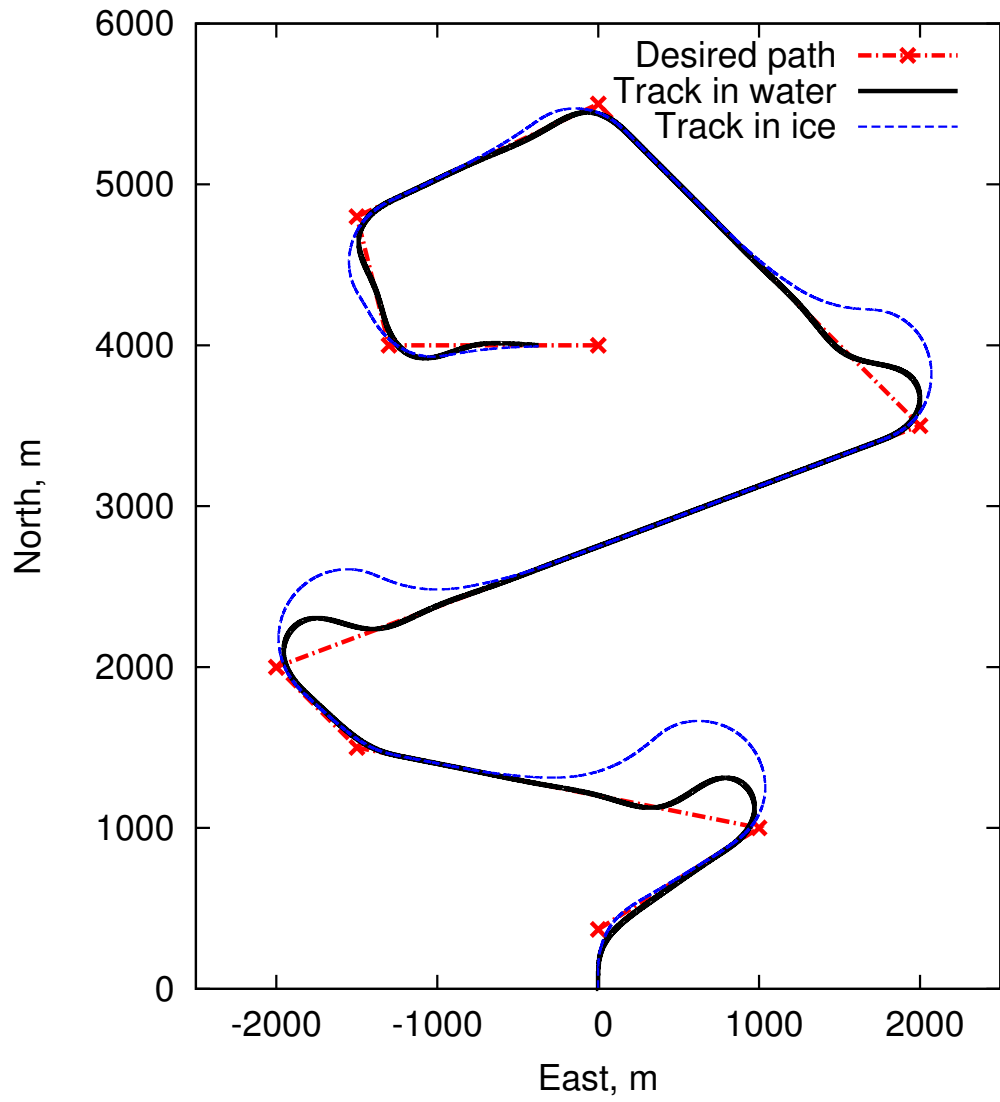


Figure 5.32: Simulated performance of path following capability, case 1

center of the ship are illustrated in Figure 5.32 and Figure 5.33.

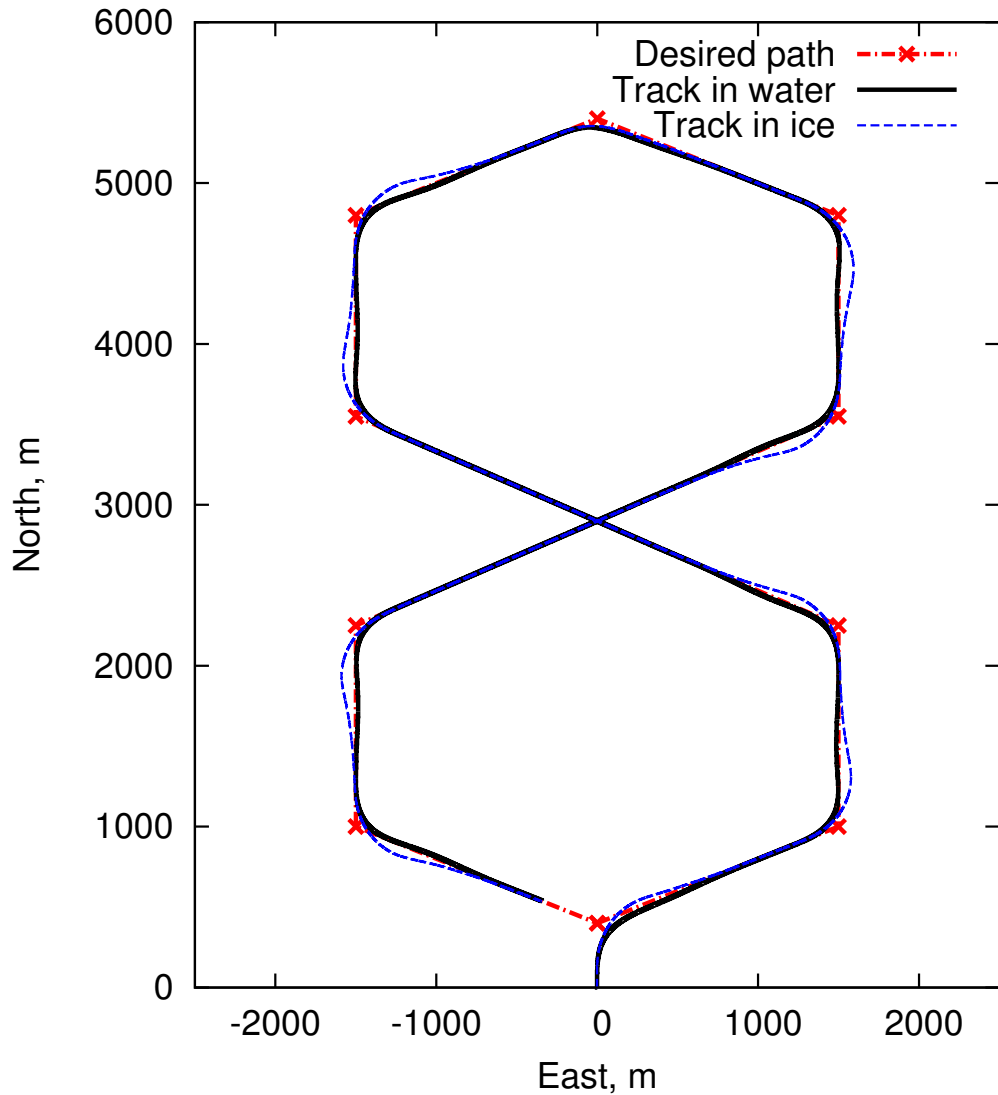


Figure 5.33: Simulated performance of path following capability, case 2

It can be observed in Figure 5.32 that large cross-track error inevitably occurs when the heading angle changes between the adjacent paths exceeds 90 degrees. The phenomena can be seen at way-point 2, 4, and 5 in Figure 5.32. When the path heading angle change is less than 90 degrees, good path following capability can be seen. To verify this conclusion, another path is applied. The path is defined such that every heading angle change is around 45 degrees. The simulation results in Figure 5.33 show

good path following capability of the ship.

The phenomenon that poor path following capability appears when heading angle change larger than 90 degrees results from the turning capability of the ship.

It can also be observed that larger cross-track error exists during heading change in ice than that in water if the same radius of the circle of acceptance is applied. This result from the fact that the turning ability in ice is poorer than it in water.

5.8 Summary

This chapter provides the studies of the convergence of the program, the effect of different P-A relations, and the effect of introducing the flexural ice plate model. Based on the studies, the basic parameters, such as time step, discrete length and the exponent factor in P-A relation, are determined. After that, simulations are carried out with two model ships and one full-scale ship. Prescribed tests are conducted so that the simulation results can be compared to the measured data in the tests. Good agreements can be observed which is able to validate the feasibility of applying the method introduced in section 2 to the study of ship manoeuvring in ice. Finally, the path following ability is investigated with the full-scale R-Class icebreaker. The signals out from the guidance and control systems are studied. The simulated tracks following the pre-defined path indicate the LOS guidance system and the PID controller are capable of automatically operating a ship in water and in level ice conditions.

Chapter 6

Conclusions and Recommendations

6.1 Conclusions

This thesis provided a method that combines numerical detection and semi-empirical formulas to solve the ship-level ice interaction in time domain which can be applied to studying ship manoeuvring in level ice. The LOS guidance system and the PID controller were also introduced, and simulations of path following performance of a ship in ice were carried out.

The main contributions of the thesis include:

- A literature review on analytical solutions and numerical solutions to ship-level ice interactions is provided, especially the numerical solutions published after 2004. All the analytical solutions break the total ice load into its components so that different mechanics of ship-ice interaction can be isolated and studied. This strategy is also applied by the numerical solutions. Those solutions presented different methods to numerically detect ship-ice contact. After that, analytical formulas would be applied to achieve the load due to interaction. Single or multiple ice failure modes can be simulated simultaneously in those numerical

solutions.

- A new ship-ice interaction detecting method named Polygon-Point Algorithm is developed. The method is able to detect the 2D contact by investigating whether a point is inside a polygon or not. An interpolation mechanism is also included in the method so that good balance between calculation accuracy and time consumption can be achieved. The Polygon-Point Algorithm can also be used in other 2D geometrical overlap detecting problems such as the interaction of a ship and small ice floes.
- The Pressure-Area relationship and the flexural ice plate model are included in the numerical method. Parametric studies on their effects of ship-ice interaction and global ice load on ships are conducted.
- A mathematical model that expresses the influence of ice buoyancy and ice clearing resistances on sway and yaw motions during turning actions is derived. It considers the ship's motion status and hull geometry when deriving the sway force and yaw moment from the resistances. Combining with numerically determined 3DOF ice breaking force, this thesis develops a full 3DOF ice load model.
- The validation of this numerical method is carried out with the tests of the Terry Fox ship model, the R-Class icebreaker ship model, and the full scale CCGS R-Class icebreaker. Straight motion test, pure yaw test, and self propulsion test are simulated and compared with measured data. The capability of this numerical method is thoroughly verified and validated with an extensive set of test data.
- The Line-of-Sight guidance system and the PID controller is designed, and the controllability and path following ability is investigated. Due to the fluctuating

nature of the ice breaking force, the actuators should change frequently. However, the simulated heading angle gradually converges to the desired value, and the simulated surge velocity oscillates in a small range which is close to the required speed. These indicate that the LOS guidance system and PID controller is sufficient for ship autonomous operation in level ice conditions.

- A stand-alone software is developed by using FORTRAN 90 language which provides a simulation platform based on the numerical method. It simulates ice load and ship motions. The software is capable of simulating multiple predefined tests such as turning tests, PMM tests, and self propulsion tests. The software is also able to simulate automatic ship operation both in calm water and in level ice.

6.2 Recommendations

The ultimate goal of the whole study is to develop a software that could be an alternative method to model tests to study ship-ice interaction. It is also expected that the software is able to help train operators in ice and to be used to study dynamic positioning in ice. This thesis, which establishes a simplified ship-level ice interaction and studies the possibility of path following in level ice, is the first step towards the ultimate goal. Future effort can be made to the following aspects:

- Empirical models are implemented in the current model to calculate ice bearing capacity and ice breaking length. Meanwhile, it simplifies the problem and make it solvable but less realistic. It would be beneficial if future studies is on establishing a relation between the empirical coefficients and ship motions, hull geometries, and ice characteristics.

- Empirical formulas are used when achieving ice buoyancy and ice clearing forces since the dynamics of a single broken ice piece and its interaction with the ship are not included in the current numerical model. Meanwhile, only two ice failure modes, crushing and breaking, are simulated. Future works on those issues would make the software capable of simulating ship manoeuvring in any ice conditions.
- Current model assumes a semi-infinite ice plate with uniform thickness and ice strength. This can barely be seen in the field, not even in ice tank tests. Statistical variation of ice characteristics, especially ice thickness and strength, should be considered in future work.
- This study only deals with ship manoeuvring in 3DOF. The motions of pitch, heave, and roll are out of the scope. Tan et al. (2013) did the preliminary study of pitch and heave motions during ship-level ice interaction in 6DOF. More effort should be made in order to better understanding of a ship's motion.
- From the guidance perspective, the LOS guidance system should be extended from straight line path following to curve path following. The nature of ice load, such as max value and frequency, should be thoroughly studied so that feedforward control law or optimal control law could apply. Effort should also be devoted to designing multi-controllers that could automatically manage the ship in different environments.

Bibliography

- Bhawsinka, K. (2011). Maneuvering simulation of displacement type ship and planning hull. Master's thesis, Memorial University of Newfoundland, St. John's, Canada.
- Breivik, M. (2003). Nonlinear maneuvering control of underactuated ships. Master's thesis, Norwegian University of Science and Technology, Trondheim, Norway.
- Breivik, M. (2010). *Topics in Guided Motion Control of Marine Vehicles*. PhD thesis, Norwegian University of Science and Technology, Trondheim, Norway.
- Browne, R., Keinonen, A., and Revill, C. (1989). *Icebreaker Design Synthesis Analysis of Contemporary Icebreaker Performance*. Transportation Development Centre, AKAC Inc.
- Colbourne, D. (1989). *Component Method of Analyzing Icebreaking Resistance*. PhD thesis, Memorial University of Newfoundland.
- Daley, C. (1991). Ice edge contact—a brittle failure process model. *Acta Polytechnica Scandinavica, Mechanical Engineering Series No. 100*.
- Daley, C. (1992). Ice edge contact and failure. *Cold Regions Science and Technology*, 21(1):1–23.

- Daley, C. (2004). A study of the process-spatial link in ice pressure-area relationships. Technical Report 7-108, PERD/CHC.
- Daley, C. (2010). Course notes of engi9096/8074 arctic ocean engineering. Technical report, Memorial University of Newfoundland.
- Daley, C., Tuhkuri, J., and Riska, K. (1998). The role of discrete failures in local ice loads. *Cold Regions Science and Technology*, 27(3):197–211.
- Derradji-Aouat, A. (2002). Experimental uncertainty analysis for ice tank ship resistance experiments. Technical Report TR-2002-04, Institute of Marine Dynamics (IMD/NRC).
- Derradji-Aouat, A. (2004). Experimental uncertainty analysis for ship model testing in the ice tank. In *Proceedings of the 25th Symposium on Naval Hydrodynamics*.
- Derradji-Aouat, A. and Thiel, A. V. (2004). Terry fox resistance tests - phase iii (pmm) testing ittc experimental uncertainty analysis initiative. Technical report, Institute for Ocean Technology, National Research Council (IOT/NRC), St. John's, Canada.
- Enkvist, E. (1972). On the ice resistance encountered by ships operating in the continuous mode of icebreaking. Technical Report No. 24, The Swedish Academy of Engineering Science in Finland.
- Enkvist, E. (1983). A survey of experimental indications of the relation between the submersion and breaking components of level ice resistance to ships. In *Proceedings of Seventh International Conference on Port and Ocean Engineering Under Arctic Conditions (POAC'83)*, volume 1, pages 484–493.

- Enkvist, E., Varsta, P., and Riska, K. (1979). The ship-ice interaction. In *Proceedings of the 5th International Conference on Port and Ocean Engineering under Arctic Conditions (POAC)*, volume 2, pages 977–1002.
- Fossen, T. (1994). *Guidance and Control of Ocean Vehicles*. John Wiley & Sons.
- Fossen, T. (2011). *Handbook of marine craft hydrodynamics and motion control*. John Wiley & Sons.
- Fossen, T. I., Breivik, M., and Skjetne, R. (2003). Line-of-sight path following of underactuated marine craft. In *Proceedings of IFAC Conference Manoeuvring and Control Marine Crafts*, pages 244–249.
- Gong, I. (1993). Development of maneuvering simulation program, part i: Mathematical models for maneuvering motions in deep/shallow water with wind/current effects. Technical Report IR-1993-09, Institute of Marine Dynamics.
- Hirano, M. (1981). A practical calculation method of ship maneuvering motion at initial design stage. *Journal of Naval Architecture and Ocean Engineering*, 19:68–80.
- Holtrop, J. and Mennen, G. (1982). An approximate power prediction method. *International Shipbuilding Progress*, 29:166–170.
- ITTC (2002). The specialist committee on esso osaka, final report and recommendations to the 23rd ittc. In *Proceedings of the 23th International Towing Tank Conference*, volume 2.
- Jones, S. (1989). A review of ship performance in level ice. In *Proceedings of the 8th International Conference on Offshore Mechanics and Arctic Engineering (OMAE)*, pages 325–342.

- Jones, S. (2004). Ships in ice - a review. In *Proceedings of the 25th Symposium on Naval Hydrodynamics*, pages 1–18.
- Kashteljan, V., II, P., and Ryvlin, A. (1969). Resistance of ice to the motion of ships. Technical report.
- Keinonen, A. (1996). Icebreaker characteristics synthesis. Technical Report TP 12812E, Arno Keinonen Arctic Consulting Inc.
- Keinonen, A., Browne, R., and Revill, C. (1989). *Icebreaker Design Synthesis Analysis of Contemporary Icebreaker Performance*. Arno Keinonen Arctic Consulting Inc.
- Keinonen, A., Browne, R., and Revill, C. (1991). Icebreaker design synthesis: Phase 2: Analysis of contemporary icebreaker performance. Technical report, Transportation Development Centre, Arno Keinonen Arctic Consulting Inc.
- Kerr, A. D. (1976). The bearing capacity of floating ice plates subjected to static or quasi-static loads. *Journal of glaciology*, 17:229–268.
- Lau, M. (2006). Preliminary modeling of ship manoeuvring in ice using a pmm. Technical Report TR-2006-02, Institute for Ocean Technology.
- Lau, M., Liu, J. C., Derradji-Aouat, A., and Williams, F. M. (2004). Preliminary results of ship maneuvering in ice experiments using a planar motion mechanism. In *Proceedings of the 17th International IAHR Symposium on Ice*, pages 479–487.
- Lewis, E. V., editor (1988). *Principles of Naval Architecture: Motions in Waves and Controllability*. Society of Naval Architects and Ocean Engineers.
- Lewis, J. and Edwards, R. (1970). Methods for predicting icebreaking and ice resistance characteristics of icebreakers. *Transactions-The Society of Naval Architects and Marine Engineers*, 78:213–249.

- Lindqvist, G. (1989). A straightforward method for calculation of ice resistance of ships. In *Proceedings of the 10th International Conference on Port and Ocean Engineering under Arctic Conditions (POAC'89)*, pages 722–735.
- Liu, J. (2009). *Mathematical Modeling Ice-Hull Interaction for Real Time Simulations of Ship Manoeuvring in Level Ice*. PhD thesis, Memorial University of Newfoundland, St. John's, Canada.
- Martio, J. (2007). Numerical simulation of vessels manoeuvring performance in uniform ice. Technical Report No. M-301, Ship Laboratory, Helsinki University of Technology, Finland.
- Milano, V. (1972). *Ship resistance to continuous motion in ice*. PhD thesis, University Microfilms, Ann Arbor, Michigan, USA.
- Moreira, L., Fossen, T. I., and Soares, C. G. (2007). Path following control system for a tanker ship model. *Journal of Ocean Engineering*, 34(14-15):2074–2085.
- Newbury, S. (1992). Repeatability of resistance experiments in ice with a 1:20 scale model of the canadian r-class icebreaker. In *Proceedings of American Towing Tank Conference (ATTC)*, pages 327–333.
- Nguyen, D. (2011). *Ice Edge Contact-A Brittle Failure Process Model*. PhD thesis, National University of Singapore, Singapore.
- Nguyen, D., Sorbo, A., and Sorensen, A. (2009). Modelling and control for dynamic positioned vessels in level ice. In *Proceedings of the 8th Conference of Manoeuvring and Control of Marine Craft (MCMC'2009)*, pages 229–236.
- Perez, T. and Blanke, M. (2002). Mathematical ship modeling for control applications. Technical Report EE02036, Technical University of Denmark.

- Sawamura, J., Riska, K., and Moan, T. (2009a). Numerical simulation of breaking patterns in level ice at ship's bow. In *Proceedings of 19th International Offshore and Polar Engineering Conference*, pages 600–607.
- Sawamura, J., Riska, K., and Moan, T. (2009b). Numerical simulation of breaking patterns in level ice at ship's bow. In *Proceedings of 20th IAHR International Symposium on Ice*, pages 600–607.
- Shi, Y. (2002). Model test data analysis of ship manoeuvring in ice. Master's thesis, Memorial University of Newfoundland, St. John's, Canada.
- Skjetne, R., Jorgensen, U., and Teel, A. R. (2011). Line-of-sight path-following along regularly parametrized curves solved as a generic maneuvering problem. In *Proceedings of the 50 IEEE Conference on Decision and Control and European Control Conference (CDC-ECC)*, pages 2467–2474.
- SNAME (1950). Nomenclature for treating the motion of a submerged body through a fluid. Technical Report Bulletin 1-5, Society of Naval Architects and Marine Engineers, New York, USA.
- Spencer, D. (1992). A standard method for the conduct and analysis of ice resistance model tests. Technical Report IR-1992-12, Institute for Ocean Technology (IOT).
- Spencer, D. and Jones, S. (2001). Model-scale/full-scale correlation in open water and ice for canadian coast guard "r-class" icebreakers. *Journal of ship research*, 45(4):249–261.
- Su, B., Riska, K., and Moan, T. (2010). A numerical method for the prediction of ship performance in level ice. *Cold Regions Science and Technology*, 60(3):177–188.

- Tan, X., Su, B., Riska, K., and Moan, T. (2013). A six degrees of freedom numerical model for level ice-ship interaction. *Cold Regions Science and Technology (Submitted)*.
- Toxopeus, S. (2011). *Practical Application of Viscous-Flow Calculations for the Simulation of Manoeuvring Ships*. the Maritime Research Institute Netherlands (MARIN).
- Valanto, P. (1989). Experimental study of the icebreaking cycle in 2-d. In *Proceedings of the 8th International Conference of Offshore Mechanics and Arctic Engineering (OMAE'89)*, volume 4, pages 343–349.
- Wang, S. (2001). A dynamic model for breaking pattern of level ice by conical structures. *ACTA POLYTECHNICA SCANDINAVICA MECHANICAL ENGINEERING ME*, 156.
- Williams, F., Spencer, D., Mathews, S., and Bayly, I. (1992). Full scale trials in level ice with canadian r-class icebreaker. *Transactions-The Society of Naval Architects and Marine Engineers*, 100:293–313.
- Zhou, Q. and Peng, H. (2013a). A numerical simulation for operating a dynamic positioned vessel in level ice. In *Proceedings of the 23rd International Offshore and Polar Engineering Conference*, pages 1300–1307.
- Zhou, Q. and Peng, H. (2013b). Numerical simulation for operating a dynamic positioned vessel in level ice. *International Journal of Offshore and Polar Engineering (Submitted)*.

Appendices

Appendix A

Ship resistance estimated by Holtrop and Mennen

The total resistance of a vessel is determined by:

$$R_{total} = R_F(1 + k_1) + R_{app} + R_w + R_B + R_{TR} + R_A \quad (\text{A.1})$$

where:

R_F frictional resistance

$1 + k_1$ form factor

R_{app} resistance of appendages

R_w wave-making and wave-breaking resistance

R_B additional pressure resistance of bulbous bow near the water surface

R_{TR} additional pressure resistance of immersed transom stern

R_A model-ship correlation resistance

The form factor is estimated by prismatic coefficient, C_P , the water line length, L , the longitudinal position of the centre of buoyancy forward of $0.5L$ as a percentage of

L .

$$1 + k_1 = c_{13} \left[0.93 + c_{12} (B/L_R)^{0.92497} (0.95 - C_P)^{-0.521448} (1 - C_P + 0.0225lcb)^{0.6906} \right] \quad (\text{A.2})$$

where:

$$\begin{aligned} L_R/L &= 1 - C_P + 0.06C_P lcb / (4C_P - 1) \\ C_{12} &= \begin{cases} (T/L)^{0.2228446} & \text{if } T/L > 0.05 \\ 48.20(T/L - 0.02)^{2.078} + 0.479948 & \text{if } 0.02 < T/L < 0.05 \\ 0.479948 & \text{if } T/L < 0.02 \end{cases} \\ c_{13} &= 1 + 0.003C_{stern} \end{aligned}$$

In above formulas, T is the average moulded draught. C_{stern} is given by the following table:

Table A.1: Stern Shape Factor

Afterbody form	C_{stem}
V-shaped sections	-10
Normal section shape	0
U-shaped sections with Hogner stern	+10

A.1 Frictional Resistance

The frictional resistance is estimated from:

$$R_F = \frac{1}{2} \rho S U^2 C_F \quad (\text{A.3})$$

where:

S wetted surface area of a ship

C_F frictional coefficient, follow ITTC 1957 Line

$$S = L(2T + B)\sqrt{C_M}(0.453 + 0.4425C_B - 0.2862C_M - 0.003467B/T + 0.3696C_w) + 2.38A_{BT}/C_B$$

$$C_F = 0.075/(\log_{10} R_n - 2)^2$$

where:

A_{BT} transverse sectional area of a bulbous bow at the position where the water surface intersects the stem

R_n Reynolds number ($= UL/\nu$)

C_B block coefficient

C_M midship section area coefficient

ρ density of water

ν kinematic viscosity of water

U ship resultant velocity

A.2 Appendage Resistance

$$R_{app} = \frac{1}{2}\rho S_{app}U^2(1 + k_2)_{eq}C_F \quad (A.4)$$

where:

S_{app} total wetted surface area of appendages ($= \sum S_i$)

$(1 + k_2)_{eq}$ equivalent appendage form factor ($= \sum(1 + k_2)_i S_i/S_{app}$)

$(1 + k_2)_i$ form factor of individual appendage in the following table

S_i wetted surface of individual appendage

Table A.2: Approximate Values of Form Factor for Various Appendages

Appendages	$(1 + k_2)_i$
Rudder behind Skeg	1.5 - 2.0
Rudder behind Stern	1.3 - 1.5
Twin-Screw Balance Rudder	2.8
Shaft Brackets	3.0
Skeg	1.5 - 2.0
Strut Bossings	3.0
Hull Bossings	2.0
Shafts	2.0 - 4.0
Stabilizing Fins	2.8
Dome	2.7
Bilge Keels	1.4

A.3 Wave Resistance

$$R_w = \begin{cases} C_1 C_2 C_5 \nabla \rho g \exp [m_1 F_n^{-0.9} + m_4 \cos(\lambda F_n^{-2})] & \text{if } F_n \leq 0.4 \\ C_{17} C_2 C_5 \nabla \rho g \exp [m_3 F_n^{-0.9} + m_4 \cos(\lambda F_n^{-2})] & \text{if } F_n \geq 0.55 \\ (R_w)_{F_n=0.4} + (10F_n - 4) [(R_w)_{F_n=0.55} - (R_w)_{F_n=0.4}] / 1.5 & \text{if } 0.4 < F_n < 0.55 \end{cases} \quad (\text{A.5})$$

where

$$\begin{aligned} C_1 &= 2223105 C_7^{3.78613} (T/B)^{1.07961} (90 - i_E)^{-1.37565} \\ C_2 &= \exp \left[-1.89 \sqrt{C_3} \right] \\ C_3 &= 0.56 A_{BT}^{1.5} / \left[BT(0.31 \sqrt{ABT} + T_F - h_B) \right] \\ C_5 &= 1 - 0.8 A_T / (BTC_M) \\ C_7 &= \begin{cases} 0.229577 (B/L)^{1/3} & (B/L \leq 0.11) \\ B/L & (0.11 < B/L < 0.25) \\ 0.5 - 0.0625 L/B & (B/L \geq 0.25) \end{cases} \end{aligned}$$

$$\begin{aligned}
C_{15} &= \begin{cases} -1.69385 & (L^3/\nabla \leq 512) \\ -1.69385 + (L/\nabla^{1/3} - 8)/2.36 & (512 < L^3/\nabla < 1726.91) \\ 0 & (L^3/\nabla \geq 1726.91) \end{cases} \\
C_{16} &= \begin{cases} 8.07981C_P - 13.8673C_P^2 + 6.984388C_P^3 & (C_P < 0.8) \\ 1.73014 - 0.7067C_P & (C_P > 0.8) \end{cases} \\
C_{17} &= 6919.3C_M^{-1.3346}(\nabla/L^3)^{2.00977}(L/B - 2)^{1.40692} \\
m_1 &= 0.0140407L/T - 1.75254\nabla^{1/3}/L - 4.79323B/L - C_{16} \\
m_3 &= -7.2035(B/L)^{0.326869}(T/B)^{0.605375} \\
m_4 &= 0.4C_{15} \exp -0.034F_n^{-3.29} \\
\lambda &= \begin{cases} 1.446C_P - 0.03L/B & (L/B \leq 12) \\ 1.446C_P - 0.36 & (L/B > 12) \end{cases} \\
i_E &= 1 + 89 \exp \left[-(L/B)^{0.80856}(1 - C_w)^{0.30484}(1 - C_P - 0.0225lcb)^{0.6367} \right. \\
&\quad \left. (L_R/B)^{0.34574}(100\nabla/L^3)^{0.16302} \right] \quad (\text{A.6})
\end{aligned}$$

where

T_F draft at FP

$(h_B$ vertical position of the center of A_{BT} above the keel ($h_B \leq 0.6T_F$)

A_T immersed part of the transverse area of the transom stern at rest

i_E half angle of entrance

A.4 Pressure Resistance due to Bulbous Bow

$$R_B = 0.11\rho g \frac{\exp(-3P_B^{-2}) F_{ni}^3 A_{BT}^{1.5}}{1 + F_{ni}^2} \quad (\text{A.7})$$

where

P_B measure for the emergence of the bow

$$= 0.56\sqrt{A_{BT}}/(T_F - 1.5h_B)$$

F_{ni} Froude Number based on bow immersion

$$= U/\sqrt{g(T_F - h_B - 0.25\sqrt{A_{BT}}) + 0.15U^2}$$

A.5 Pressure Resistance due to Transom Immersion

$$R_{TR} = \frac{1}{2}\rho U^2 A_T C_6 \quad (\text{A.8})$$

where

$$C_6 = \begin{cases} 0.2(1 - 0.2F_{nT}) & (F_{nT} < 5) \\ 0 & (F_{nT} \geq 5) \end{cases}$$

$$F_{nT} = U/\sqrt{2gA_T/(B + BC_w)}$$

A.6 Model-Ship Correlation Resistance

$$R_A = \frac{1}{2}\rho U^2 S C_A \quad (\text{A.9})$$

where

$$C_A = 0.006(L + 100)^{-0.16} - 0.00205 + 0.003\sqrt{L/7.5}C_B^4 C_2(0.04 - C_4)$$

$$C_4 = \begin{cases} T_F/L & (T_F/L \leq 0.04) \\ 0.04 & (T_F/L > 0.04) \end{cases}$$

